

Fracture of thin-ply composites: effects of ply thickness

THÈSE N° 8032 (2017)

PRÉSENTÉE LE 17 NOVEMBRE 2017

À LA FACULTÉ DES SCIENCES ET TECHNIQUES DE L'INGÉNIEUR
LABORATOIRE DE MÉCANIQUE APPLIQUÉE ET D'ANALYSE DE FIABILITÉ
PROGRAMME DOCTORAL EN MÉCANIQUE

ÉCOLE POLYTECHNIQUE FÉDÉRALE DE LAUSANNE

POUR L'OBTENTION DU GRADE DE DOCTEUR ÈS SCIENCES

PAR

Guillaume FROSSARD

acceptée sur proposition du jury:

Dr M. Farhat, président du jury
Prof. J. Botsis, Prof. T. Gmür, directeurs de thèse
Dr C. Lopes, rapporteur
Prof. J. Costa, rapporteur
Prof. V. Michaud, rapporteuse



ÉCOLE POLYTECHNIQUE
FÉDÉRALE DE LAUSANNE

Suisse
2017

Abstract

The demand for carbon/epoxy laminated composites is continuously increasing due to their high specific modulus and strength. Among them, laminates made of particularly thin layers (from $t=0.015$ to 0.150 mm) and called thin-ply composites are gaining in interest for the larger design space they offer. Moreover, they have outstanding strength properties, thanks to a significant ply thickness effect reflected by a delayed onset of damage. However, the improvement in strength is accompanied by higher brittleness and reduction of fracture toughness. Therefore, this thesis focuses on explanation, characterization, and modeling of ply thickness effects on the inter-, intra-, and trans-laminar fracture of M40JB/TP80EP composites in the range $t=0.150$ to 0.030 mm.

In mode I inter- and intra-laminar fracture, while the critical energy release rate (ERR) at initiation is found practically independent of ply thickness, it is decreased by 50% (interlaminar) and 23% (intralaminar) at steady-state with decreasing ply thickness. During crack growth, fiber bridging develops in the wake of the crack. The heterogeneous microstructure of the thick-ply laminates promotes distributed micro-cracking around the crack surface, crack surface waviness and the development of large bundles of bridging fibers, leading to higher fracture resistance. In contrast, the homogeneous microstructure in thin-ply composites reduces significantly the creation of bridging bundles leading to lower ERR. The results suggest that bridging fibers are better anchored in intra- than inter-laminar fracture due to fiber waviness and misalignment and thus exert larger closing forces that explain the much higher steady-state ERR measured in intra- than in inter-laminar fracture.

The translaminar fracture toughness of cross-ply (CP) and quasi-isotropic (QI) laminates is significantly decreased between $t=0.150$ and 0.030 mm plies at both the initiation (-70%) and steady-state propagation (-77%). The translaminar fracture toughness scales linearly with ply thickness and is found ~25% lower in the QI specimens compared to the corresponding CP specimens. Quantitative morphological studies of fracture surfaces show that the ply thickness effect is directly correlated to

the height of the pull-out fiber bundles, which are much shorter in thinner-ply specimens.

The inter-, intra- and trans-laminar fracture are simulated by cohesive elements models, with linear stiffness degradations corresponding to the initiation ERRs and identified non-linear relations representing the ERRs associated with the toughening mechanisms. In inter- and intra-laminar fracture, these traction-separation relations related to fiber bridging are identified with an efficient R-curve based method developed in this work. In translaminar fracture, the pull-out mechanism is proposed to be modeled by a constant traction level. For each fracture mode, scaling strategies are suggested to account for the ply thickness effects.

Potential solutions to increase the fracture toughness are investigated. Experimental results demonstrate that the fiber hybridization and interlayer toughening strategies improve the trans- and inter-laminar fracture toughness, respectively, but are accompanied by a decrease in the strength properties. In contrast, the change of fiber/matrix combination (T800/Aero2) offers a simultaneous increase in the toughness and strength properties.

Keywords: Carbon fiber reinforced polymers, Thin-ply composite, Interlaminar fracture (delamination), Intralaminar fracture, Translaminar fracture, Fiber bridging, Fiber pull-out, FE modeling, Cohesive elements.

Résumé

La demande pour des composites laminés carbone/epoxy augmente continuellement en raison de leur hauts module et contrainte à la rupture spécifiques. Parmi eux, des laminés à plis très fins (de $t=0.015$ à 0.150 mm) appelés *thin-ply* gagnent de l'intérêt pour leur plus grand espace de conception. De plus, ils ont une contrainte à la rupture exceptionnelle grâce à un effet significatif d'épaisseur de pli reflété par un début d'endommagement retardé. Cependant, l'amélioration de la contrainte à la rupture est accompagnée par une plus grande fragilité et une ténacité réduite. Ainsi, cette thèse caractérise, explique et modélise l'effet d'épaisseur de pli sur les ruptures inter-, intra, et trans-laminaire de composites M40JB/TP80EP dans la plage $t=0.150$ à 0.030 mm.

En ruptures inter- et intra-laminaire en mode I, le taux de restitution d'énergie (ERR) à l'initiation est pratiquement indépendant de l'épaisseur de pli. En réduisant l'épaisseur de pli, il est en revanche réduit de 50% (en interlaminaire) et 23% (en intralaminaire) lors du régime de propagation permanent. Durant la propagation de la fissure, du pontage de fibre se développe dans le sillage de la fissure. La microstructure hétérogène des laminés à plis épais favorise les microfissures distribuées autour de la fissure, l'ondulation de la surface de fissure et le développement de grands faisceaux de fibres pontantes, ce qui conduit à une résistance à la rupture plus haute. Au contraire, la microstructure homogène des composites à plis fins empêche la création de faisceaux de fibres de pontage et conduit à un ERR plus bas. Les résultats suggèrent que les fibres pontantes sont mieux ancrées en rupture intra- plutôt qu'inter-laminaire à cause de l'ondulation et d'un mauvais alignement des fibres, exerçant ainsi de plus grandes forces de fermeture qui expliquent le bien plus haut ERR mesuré en rupture intra- plutôt qu'inter-laminaire.

La ténacité en rupture translaminaire des laminés à plis croisés (CP) et quasi-isotropes (QI) est drastiquement diminuée entre les plis de $t=0.150$ et 0.030 mm, tant à l'initiation (-70%) qu'en régime permanent (-77%). La ténacité en rupture translaminaire varie linéairement avec l'épaisseur de pli et est mesurée $\sim 25\%$ plus

basse dans les éprouvettes QI en comparaison des éprouvettes CP correspondantes. Une étude morphologique des surfaces de rupture montrent que l'effet d'épaisseur de pli est directement corrélé à la hauteur des fibres arrachées, qui sont bien plus courtes dans les éprouvettes à plis fins.

Les ruptures inter-, intra- et trans-laminaire sont simulées par des modèles à éléments cohésifs, avec des diminutions linéaires de rigidité correspondant aux ERRs à l'initiation et des relations non linéaires identifiées représentant les ERRs associés aux mécanismes augmentant la ténacité. En rupture inter- et intra-laminaire, ces relations de traction-séparation liées au pontage de fibre sont identifiées avec une méthode efficace basée sur la courbe de résistance et développée au cours de ce travail. En rupture translaminaire, il est proposé de modéliser le mécanisme d'arrachage de fibres par une traction constante. Pour chaque mode de rupture, une stratégie de mise à l'échelle est suggérée afin de tenir compte des effets d'épaisseur de pli.

Des solutions potentielles pour augmenter la ténacité sont étudiées. Les résultats expérimentaux montrent que les stratégies d'hybridation de fibres et d'augmentation de la ténacité à l'interface entre les plis améliorent respectivement les ténacités en ruptures trans- et inter-laminaire, mais sont accompagnées d'une réduction de la contrainte à la rupture. Au contraire, le changement de combinaison fibre/matrice (T800/Aero2) offre une augmentation simultanée de la ténacité et de la contrainte à la rupture.

Mots-clés: Polymères renforcés de fibres de carbone, Composite à plis fins, Rupture interlaminaire (délamination), Rupture intralaminaire, Rupture translaminaire, Pontage de fibres, Arrachement de fibres, Modélisation par éléments finis, Éléments cohésifs.

Acknowledgements

I would like to express my gratitude to my thesis director Prof. John Botsis for the opportunity he offered me to work at the Laboratory of applied mechanics and reliability analysis (LMAF). I feel grateful for his continuous support, involvement and availability throughout the whole project and for his expertise in the publication procedures. I would also like to sincerely thank my thesis co-director Prof. Thomas Gmür for his involvement and interest in the conducted research.

I would like to express my deepest appreciation to Dr. Joël Cugnoni for his quasi-infinite scientific knowledge and the quality of his technical advice. He always kept his door open for invaluable discussions and for finding solutions at any kind of issues. Thank you also for the coffee supply management, which is one of the main reasons for the success of the projects at the LMAF.

I also want to thank my other colleagues of the “thin-ply” team, Robin Amacher, Sébastien Kohler and on the last months Alexandre Mordasini. Working on the same materials has stimulated a great cooperation, a healthy emulation among us and a close friendship.

A warm thank you also to Matteo Galli, Nassima Nasri, Marco Piccinini, Ebrahim Farmand-Ashtiani, Martin Rhême, Simon Joncas, Bruno Giuntoli, Mathieu Janier, Anne Legrand and Fernando Naya for the regular coffee and lunch breaks. These moments were essential in order to relax and talk about anything (including our respective projects). I was always much more effective after these convivial moments. I would also like to thanks Marco Borotto who was my first office mate, Georgios Pappas with whom I attended several conferences, Viviane Magnenat, and Luis Canal for the warm working environment.

I further need to acknowledge Martin Boesiger, Romain Conti, Simon Wicki and Cyrille Aeby who have accepted to work on projects under my supervision. Thank you for your respective valuable contributions to this thesis.

Acknowledgements

This work would not have been possible without our material supplier, North Thin Ply TPT (Renens, Switzerland). In particular, I would like to thank Olivier Thomassin and Yannick Prioux for their expertise, technical support and incredible responsiveness. Many thanks also to the team of the ATME and ATPR workshops for their contribution on machining the molds and specimens used throughout this work.

I cannot forget expressing my sincere thanks to my family, Catherine, Gabriel, Xavier, David and Diane for the support all along my studies. In particular, thank you 'Vati' for the daily phone calls and encouragements. Deepest thanks also to Chantal, André and Kamy, my second family since 2005. Many thanks also to Nicole Franc for the proofreading of the thesis. I would like to thank Giorgio Tondini who motivated me to write a PhD thesis. From wherever you are, I hope that you are proud of me.

Last but not least, I would like to express the warmest and deepest thanks to my sunshine, Philo. Thank you for having shared my life for so many years. Thank you for your unconditional and steadfast support. Thank you for being you.

Contents

Abstract	i
Résumé	iii
Acknowledgements	v
Contents	vii
List of Figures	xi
List of Tables	xix
List of Symbols	xxi
List of abbreviations	xxv
1. Introduction.....	1
1.1 Motivations.....	1
1.2 Objectives	3
1.3 Thesis outline	5
2. State of the art.....	7
2.1 Thin-ply laminated composite	7
2.2 Fracture mechanics approach	10
2.3 Interlaminar fracture (delamination)	12
2.4 Intralaminar fracture	15
2.5 Fiber bridging and traction-separation relations	16
2.6 Translaminar fracture	18
3. Materials and methods	21
3.1 Experimental procedure	21

Contents

3.1.1	Laminates manufacturing and specimen preparation.....	21
3.1.2	Material properties	27
3.1.3	Fracture tests and data reduction.....	28
3.1.4	Strain measurements by fiber Bragg grating (FBG) sensors	36
3.1.5	Digital image correlation (DIC) measurements.....	38
3.2	Mechanistic investigations	39
3.2.1	Fiber bridging characterization	39
3.2.2	Fiber pull-out characterization.....	40
3.3	Numerical procedure	41
3.3.1	Identification of bridging tractions in DCB specimens.....	41
3.3.2	Cohesive element modeling of DCB specimens.....	49
3.3.3	Cohesive element modeling of compact tension (CT) specimens	51
4.	Interlaminar fracture.....	55
4.1	Mode I experimental testing.....	55
4.1.1	Specimens and data reduction.....	55
4.1.2	Ply thickness effect.....	58
4.2	Mode II experimental testing.....	60
4.3	Mechanistic investigations	63
4.3.1	Microstructure analysis.....	64
4.3.2	Fiber bridging characterization	67
4.4	Numerical modeling	69
4.4.1	Mode I	69
4.4.2	Mode II	72
4.5	Summary.....	73
5.	Intralaminar fracture.....	75
5.1	Experimental testing	75
5.1.1	Specimens and Data reduction	75
5.1.2	Ply thickness effect.....	78
5.2	Mechanistic investigations	81

5.2.1	Microstructure analysis	82
5.2.2	Fiber bridging characterization.....	83
5.3	Numerical modeling	85
5.3.1	Identification of bridging tractions.....	85
5.3.2	Cohesive elements simulations	87
5.4	Summary	89
6.	Comparison between inter- and intra-laminar fracture.....	91
6.1	Experimental data.....	91
6.2	Mechanistic investigations	95
7.	Translaminar fracture	101
7.1	Experimental testing.....	101
7.1.1	Specimens and data reduction	101
7.1.2	Ply thickness effect	106
7.2	Mechanistic investigations	112
7.2.1	Cross-ply (CP) specimens.....	112
7.2.2	Quasi-isotropic (QI) specimens.....	117
7.3	Numerical modeling	119
7.3.1	Identification of bridging tractions.....	119
7.3.2	Cohesive elements simulations	121
7.4	Summary	124
8.	Improving the fracture toughness	127
8.1	Change of fiber/matrix combination	127
8.2	Use of interlayer toughener	130
8.3	Use of fiber hybridization	132
8.4	Summary	137
9.	Conclusions and perspectives	139
9.1	Summary and conclusions	139
9.2	Perspectives	144
References	147

Contents

Curriculum Vitae.....	159
------------------------------	------------

List of Figures

Fig. 1.1: Repartition of the carbon fiber consumption by domains of application (in tonnes). [2]	1
Fig. 1.2: Definition of inter-, intra- and trans-laminar fracture in laminated composites.	3
Fig. 1.3: Flowchart of the motivations and ways to address them.	6
Fig. 2.1: Airflow tow-spreading method [4].	7
Fig. 2.2: Onset of damage and ultimate tensile strength in unnotched QI specimens as a function of the ply thickness [3] (CLT stands for classical laminate theory).....	9
Fig. 2.3: Definition of the three basic fracture modes [24].....	11
Fig. 2.4: Available ERR and R-curves in a DCB specimen in (a) load controlled loading and (b) displacement controlled loading (adapted from [25]).	12
Fig. 2.5: Loading through compliant system (adapted from [25]).	12
Fig. 2.6: Sources of interlaminar fracture [24].	13
Fig. 2.7: Specimen configurations for interlaminar mode II testing [47].	15
Fig. 2.8: Fiber bridging in a DCB specimen for intralaminar fracture testing.	17
Fig. 3.1: Set-up for the curing of the composite plates.	24
Fig. 3.2: Temperature and external pressure set points.....	24
Fig. 3.3: Microstructure of an 8 mm thick plate with (a) low compaction and (b) good compaction (uncured stack sufficiently thick compared to the spacers).	25
Fig. 3.4: DCB, 4ENF and CT specimen configurations.	26
Fig. 3.5: (a) Compliance fitting with different functions; (b) Corresponding R-curves..	31
Fig. 3.6: Fixture for mode II experimental testing.....	32
Fig. 3.7: Schematic of a 4ENF specimen (adapted from [100]).....	33

List of Figures

Fig. 3.8: (a) Contour selected for the J-integral; (b) Three zones selected for the displacements fields fitting.	36
Fig. 3.9: Shift of the Bragg reflection peaks under compressive strain.	37
Fig. 3.10: (a) Targets for angle measurement in DCB specimens; (b) Speckle pattern, local window's size (in black) and both zones defined for DIC (yellow and blue).	39
Fig. 3.11: Schematic of the DCB specimen and transverse sections.	40
Fig. 3.12: Strain profile close to the crack tip in a representative $t=0.150$ mm DCB specimen for interlaminar fracture testing.	42
Fig. 3.13: Schematic representation of the model used in the static FE simulations. ..	43
Fig. 3.14: Schematic of the R-curve based fiber bridging identification method.	45
Fig. 3.15: Flowchart of the R-curve based fiber bridging identification method.	46
Fig. 3.16: For the interlaminar fracture of a $t=0.150$ mm M40JB/TP80EP specimen, data obtained from (i) the experiment, (ii) a R-curve based identification and (iii) a strain based identification: (a) Bridging tractions distributions; (b) Load-displacement curves; (c) Strain profile in the vicinity of the crack tip at steady-state; (d) R-curves. .	47
Fig. 3.17: (a) Load-displacement curves obtained from the R-curve based identification and linear distributions. (b) ERR values computed by integration of the identified bridging profile and linear distribution.	49
Fig. 3.18: Dissipated energy (a) in the fracture mechanics and (b) cohesive element approaches.	50
Fig. 3.19: Multilinear traction-separation relation. Illustration of the upper bound for the traction σ_2	51
Fig. 3.20: Identified traction-separation relation for a representative $t=0.075$ mm CP specimen.	52
Fig. 3.21: Simplified traction-separation relation for the CT specimens.	53
Fig. 4.1: DCB specimens with $h=2, 4$ and 8 mm ($t=0.150$ mm) for interlaminar fracture testing.	57
Fig. 4.2: For $t=0.150$ mm and $h=2, 4$ and 8 mm specimens, (a) crack length increment vs applied displacement and (b) crack speed vs crack length increment.	57
Fig. 4.3: Representative load-displacement curves as a function of the ply thickness ($h=4$ mm).	58

Fig. 4.4: Average R-curves for different ply thicknesses (color) and different specimen thicknesses (symbol).	60
Fig. 4.5: ERR at crack initiation (dark colors) and steady-state propagation (light color).	60
Fig. 4.6: Representative load-displacement curves as a function of the ply thickness (h=4 mm).	61
Fig. 4.7: Average R-curves for different ply thicknesses.	62
Fig. 4.8: Comparison of interlaminar fracture ERR under mode I and mode II loading (h=4 mm) at crack initiation (dark colors) and steady-state propagation (light colors).	63
Fig. 4.9: Side views of DCB specimens, where fiber bridging decreases with ply thickness (h=4mm).	64
Fig. 4.10: (a)-(c) Representative cross sections for the three ply thicknesses; (d) Corresponding coarseness values.	65
Fig. 4.11: Cross sections of t=0.030 and 0.150 mm fractured specimens.	66
Fig. 4.12: Development of a fiber bridging bundle in a t=0.150 mm specimen. The ellipses show consecutive stages of the bundle.	67
Fig. 4.13: Crack profile and bridging fibers / bundles.	67
Fig. 4.14: Number of isolated bridging fibers and fibers clustered in bundles per millimeters of crack width.....	68
Fig. 4.15: Fiber bridging traction-separation profiles as a function of the ply thickness (h=4 mm). The thinner lines represent the identification based on the mean R-curves plus/minus the standard deviation.	70
Fig. 4.16: Split of the cohesive relation.	71
Fig. 4.17: Experimental and simulated load-displacement curves under mode I loading. (see text for details).	72
Fig. 4.18: Experimental and simulated load-displacement curve for a t=0.150 mm specimen loaded in mode II.	73
Fig. 5.1: CT specimen and DCB specimens with h=6 and 10 mm (t=0.0750 mm) for intralaminar fracture testing.	77
Fig. 5.2: For CT and DCB (h=6 and 10 mm) specimens, (a) crack length increment vs applied displacement and (b) crack speed vs crack length increment.	77

List of Figures

Fig. 5.3: Representative load-displacement curves as a function of the ply thickness for (a) DCB specimens ($h=6$ mm) and (b) CT specimens (light colors indicates the data not considered in the data reduction).	78
Fig. 5.4: Average R-curves for different ply thicknesses (color) and different specimen configurations (symbol). The insert shows the R-curve for the CT specimens.	80
Fig. 5.5: ERR at crack initiation (dark colors) and steady-state propagation (light color).	81
Fig. 5.6: Side views of (a) DCB specimens showing less fiber bridging with decreasing ply thickness ($h=4$ mm) and (b) a CT specimen.	82
Fig. 5.7: Representative transverse sections for the three ply thicknesses. Please note that the crack plane is horizontal on these images.	83
Fig. 5.8: Crack profile and bridging fibers / bundles.	84
Fig. 5.9: Number of isolated bridging fibers and fibers clustered in bundles per millimeters of crack width.	84
Fig. 5.10: Traction-separation relations as a function of ply thickness t for (a) $h=6$ and (b) $h=10$ mm.	86
Fig. 5.11: (a) Traction-separation relations obtained with both identification methods; (b) Load-displacement curves, (c) strain profiles and (d) crack length increments obtained experimentally and numerically.	87
Fig. 5.12: Experimental and simulated load-displacement curves for DCB specimens with different ply thicknesses.	88
Fig. 5.13: Experimental and simulated load-displacement curves for CT specimens with different ply thicknesses.	89
Fig. 6.1: Average R-curves for different ply thicknesses (color) in inter- and intra-laminar fracture (symbol).	92
Fig. 6.2: ERR at crack initiation (dark colors) and steady-state (light colors) for inter- and intra-laminar fracture.	93
Fig. 6.3: Traction-separation relations as a function of ply thickness t for interlaminar fracture ($h=4$ mm) and intralaminar fracture ($h=6$ mm).	94
Fig. 6.4: For the inter- and intra-laminar fracture, linear scaling relations as a function of ply thickness for (a) bridging ERR at steady-state, (b) the maximal bridging traction,	

(c) the exponential decay parameter and (d) the COD at the end of the bridging zone.	95
Fig. 6.5: Representative crack profiles and bridging fibers for different ply thicknesses t in specimens tested in inter- and intra-laminar fracture.....	96
Fig. 6.6: Schematic view of the ply orientation, micro-cracking, crack tortuosity and bundle aspect ratio in (a) inter- and (b) intra-laminar fracture.....	97
Fig. 6.7: Average equivalent diameter, major axis length and minor axis length for the ten largest bridging bundles in each ply thickness.	97
Fig. 6.8: (a) Number of isolated bridging fibers (dark colors) and bridging fibers in bundles (light colors); (b) Steady-state ERR as a function of number of bridging fibers.	98
Fig. 6.9: Fiber misalignment in inter- and intra-laminar fracture.	100
Fig. 6.10: Average closing tractions per bridging fibers in inter- and intra-laminar fracture ($z \approx 3$ mm).....	100
Fig. 7.1: Compact tension configuration adapted for opening displacement measurement with an extensometer.	102
Fig. 7.2: Representative load-displacement curves as a function of the ply thickness in CP and QI specimens ($a_0 \approx 25$ mm).....	107
Fig. 7.3: Two loading-unloading cycles up to a noncritical displacement in a selected $t=0.150$ specimen.	108
Fig. 7.4: Average R-curves for different ply thicknesses in CP and QI laminates.....	109
Fig. 7.5: ERR at crack initiation (dark colors) and “steady-state” propagation (light colors).....	110
Fig. 7.6: Propagation of the crack in the $\pm 45^\circ$ plies by succession of splitting and fiber failure.	111
Fig. 7.7: Representative view of the fracture surface in the CT CP specimens with (a) $t=0.030$ mm, (b) $t=0.075$ mm, (c) $t=0.100$ mm and (d) $t=0.150$ mm. The arrow indicates the double 90° ply at the center of the specimens.....	113
Fig. 7.8: Representative surface profile in 0° plies of CP CT specimens for different ply thicknesses.	114
Fig. 7.9: Schematic of the crack starter and crack profiles in the 0° and 90° plies.	115

List of Figures

Fig. 7.10: Histogram of the height of the top envelope profile as a function of ply thickness and corresponding fitted normal distributions.	116
Fig. 7.11: Correlation between ply thickness and mean pull-out height.	116
Fig. 7.12: Representative view of the fracture surface in the CT QI specimens with (a) $t=0.030$ mm, (b) $t=0.075$ mm, (c) $t=0.150$ mm. (d) For comparison, CT CP specimen with $t=0.150$ mm.....	118
Fig. 7.13: Representative crack profile in four successive plies of a QI $t=0.150$ mm specimen.	119
Fig. 7.14: For the CP and QI specimens, linear scaling as a function of ply thickness of (a) the pull-out tractions, (b) the initiation ERR, (c) the steady-state ERR, (d) the unnotched strength and (e) the maximal COD.....	121
Fig. 7.15: Experimental and simulated load-displacement curves for CP specimens.(see text for details).....	123
Fig. 7.16: Simulation of the load-displacement curve of a selected $t=0.150$ mm specimen with a reduced shear modulus. (see text for details)	123
Fig. 7.17: Experimental and simulated load-displacement curves for QI specimens.(see text for details).....	124
Fig. 8.1: Onset of damage and ultimate tensile strengths for different ply thicknesses and fiber / matrix combinations (adapted from [112]).	128
Fig. 8.2: Mode I ERR at crack initiation and in average on 100 mm of propagation in interlaminar fracture. (See text for details).....	129
Fig. 8.3: Average R-curves of QI laminate for different ply thicknesses and fiber / matrix combinations.	130
Fig. 8.4: CAI strength for different fiber / matrix combinations and IT. IT 1/n refers to IT every n layers. (adapted from [112])	131
Fig. 8.5: Mode II average ERR on 40 mm of propagation in interlaminar fracture of different fiber / matrix combinations and amount of IT.	132
Fig. 8.6: Schematic view of the T800 / HR40 (a) $0^\circ/0^\circ$ and (b) $0^\circ/90^\circ$ hybrid (adapted from [112]).	134
Fig. 8.7: Averaged stress-strain curves for the T800 / Aero2 and T800 / HR40 QI hybrid laminates in unnotched tension. The dots for ultimate strength of the hybrid represent the elastic part of the strain (adapted from [112]).....	135

Fig. 8.8: Average R-curves of QI laminate for the T800 / Aero2 and hybrid laminates. The dashed line represent the rule of mixture between the T800 / Aero2 ($t=0.067$ mm) and M40JB / TP80EP ($t=0.030$ mm).	136
Fig. 8.9: Strength (onset of damage) vs translaminar fracture toughness (at crack initiation) for the different systems studied in this work.	138
Fig. 9.1: Normalized inter-, intra- and trans-laminar fracture toughness as a function of ply thickness. (* Values normalized by the steady-state ERR at $t=0.150$ mm of the corresponding fracture orientation)	141

List of Figures

List of Tables

Table 3.1: Produced laminate plates.....	23
Table 3.2: M40JB/TP80EP lamina level properties, normalized for 55% fiber volume fraction [3].....	27
Table 3.3: M40JB/TP80EP laminate level stiffness properties (in-plane equivalent moduli from CLT).....	28
Table 3.4: Compliance fitting and corresponding ERR values.....	31
Table 4.1: Dimensions of the specimens for interlaminar fracture testing.	56
Table 4.2: Interlaminar fracture specimen's dimensions	61
Table 4.3: Identified fiber bridging parameters for different ply thicknesses (h=4 mm)	70
Table 5.1: Dimensions of the specimens for intralaminar fracture testing.	76
Table 5.2: ERR computed with compliance calibration and J-integral for initiation by loss of linearity ($G_{I,i,NL}$), visual initiation ($G_{I,i,vis}$ and $J_{I,i,vis}$) and steady-state ($G_{I,ss}$ and $J_{I,ss}$).....	81
Table 5.3: Identified fiber bridging parameters for different ply and specimen thicknesses.	86
Table 6.1: Identified fiber bridging parameters for the different ply thicknesses in inter- and intra-laminar fracture.....	94
Table 7.1: Dimensions of the specimens for translaminar fracture testing.	103
Table 7.2: Fracture toughness of the 0° plies.	111
Table 7.3: Fracture toughness of the ±45° plies.	111
Table 7.4: Mean, standard deviation and extreme values of the top and bottom envelope profiles as a function of ply thickness.	116
Table 7.5: Traction-separation parameters for the translaminar fracture.	120

List of Tables

List of Symbols

a	Crack length
a_0	Initial crack length
a_{eff}	Effective crack length
b	Specimen's width
B	Plate's width
C	Specimen's compliance
\mathbf{C}^*	Stiffness matrix of orthotropic plane stress material
d	Distance between the loading points in 4ENF tests
dE_{coh}	Element of dissipated energy in the fracture mechanics approach
dE_{FM}	Element of dissipated energy in the cohesive zone approach
ds	Infinitesimal element of contour
dx_i	Infinitesimal length in direction i
D	Damage parameter
E_i	Young's modulus in direction i
erf	Error (objective) function
f	Dimensionless function
F	Applied work
g	Grammage of fiber per ply (also called fiber areal weight)
G	ERR or crack driving force
G_{ij}	Shear modulus in plane ij
G_I, G_{II}, G_{III}	ERR in mode I, II and III respectively

List of Symbols

$G_{I,i}$	Mode I ERR at initiation
$G_{I,b}$	Mode I ERR associated with bridging
$G_{I,tot}$	Total ERR
$G_{I,ss}$	Mode I steady-state ERR
h	Specimen's thickness (direction normal to the crack plane)
H	Plate's thickness
J	Nonlinear ERR (the use of indices l, i, b, tot and ss is similar as for G)
k	Stiffness of a spring
K	Stress intensity factor
l	Specimen's length
L	Plate's length
l_c	Critical fragmentation length
$M_{1,...,3}$	Fitting parameters
n_p	Number of plies
$N_{1,...,9}$	Fitting parameters
p_e	Experimental optomechanical grating gage factor
P	Load
P_c	Critical load
S	Strength
t	Ply thickness
u_i	Displacement in direction i
U	Strain energy
v_f	Fiber volume fraction
w	Strain energy density
z	Distance from the crack tip
z_{max}	Bridging zone length

$\gamma, \hat{\gamma}$	Exponent in traction-separation profiles
Γ	Contour in J-integral computation
Δ	Cross-head (applied) displacement
δ	COD
$\hat{\delta}$	COD at the end of matrix cracking zone
$\bar{\delta}$	COD at the crack starter
δ_i	COD discretization
δ_m	COD at the end of the pull-out zone
δ_{\max}	COD at the end of the bridging zone
ε_{ij}	Strain in direction j on face normal to i
ε_{exp}	Experimental strain
ε_{FE}	Numerical strain
θ	Relative angle between both DCB arms at the loading points
$\lambda_{B,i}$	Bragg wavelength of sensor i
$\lambda_{B0,i}$	Initial Bragg wavelength of sensor i
ν_{ij}	Poisson's ratio in plane direction ij
Π	Potential energy
ρ_f	Fiber's density
σ_c	Critical strength of cohesive elements
$\sigma_b(z)$	Bridging tractions over distance from crack tip
$\hat{\sigma}_b(\delta)$	Bridging tractions over COD
σ_{ij}	Stress in direction j on face normal to i
σ_{\max}	Maximum bridging traction
σ_p	Pull-out traction

List of Symbols

τ_y Shear strength

List of abbreviations

2D	Two dimensional
3D	Three dimensional
4ENF	Four point end notched flexure
ASTM	American society for testing material
CAI	Compression after impact
CC	Compliance calibration
CC3	Compliance calibration with three parameters
CCD	Charge-coupled device
CFRP	Carbon fiber reinforced polymer
CLT	Classical laminate theory
CNC	Computer numerical control
COD	Crack opening displacements
CP	Cross-ply
CT	Compact tension
DCB	Double cantilever beam
DCC	Double compliance calibration
DIC	Digital image correlation
ELS	End loaded split
ENF	End notched flexure
ERR	Energy release rate
FBG	Fiber Bragg grating

List of abbreviations

FE	Finite element
IT	Interlayer toughener
LEFM	Linear elastic fracture mechanics
LMAF	Laboratory of Applied Mechanics and Reliability Analysis
LVDT	Linear variable differential transformer
MCC	Modified compliance calibration (DCB specimens)
MCC2	Modified compliance calibration (CT specimens)
NTPT	North Thin Ply Technology
PTFE	Poly-tetrafluoroethylene
QI	Quasi-isotropic
R-curve	Resistance-curve (ERR vs crack length)
RSFP	Reactive super fine particles of polyethersulfone
SENF	Stabilized end notched flexure
SIF	Stress intensity factor
UD	Unidirectional

Chapter 1

Introduction

1.1 Motivations

The demand for fiber reinforced polymers is continuously increasing to meet the high demands for light and strong materials. Such a trend is motivated by the desire to reduce the ecological impact of the transportations systems and the willingness to reach performances that were unachievable previously. For instance, the composite materials represent 50% in weight of the new aircraft generation, offering weight saving of 20% compared to designs with conventional materials [1]. As shown, in Fig. 1.1, carbon fiber reinforced polymers (CFRPs) are mostly used in aerospace and defense applications, followed by wind turbines, sports, molding and automotive applications.

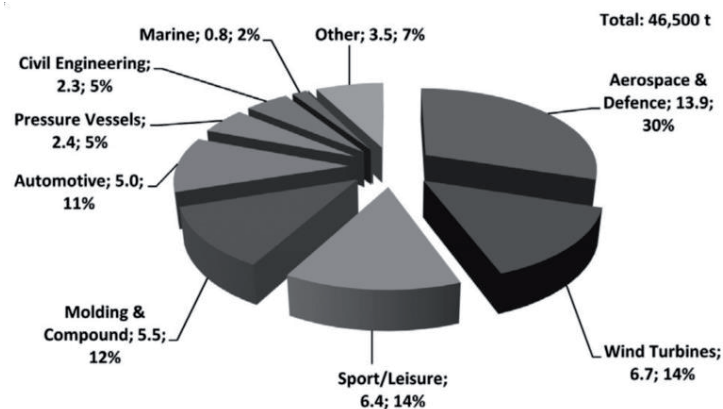


Fig. 1.1: Repartition of the carbon fiber consumption by domains of application (in tonnes).

[2]

The CFRPs are extensively used for their very high specific modulus and strength. Thanks to a much lower density, CFRPs have better specific stiffness and strength properties compared to metals. Among the CFRPs, thin-ply laminates made out of

particularly thin layers (from 0.015 to 0.150 mm) are gaining in interest. Such ply thicknesses enlarge the design space, since more plies orientations can be selected to optimize the mechanical properties in the directions with higher loads. This benefit is particularly important in thin-structures or sandwich skins, where quasi-isotropic or oriented laminates can advantageously replace basic cross-ply laminates without ignoring design rules such as the laminate's symmetry and balance. A second advantage is the delayed onset of damage and enlarged ultimate tensile strength of the thin-ply laminates compared to standard composites [3, 4]. This size effect is attributed to a change of failure mode, from accumulation of damage to brittle failure. Due to the reduction of damage development, the fatigue behavior of thin-ply composites is also remarkable [3, 4].

However, due to the transition towards a quasi-brittle fracture behavior without delamination, the improvement of strength properties is generally accompanied by a reduction of the composite toughness. Even if the design methods are in most of the cases based on strain or stress criteria, the resistance to fracture is of paramount importance to assess the safety of advanced structures. Traditionally, the detection of the first-ply failure was synonymous of the end of life of the structure. However, recent advances in damage tolerant design and maintenance programs account for the possible presence of cracks in the laminated composites. The fundamental motivation is to plan periodic inspections for detecting cracks before they reach critical lengths. Such a maintenance program requires a deep understanding of the fracture behavior in the composite materials.

Cracks may appear in laminated composites for several reasons. Among the main ones, one can mention the defects and damage caused during manufacturing processes, impact loadings, out-of-plane and in-plane unexpected overloading, cyclic loadings producing fatigue damage, and structural discontinuities or stress concentrator features. In unidirectional composite laminates the cracks can grow in three basic orientations, as schematized in Fig. 1.2. (i) The interlaminar fracture, also called delamination, is the debonding of two successive plies. It is generally caused by out-of-plane loadings and is one of the main weaknesses of laminated structures. (ii) The intralaminar fracture is a failure mode, where the crack propagates within the laminae of a laminate, parallel to the fibers [5]. It can be caused by impact loading conditions and often appears together with interlaminar fracture [6]. (iii) The translaminar fracture is perpendicular to the fibers. It requires therefore much more energy to propagate than the inter- and intra-laminar fracture. Translaminar fracture

is caused by excessive in-plane loading conditions or structural discontinuities such as holes.

The crack initiation and growth in any of these orientations may lead to the ruin of the structure's integrity. To optimize the design of structures with thin-ply composites it is therefore mandatory to quantify and understand the effects of ply thickness on these different failure modes. Based on experimental characterizations, numerical models can be implemented to accurately predict the fracture behavior for laminates of different ply thicknesses. A better understanding of the failure mechanisms would enable a reduction of the safety factors and thus design even lighter and safer structures. Moreover, the fracture prediction can be used to plan periodic inspections and limit the costs in maintenance. Finally the developed models can contribute to a better understanding of the damage mechanisms and size effects in thin-ply laminates.

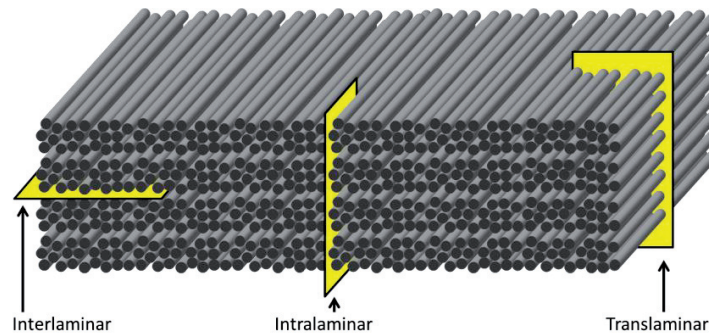


Fig. 1.2: Definition of inter-, intra- and trans-laminar fracture in laminated composites.

1.2 Objectives

The outstanding strength properties of thin-ply composites have been extensively studied in the past few years. Despite these proven advantages, the study of their fracture properties and their relative brittleness has received a limited attention. However, it represents an important performance limitation that needs to be understood and improved. Indeed, the trade-off between strength and fracture properties governs the choice of the optimal ply thickness and defines where thin-ply composites can be used. Therefore, it is necessary to acquire a thorough understanding of the parameters and mechanisms affecting the fracture properties. The inter-, intra- and trans-laminar fracture toughness of laminated CFRPs made of conventional ply thicknesses (larger than $t=0.150$ mm) have been studied for different fiber/matrix combinations and different specimen's geometry. However, there is a

lack of studies concerning a detailed understanding of the influence of the ply thickness on each of these three fracture orientations in thin-ply laminates. In particular, the following questions need to be addressed:

- How does the ply thickness affect the fracture toughness and resistance-curve (R-curve) behavior of thin-ply composites for the different fracture orientations?
- Which mechanisms can explain the observed size effects and what are the dominant parameters governing this behavior?
- How does interlaminar fracture differ from intralaminar fracture and what are the causes of such differences?
- How much is the fracture toughness reduced for translaminar cracks in cross-ply (CP) or quasi-isotropic (QI) laminates made of very thin-ply?
- How can the ply thickness effects be accounted for in the modeling and prediction of fracture in thin-ply composites?
- What are the possible solutions to overcome these limitations while keeping the thin-ply advantages?

In view of the above questions, the objectives of this thesis consist in understanding and characterizing the effects of ply thickness on the fracture in a carbon-epoxy laminate, under monotonic loading by considering a single material (M40JB/TP80ep) and keeping all specimen dimensions constant except for the ply thickness which varies from standard-ply ($t=0.150$ mm) to very thin-ply ($t=0.030$ mm). This main objective is addressed through three main components:

- The interlaminar mode I, interlaminar mode II, intralaminar mode I and translaminar mode I fracture toughness at initiation and subsequent crack growths in at least three ply thicknesses are characterized experimentally. In addition, the effect of specimen thickness is studied through selected experiments in inter- and intra-laminar mode I fracture.
- Mechanistic investigations in order to identify the dominant toughening mechanisms leading to the ply thickness effects such as fiber bridging in inter- and intra-laminar fracture and fiber pull-out in translaminar fracture are carried out.
- The inter-, intra- and trans-laminar crack growths are simulated with cohesive element models using traction-separation relations identified based on the R-curves obtained experimentally.

1.3 Thesis outline

After the introduction presenting the motivations and objectives (chapter 1), the thesis is organized according to the following structure:

- Chapter 2 provides a literature review of the state of the art on thin-ply composites. It also presents the general concepts of fracture mechanics and the methods for the inter-, intra- and trans-laminar fracture testing. Finally, it also describes the numerical model techniques.
- Chapter 3 details the materials, manufacturing and experimental testing procedures. In particular, the specimen configuration and data reduction scheme are described for each of the three fracture orientations. The strain acquisition technique and full-field displacement measurement tools are also presented in this chapter. The different mechanistic investigation techniques employed to explain the causes of the ply thickness effects are also described. Finally, this chapter presents a new fiber bridging tractions identification procedure based on the R-curve and covers the proposed numerical modeling techniques for fracture predictions.
- Chapter 4 is dedicated to the characterization of the interlaminar fracture under mode I and II in monotonic loading conditions. The microstructure of the laminate and fiber bridging behaviors (in mode I) which are deemed to be responsible for the ply thickness effect are evaluated. The traction-separation relations associated with fiber bridging are identified for the different ply thicknesses and subsequently implemented in cohesive element simulations.
- Chapter 5 follows a similar approach as in chapter 4, but for the characterization, understanding and modeling of the mode I intralaminar fracture.
- Chapter 6 addresses the comparison of inter- and intra-laminar fracture which both share similarities in terms of crack propagation mode and fiber bridging development along the direction of the fibers. Potential mechanisms are proposed to explain the differences observed in the experimentally obtained R-curves and bridging ligament morphology.
- Chapter 7 deals with the characterization of the translaminar fracture in cross-ply (CP) and quasi-isotropic (QI) laminates. The fracture toughness at initiation and subsequent crack growth are measured by J-integral calculations based on full-field displacement measurements. The shape and amount of fiber pull-out

as a function of the ply thickness is analyzed to provide an explanation of the scaling effect. Finally, cohesive element models are implemented to predict the crack propagation and global response under in-plane loading conditions.

- Chapter 8 investigates solutions to improve the fracture toughness of thin-ply CFRPs. Through selected experiments, it is shown how the change of fiber/matrix combination, the use of interlayer toughener and the development of fiber hybridization techniques can raise the fracture toughness.
- Chapter 9 summarizes the effects of ply thickness on the inter-, intra- and trans-laminar fracture and presents the future work perspectives.

The flowchart in Fig. 1.3 summarizes the questions highlighted in the objectives and the ways they are addressed. The numbers in bold characters refers to the corresponding sections numbers.

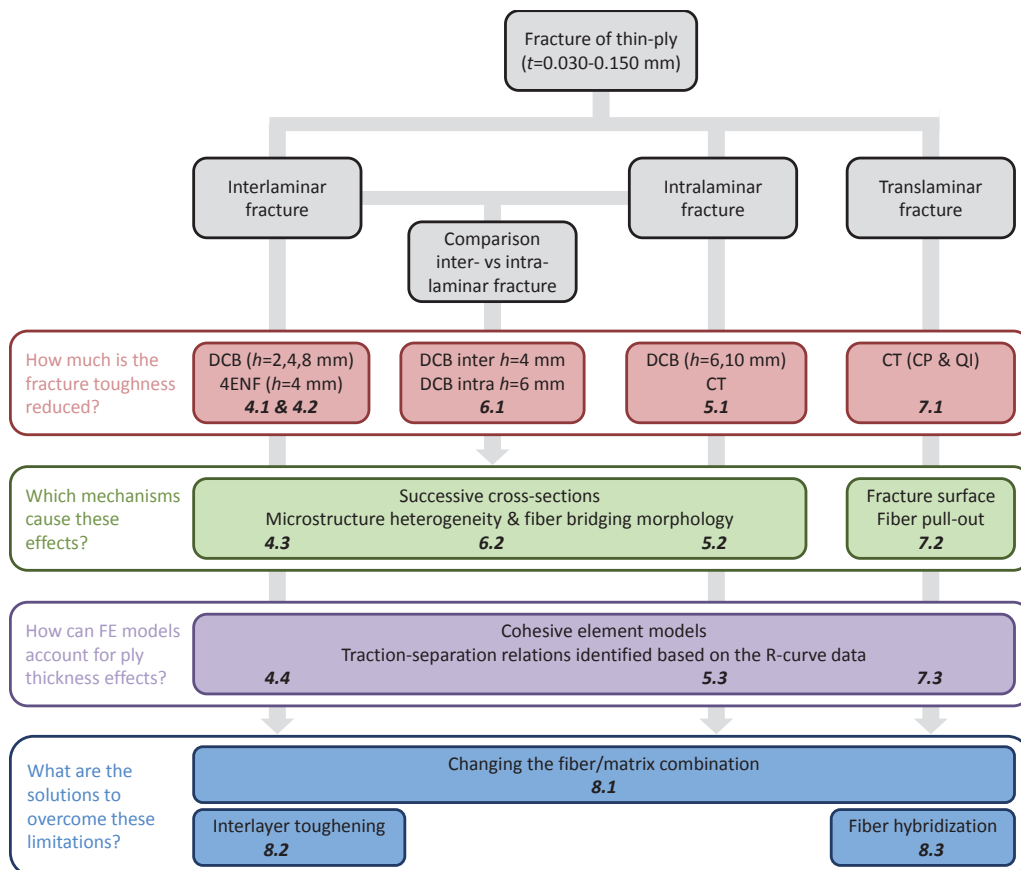


Fig. 1.3: Flowchart of the motivations and ways to address them.

Chapter 2

State of the art

2.1 Thin-ply laminated composite

The demand for thin-ply laminates is continuously increased by the aeronautics and sport industry. Therefore, the technology is progressively developed, leading to current production of thin-ply down to 0.015 mm [7]. In thin-ply composites, the fiber bundles are thinner and better scattered in the in-plane direction than in standard composites. It results in a more homogenized microstructure. Moreover, the impregnation of the fiber with the resin is claimed to be better controlled [8]. The spreading of the fiber tows to produce thin-ply fabrics can be achieved by several methods. Among them, one can cite a patented mechanical technique using rotating wheels with perpendicular teeth [9] and a technique based on ultrasonic waves [10]. Another method first proposed by Kawabe et al. [11] and further developed by Sihni et al. [4] uses the aerodynamic force created by an airflow to spread the tows (Fig. 2.1). Using this technique, the tows can be spread continuously and the fibers are not damaged by the airflow [4]. This technique is used by North Thin Ply Technology (NTPT) in Renens, Switzerland to produce the preregs used in this study.

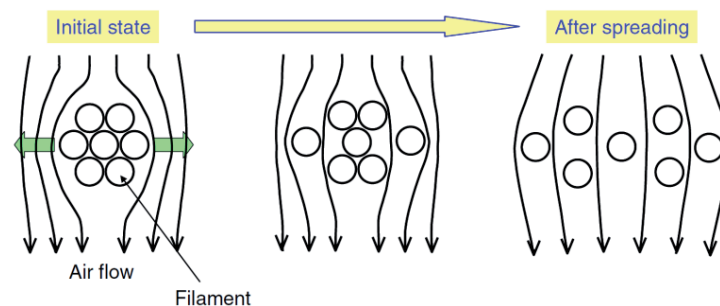


Fig. 2.1: Airflow tow-spreading method [4].

Thin-ply composite laminates are gaining in interest not only because of the enlarged design space they offer, but also for their improved strength and fatigue properties. The first comprehensive study on thin-ply composite was done by Sih et al. [4] who investigated the difference between thin-ply ($t=0.04$ mm) and thick-ply ($t=0.20$ mm). They noticed a higher ultimate strength (+10%) in the thin-ply QI unnotched specimens subjected to monotonic tension. While an accumulation of damage was detected in the thick-ply specimens before failure, the thin-ply specimens remained linear until a brittle fracture. Similarly, the thin-ply specimens exhibited a better resistance to fatigue loading, thanks to the limited development of damage at the free-edges. In open-hole specimens, the thick-ply laminates failed at slightly higher ultimate strength because the development of damage around the notch reduced the stress concentration. Finally, the thin-ply specimens were much less delaminated than thick-ply ones after impact, leading to a delayed buckling in post-impact compression.

Similarly, Yokozeki et al. [12] noticed superior properties of thin-ply ($t=0.075$ mm) compared to thick-ply ($t=0.145$ mm) laminates in monotonic tension, tension-tension fatigue, non-hole compression, open-hole compression and compression after impact tests. Yokozeki et al. [13] also investigated the resistance of thin-ply composites subjected to out-of-plane loading. While multiple matrix cracks and a large amount of delamination led to the failure of the thick-ply laminate, fiber fracture occurred in thin-ply specimens. Wisnom et al. [14] also show a ply thickness effect on the strength of unnotched QI specimens by comparing sublaminates scaling and ply level scaling. These two scaling strategies give drastically different strength values.

Amacher et al. [3] reported a linear increase in the stress at onset of damage and ultimate strength over a large range of ply thicknesses ($t=0.030$ to 0.300 mm), as shown in Fig. 2.2. While in the thin-ply laminate the onset of damage was delayed until the ultimate strength and the specimens failed in a brittle manner, damage started accumulating at a lower stress level in thick-ply laminates leading to an overall lower ultimate strength. The apparition of transverse cracks and delamination appears to be suppressed or at least delayed in the thin-ply laminates. Such effect is caused by the constraints imposed by the neighboring plies that limit the elastic energy available for crack initiation and propagation. In open-hole configuration, due to the delayed onset of damage, the thin-ply specimens could not relax the stress concentrations and thus failed at lower stress than the thick-ply. However, the delayed onset of damage offers a better resistance to fatigue loading in thin-ply compared to thick-ply specimens. These observations confirm the trends highlighted

in the previous studies about notched (open-hole) specimens [4, 12, 15, 16]. The damage sequence and failure behavior in open-hole non crimp fabric thin-ply specimens is found by Arteiro et al. [17] similar as in specimens made out of unidirectional thin-ply prepregs [3, 4]

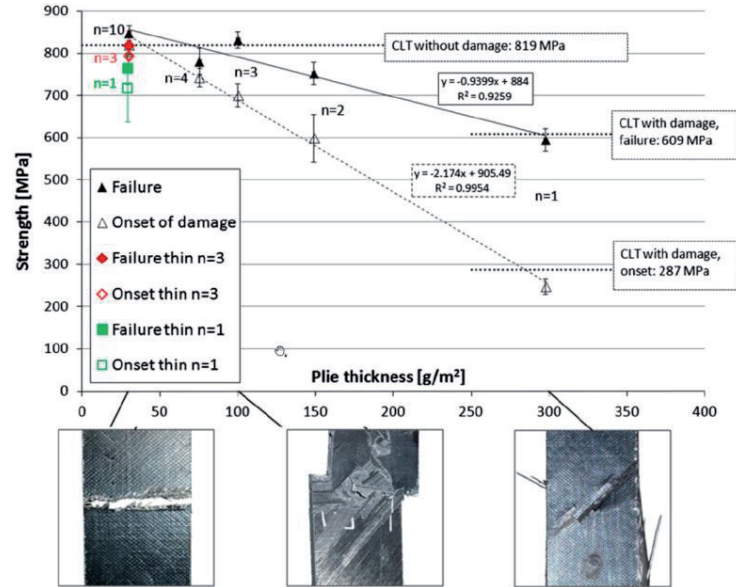


Fig. 2.2: Onset of damage and ultimate tensile strength in unnotched QI specimens as a function of the ply thickness [3] (CLT stands for classical laminate theory).

The transverse tensile and in-plane shear strength properties of a ply are affected by the constraints imposed by the adjacent plies. Therefore, the strength properties of a ply in a laminate depend on the ply thickness t and follow approximately a relation in $1/\sqrt{t}$. This effect is conceptualized by Camanho et al. [18] as the in-situ strength of a ply. Consequently, for very low ply thicknesses the critical strain leading to transverse cracking and in-plane shear cracking increases so much that the final failure becomes dominated by the fiber ultimate strain in the thinnest plies (about $t=0.030$ mm for M40JB / TP80EP). In addition to their thickness, the location of the plies in the laminate is also shown to considerably affect the strength properties [19].

Lots of works about thin-ply composites focus on the strength properties of notched and unnotched specimens. They highlight the change of failure mechanisms from extensive damage development in thick-ply laminates to brittle failure in thin-ply laminates. However, only a few studies address directly the measurement of the toughness properties. In particular, the influence of ply thickness on the inter- and intra-laminar fracture has not been investigated yet (see sections 2.3 and 2.4). The

thin-ply effect on the translaminal fracture of CP specimens has been studied only recently (see section 2.6).

2.2 Fracture mechanics approach

Classical failure criteria assume perfect materials free from defects and thus fail to predict failure in structures containing a crack. Fracture mechanics, which is the subject of engineering science concerned with the study of crack initiation and propagation leading to failure in solids, proposes two fracture criteria: (i) the crack tip stress field (local) and (ii) the energy balance approach (global) [20].

When linear elastic fracture mechanics (LEFM) conditions are fulfilled (i.e. the process zone is small compared to the singular stress field), the stress field around a crack is defined as $\sigma_{ij}(r, \theta) = K(2\pi r)^{-1/2} f_{ij}(\theta)$, where $f_{ij}(\theta)$ is a dimensionless function of the angle θ , r is the radial distance from the crack tip and K is the stress intensity factor (SIF) which depends on the applied load and crack geometry. A crack starts growing when the SIF becomes equal to the critical SIF determined experimentally and called fracture toughness K_c (MPa \sqrt{m}) [21].

The global approach considers that the energy required to create new surfaces corresponds to the decrease in the potential energy, as proposed by Griffith [22]:

$$G = -\frac{1}{b} \frac{d\Pi}{da} = 2\gamma \quad (2.1)$$

Here Π is the potential energy of the system, a the crack length and γ the surface energy. This drop of potential energy is defined as the energy release rate (ERR) by Irwin [23] and is also called crack driving force. The crack propagates when the ERR reaches the critical ERR G_c (J/m²) measured experimentally. For linear elastic materials both criteria (K_c and G_c) are related by a bijection [20]. In this work, only propagation points are considered. Therefore, the word “critical” and the subscript “c” are omitted in the presentation of the results.

In cases where LEFM is not valid and nonlinear effects must be accounted for, one can use another fracture parameter introduced by Rice: the J-integral. This path independent contour integral is an extension of the ERR for nonlinear and elastic-plastic deformation. It is equal to the ERR G when the validity of LEFM is verified.

In fracture mechanics, three basic fracture modes are defined, depending on the loading direction (Fig. 2.3): (i) the mode I is the opening of the crack faces normal to the crack plane; (ii) the mode II is the in-plane sliding (shearing direction perpendicular to crack front); and (iii) the mode III is the out-of-plane shearing (tearing direction parallel to crack front). The subscript I, II, or III is generally appended to the critical fracture toughness K_c and ERR G_c to specify the loading mode considered. In practice, the crack propagation can occur under combination of these loading modes and are treated as mixed-mode cases of the basic modes.

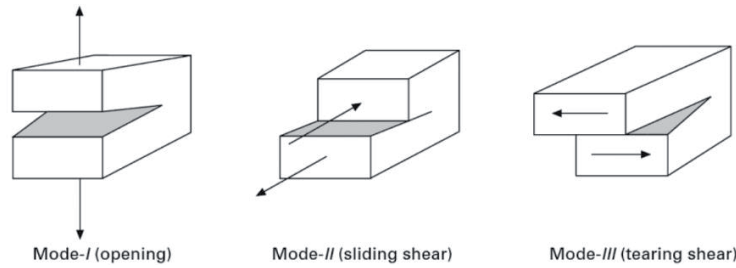


Fig. 2.3: Definition of the three basic fracture modes [24].

While for brittle materials, the ERR remains constant with crack growth, in some materials the resistance to fracture increases with crack advance due to toughening mechanisms such as plasticity, fiber bridging or fiber pull-out. Such a behavior is generally depicted in the ERR vs crack length increment plot called resistance curve (R-curve). If steady-state propagation is reached, meaning that the crack propagates in a self-similar manner, the R-curve reaches a plateau level. Fig. 2.4 represents R-curves superimposed with available ERR for load and displacement imposed conditions in a double cantilever beam (DCB) specimen. A crack grows in a stable manner only if the rate of change in the available ERR (crack driving force) is smaller than the slope of the R-curve (eq. (2.2)):

$$\frac{\partial G}{\partial a} < \frac{\partial G_c}{\partial a} \quad (2.2)$$

While the crack propagation is unconditionally stable in displacement controlled loading, the crack growth becomes unstable after a small crack increment in load controlled loading even if the material exhibits an R-curve behavior due to a toughening mechanism. In most applications the loading is an intermediate state between load and displacement control and can be represented by the force imposed with a spring loaded in displacement control (Fig. 2.5). The loading of the solid is in displacement control when the stiffness of the spring tends to infinity and in load control when the stiffness tends to zero. In practice, specimens for the fracture

toughness testing are loaded under displacement controlled conditions to grow the crack in a stable manner. However, the rigidity of the machine and experimental set-up must be much larger than the rigidity of the specimen to guaranty a stable propagation.

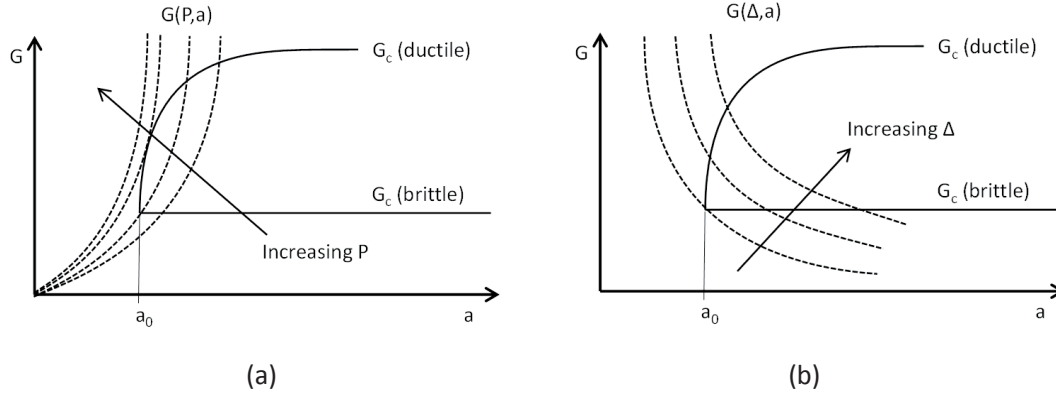


Fig. 2.4: Available ERR and R-curves in a DCB specimen in (a) load controlled loading and (b) displacement controlled loading (adapted from [25]).

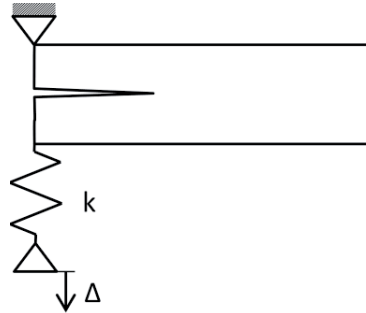


Fig. 2.5: Loading through compliant system (adapted from [25]).

2.3 Interlaminar fracture (delamination)

Interlaminar fracture, also called delamination is one of the most critical fracture mechanisms in laminated composites. Indeed, the debonding of successive layers may ruin the integrity of a multilayer composite structure, since it suppresses the capacity of the laminate to share load between laminae. Interlaminar fracture most commonly occurs at structural discontinuities and in regions subjected to out-of-plane bending, as illustrated in Fig. 2.6 [8, 24]. As a consequence, interlaminar fracture has received lot of attention in the literature and is the object of review papers [26, 27] and textbooks [28].

2.3 Interlaminar fracture (delamination)

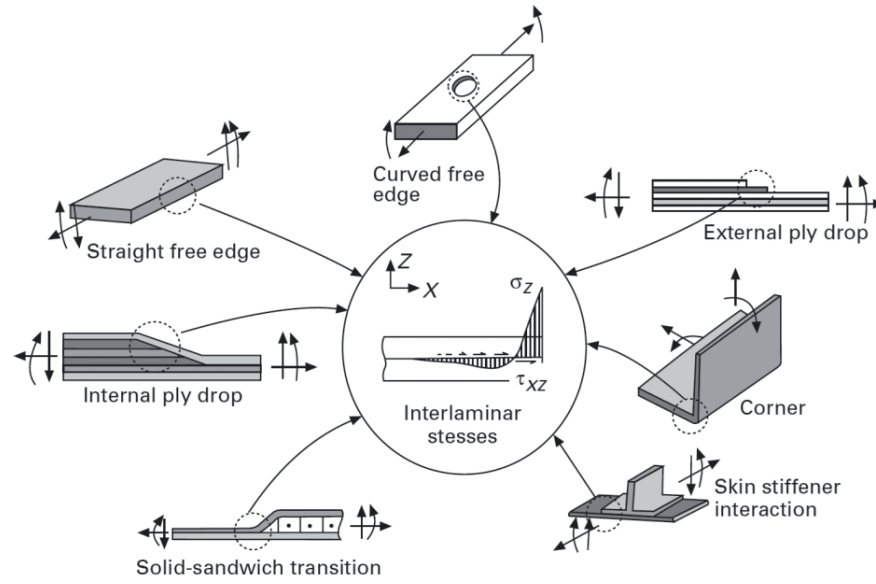


Fig. 2.6: Sources of interlaminar fracture [24].

Several parameters are shown to influence the interlaminar fracture:

- Farmand-Ashtiani [29] measured lower steady-state crack driving force in fatigue loading than in monotonic loading condition.
- The mode I steady-state fracture toughness is observed to decrease with increasing Young's modulus [30]. The role of fiber morphology is also highlighted.
- The laminate stacking sequence affects the crack growth. In particular, the unidirectional (UD) laminates do not behave similarly as angled ply laminates [31, 32, 33, 34].
- Temperature and moisture must be controlled to guarantee a good repeatability of the tests [35].
- The ERR level at steady-state propagation is reported higher in thicker specimens [36, 37].

In contrast to these parameters, the influence of the ply thickness on the interlaminar fracture ERRs at crack initiation and subsequent growths has not been reported yet in the literature.

The ASTM standard D5528-01 [38] details the testing procedure to obtain the Mode I interlaminar fracture toughness of unidirectional fiber-reinforced polymer matrix composites. It recommends the use of double cantilever beam (DCB) specimens loaded by a pair of symmetric forces applied at the end of the beams. The

crack starter is obtained by inserting a non-adhesive film at the mid-plane of the laminate during the stacking sequence. When the release film is sufficiently thin, it does not influence the crack initiation [39, 40]. Computation of the R-curve is done by monitoring the load, displacement and crack length simultaneously and applying a compliance calibration (CC) data reduction method. The use of correction factors for the large displacement and end block is suggested [38, 41]. The CC method assumes the linearity of the system in the computation of the compliance. The potential sources of non-linearity are the material non-linear deformation such as plasticity or viscosity and geometrical non-linearity associated with large displacements. If the linearity of the system is not verified, a J-integral approach can be adopted [42, 43, 44, 45].

In contrast to mode I, the testing of mode II interlaminar fracture has been standardized only recently (ASTM standard D7905-14 [46]). The main reason for the lack of standardized procedure until then is the difficulty to measure the crack length under in-plane shear loading conditions, since the crack faces remain in contact one with each other's. There are mainly four configurations for the interlaminar mode II fracture testing (Fig. 2.7): (a) End notched flexure (ENF), (b) stabilized end notched flexure (SENF), (c) end loaded split (ELS) and (d) four-point end notched flexure (4ENF) specimens [47]. The ENF test is the configuration recommended by the ASTM standard [46] and follows a simple procedure. However, it generally leads to unstable crack propagation [47, 48, 49], which prevents the study of potential R-curve behavior. To overcome this drawback, Kageyama et al. [47, 50] propose the SENF test configuration, which is stable but involve a complex control system. The ELS configuration allows for long crack length increment but suffers from variability in the clamping device [47, 51]. The 4ENF test configuration is stable and requires a simple set-up [47, 52]. As for the other test configurations, the contribution of friction must be considered and verified to be small [53]. Stutz [54] showed that while the friction between the loading pins and the specimen is of paramount importance, the friction between both crack faces has a negligible influence. It was also observed that the mode II critical ERR is almost constant with respect to crack length with no clear signs of fiber bridging. In our work, the 4ENF configuration is used, since it does not require a complex set-up and produces stable crack propagation.

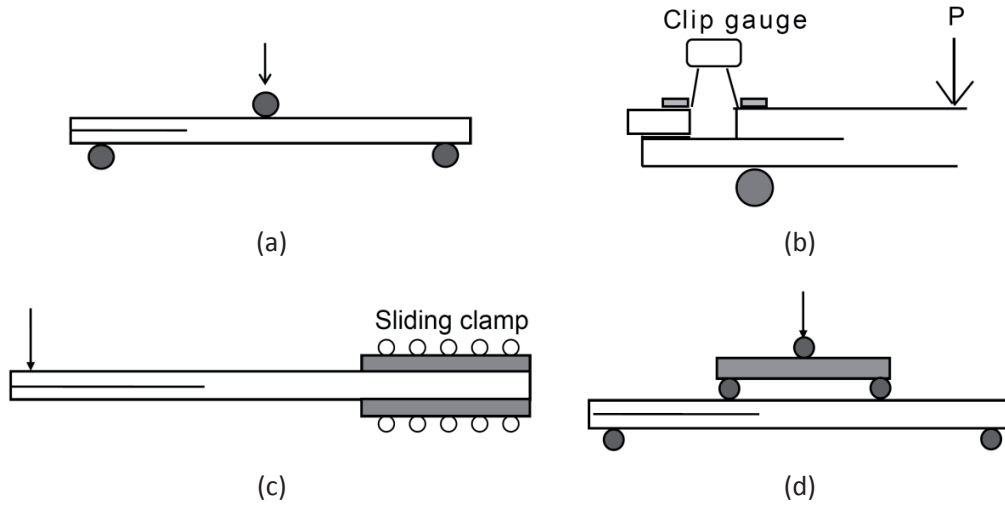


Fig. 2.7: Specimen configurations for interlaminar mode II testing [47].

2.4 Intralaminar fracture

Intralaminar fracture is often the first damage event in the failure of laminated composites. Indeed, in CP or QI laminates loaded in the in-plane direction, transverse cracks appear first in the plies oriented normal to the loading direction. These intralaminar cracks are generally followed by delamination at the interface between the adjacent plies [6, 55, 56]. Therefore, it is important to characterize both the inter- and intra-laminar fracture.

A standardized testing procedure for the mode I intralaminar fracture is still lacking. According to the ASTM definition [5], the word intralaminar refers to “events within the laminae of a laminate”. The intralaminar fracture is usually interpreted as out-of-plane intralaminar crack, but can also be interpreted as in-plane intralaminar crack [55]. In this study, out-of-plane intralaminar cracks are considered (Fig. 1.2), since they correspond to the transverse cracks observed in multidirectional laminates. Moreover, an interlaminar crack can naturally migrate within a ply because of the presence of fiber-rich regions. Such a behavior is not distinguished in delamination analysis and is still referred to as interlaminar fracture.

Due to the lack of standards, several specimen geometries can be employed. The most commonly used are the DCB [6, 55, 57, 58, 59, 60, 61, 62, 63, 64] and compact tension (CT) [63, 64, 65] specimens. In this work, DCB specimens are tested because large crack length increments can be reached and the R-curves can converge to steady-state values. Complementary tests are also carried out on CT specimens. The

crack starter is usually obtained by mechanical machining using razor blades and disc cutters [55, 58, 63, 65] or diamond wire saws [57, 59, 60, 61, 62]. In recent studies, several authors have inserted release film to create the intralaminar crack starter [6, 55, 66]. This latter procedure is difficult, since the exact position of the specimen in the plate is not necessarily known beforehand. Therefore, in the present study, the crack starter is machined with a diamond wire saw of small diameter.

As summarized by Czabaj and Ratcliffe [56], most of the studies about intralaminar fracture compare the obtained fracture toughness with the corresponding interlaminar values. However no clear trend is observed on the ratio of intra- over inter-laminar fracture toughness, even if generally the intralaminar fracture exhibits higher toughness values than interlaminar fracture. This absence of agreement can be explained by the inconsistencies among the measurement and testing procedures, in particular in the way to introduce the crack starter. Moreover, the ratios at crack initiation and steady-state propagation are not always clearly distinguished one from each other's, leading to ambiguous messages.

Size effects in intralaminar fracture have received only limited attention. The main work has been reported by Pappas et al. [59, 61, 67]. They reported increasing ERR at steady-state propagation with increasing specimen thickness. Therefore, the R-curves obtained for intralaminar fracture cannot be considered as material properties [59, 62]. In contrast to the specimen thickness effect, the influence of ply thickness on the intralaminar fracture has not been reported yet in the literature.

2.5 Fiber bridging and traction-separation relations

Intact fibers are generally observed in the wake of inter- and intra-laminar crack loaded in mode I (Fig. 2.8). This phenomenon, called fiber bridging, occurs when the crack path moves from one side to the other side of a fiber or group of fibers. In this case, the intact fibers bridge both faces of the crack. Such a behavior can happen when the fibers are not perfectly aligned with the crack plane or if micro-cracks nucleate in the vicinity of the crack tip [68]. The bridging fibers exert closing forces and prevent the crack to propagate faster. Therefore, fiber bridging is reflected by an increase in the ERR in the R-curves. The bridging phenomenon is mainly controlled by the fiber/matrix debonding and fiber failure. As long as the tensile stress in the fibers does not exceed the fiber strength, the bridging fibers are progressively peeled-off. Beyond a certain opening, all the bridging fibers are broken. At this stage, the development of new bridging fibers compensates the failure of fibers at the end of

the bridging zone. Therefore, the crack growth becomes self-similar and the R-curve reaches a steady-state value.

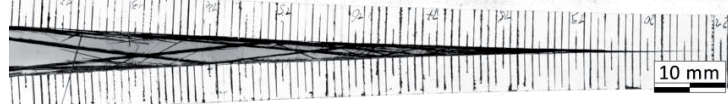


Fig. 2.8: Fiber bridging in a DCB specimen for intralaminar fracture testing.

In both the inter- and intra-laminar mode I fracture, the steady-state ERR can be several times higher than the initiation value. The fiber bridging behavior is affected by different parameters such as the fiber/matrix combination, specimen thickness [36, 37, 59], ply thickness [69, 70], orientation [29, 71] and microstructure. At a continuum scale, fiber bridging can be seen as a continuous relation between closing stresses and crack opening displacement (COD). To acquire a thorough understanding of this important toughening mechanism, it is mandatory to identify the fiber bridging closing tractions. Surface traction distributions or cohesive traction-separation relations are also required to realistically predict crack growth as a function of the aforementioned parameters.

The existing identification methods proposed in the literature are based either on inverse methods or analytical models. In a first method, used by Sørensen et al. [72], Tamuzs et al. [73] and Sorensen et al. [74] the COD at the crack starter $\bar{\delta}$ is measured during the experiments. The ERR (G or J) is then derived with respect to the COD measurements to obtain the bridging tractions: $\sigma_b(\bar{\delta}) = dG/d\bar{\delta}$. This semi-analytical method is relatively simple but might suffer from inaccuracies in the COD measurements. These imprecisions are amplified in the computation of the derivative.

Sorensen et al. [74] propose an inverse method based on local strain measurements in the vicinity of the crack tip using fiber Bragg sensors. These sensors are integrated in an optical fiber embedded in a selected specimen. This method is further developed by [75] and successfully employed to analyze the specimen thickness effects in inter- and intra-laminar fracture [36, 37, 59]. However, it is not always possible to embed an optical fiber in the laminate, for instance in woven or thin-ply composites. Therefore, this elaborate method is not always applicable.

Another inverse identification method uses cohesive element models and the load-displacement response as objective function [76]. This simple method is computationally expensive because it requires the solution of cohesive element

simulations at each of the iterations. Moreover, the crack extension is not considered in the objective function, so that the convergence to a unique solution is not necessarily ensured.

Several authors simply represent the fiber bridging behavior by linear or bilinear softening cohesive laws [63, 77, 78]. This approach accounts for the ERR at crack initiation and steady-state propagation, but does not consider the transient phase of the R-curve. However the linear and bilinear softening laws do not represent realistically the inter- and intra-laminar fracture and are not suitable for the study of scaling effects [36, 62, 79, 80].

Given the difficulties related to each of the existing identification approaches, there exists a demand for the development of an alternative method. This method should ideally fulfill the following specifications. It should be appropriate for the study of the large range of bridging intensities observed in inter- and intra-laminar fracture (typically from 0.1 to 10 MPa). Moreover, it should be based on data readily obtained from standard tests. Finally, the method should be time and cost effective so that it can be applied to numerous series of tests.

2.6 Translaminar fracture

The composite laminates are generally optimized to concentrate a maximum of fibers in the most loaded directions. In these multidirectional laminates, a through-the-thickness crack necessarily needs to break fibers to propagate. Such a failure mechanism is represented by the mode I translaminar fracture. The growth of translaminar cracks is particularly critical since it directly affects the stiffness of the structure and can eventually lead to a complete failure. However, the measurement of the translaminar fracture toughness is relatively difficult. Therefore, lots of studies only measure the ultimate strength of notched specimens such as open-hole specimens, rather than addressing specifically the fracture toughness.

Several techniques exist for measuring the translaminar fracture toughness. An ASTM standard is dedicated to the measurement of the initiation translaminar fracture toughness of laminated and pultruded polymer matrix composites materials, based on single-edge-notched specimens [81]. Another ASTM addresses the fracture toughness of metallic materials by testing CT specimens [82]. Both standards recommend the SIF approach as data reduction method. However, it has been shown by Pinho et al. [83] and Laffan et al. [84] that the correction factors developed for isotropic laminates are not accurate for orthotropic materials such as CP laminates.

Laffan et al. have reviewed the different specimen geometries and data reduction schemes for the measurement of the translaminar fracture toughness [85]. They identify six specimen configurations: (i) compact tension, (ii) extended compact tension, (iii), three / four point bending, (iv) single edge notched tension, (v) double edge notched tension and (vi) center notched tension. Only the first three configurations exhibit stable propagation and are therefore appropriate for the measurement of a complete R-curve. The compact tension configuration is the most commonly used.

With the CT configuration, several data reduction methods can be used. The first one is the computation of the critical SIF recommended by the ASTM standards [81, 82] and used by different authors [65, 86, 87] despite the inaccurate results for orthotropic materials. A simple alternate method to compute the ERR is the area method. The dissipated energy, represented by the area under the load-displacement curve, is divided by the total area of surface created during the fracture process. This calculation gives an average ERR value on the range of propagation. However, for small crack length increment the method is very sensitive to crack length measurement. Therefore, this approach is not suitable for the measurement of initiation ERR. Another data reduction method consists in calculating a contour J-integral based on digital image correlation (DIC) measurements. This approach, used by Catalanotti et al. [88] and Hou and Hong [89], does not require the measurement of the crack length. Moreover, the DIC measurements can help to identify the crack tip position for the determination of the x-axis of the R-curves.

A compliance calibration method cannot be employed for CT specimens in a straightforward manner. Indeed, the crack propagates by a succession of jumps, so that only a few points correspond to a critical state. Therefore, the compliance fitting might lead to non-unique solutions. Moreover, this method relies on a precise measurement of the crack length, which is unlikely in CT composite specimens. Therefore, a modified compliance calibration method is introduced by [90]. This approach consists in measuring the initial compliance of specimens that have crack starters machined at different lengths. The so-obtained compliance vs crack length data is fitted with a power law. Using the experimental load and displacement values, an effective crack length is then computed by inverting the fitted relation. Finally, the standard compliance calibration method is applied using the fitted compliance curve and effective crack length. The main advantage of this method is to eliminate the need of measuring the crack length. This approach is used in [84, 91] among others. More recently, the compliance vs crack length curve obtained experimentally has

been replaced by data obtained from FE simulations [92, 93, 94, 95]. However, this method has two main drawbacks: (i) it requires the linearity of the system and (ii) the compliance vs crack length curve does not account for dissipative mechanisms in the wake of the crack, such as fiber pull-out.

Since the group of Pinho is one of the main contributors about the toughness measurement in carbon/epoxy laminate, the modified compliance calibration method is probably the most widely used data reduction approach. However this method makes assumptions that are questionable. As affirmed recently by Furtado et al. [96], there is not a data reduction method which is currently established. In our work the data reduction is done by J-integral computation, since it appears to be the most reliable method.

Size effects on the translaminar toughness of CP carbon/epoxy laminates have been studied by Laffan et al. [97]. They showed that the in-plane scaling of the CT specimens does not affect the translaminar toughness. In contrast, blocking 0° plies significantly increases the toughness. In a recent study, Teixeira et al. [95] reported the same trend using thin-ply CP specimens. They attributed the size effect to smaller pull-out fibers in the thin-ply laminate when compared to thicker-ply laminates. The important influence of fiber pull-out on the fracture toughness has also been reported in [94, 98]. The ply thickness effect has not been reported yet for other lay-up such as QI laminates.

Chapter 3

Materials and methods

This chapter provides general information about the materials and methods used in this study. In particular, the manufacturing of the laminate plates and the experimental measurement tools such as fiber Bragg grating (FBG) sensors and digital image correlation (DIC) are described in this chapter. While the general test configurations and data reduction methods are also explained here, the specific details of each test are given in the corresponding chapters. The numerical approach for fiber bridging identification and cohesive elements simulations are also presented in this chapter.

3.1 Experimental procedure

3.1.1 Laminates manufacturing and specimen preparation

The material used throughout this study is a carbon-epoxy composite manufactured by NTPT, Renens. It is made of high modulus Toray M40JB carbon fibers (fiber modulus 377 GPa, ultimate strain 1.2% [99]) and an 80°C curing temperature epoxy resin called TP80EP. It is delivered in rolls of UD prepregs, meaning that the fibers are already impregnated by the uncured resin. Prepregs are commonly used in the manufacturing of composite laminates because they ensure a good repeatability, especially in terms of fiber volume fraction. The rolls of prepregs, enveloped in hermetic plastic bags, are stored in freezers in order to prevent the resin to start curing. To avoid condensation of water on the prepreg, a roll is taken out of the plastic bag only when it reaches the room temperature. This precaution is essential because moisture contamination would considerably affect the mechanical behavior of the laminate.

The same batch of fibers and resin is used throughout the whole experiment program, limiting at maximum any scattering effects due to heterogeneities in the

manufacturing process. The prepregs are made of three different carbon fiber grammages (also called fiber areal weight): $g=30, 75$ and 150 g/m^2 . These values represent the areal weight of carbon fibers per plies and approximatively correspond to a nominal cured thickness of $t=0.030, 0.075$ and 0.150 mm respectively. A small amount of 100 g/m^2 prepreg is delivered and used only in the mode II interlaminar and mode I CP translaminar testing. The selected ply thicknesses cover a range from a conventional ply thickness down to the thinnest prepreg available for this carbon/epoxy combination. The work done by Amacher et al. [3] showed that the ply thickness effect is strong on this range of ply thicknesses (Fig. 2.2). Considering ply thickness smaller than $t=0.030 \text{ mm}$ would be worthless since the full strength potential is reached and the onset of damage occurs at more than 95% of the ultimate strength.

The laminated plates are produced by stacking by hand the appropriate sequence of plies. While the inter- and intra-laminar tests require UD plates, the translaminar fracture is tested on cross-ply (CP) and quasi-isotropic (QI) laminates. The number of plies is adjusted so that the nominal thickness of the laminate is kept constant for each test configuration. For CP and QI laminates, the number of $[90^\circ/0^\circ]$ and $[45^\circ/90^\circ/-45^\circ/0^\circ]$ ply groups is adjusted to best match the specimen thickness target. The plate thicknesses are dictated by considerations related to the specific test configurations. In particular, the thickness of the plates for intralaminar fracture testing corresponds to the width of the DCB specimens. This width should not be smaller to avoid edge effects. The thickness of the plates for translaminar fracture testing is set to approximately 10 mm to limit compressive damage by buckling of the specimen ligament. Table 3.1 summarizes all the plates produced for this study, with the lay-up, grammage g , number of plies n_p , length L , width B , cured plate

thickness H and fiber volume fraction $v_f = \frac{n_p \cdot g}{H \cdot \rho_f}$, where $\rho_f = 1770 \text{ g/m}^3$ is the

carbon fiber density [99]. For the 10 mm thick plates required for intra- and translaminar tests, the plies are pre-stacked in complexes of 4 layers by an automatic plotter and delivered as complexes cut directly at the dimensions of the plates. The stack of prepregs is put under vacuum every four layers for $t=0.075, 0.100$ and 0.150 mm and every eight layers for $t=0.030 \text{ mm}$ during 10 minutes in order to remove the air trapped between the plies. This debulking procedure ensures a good compaction and a limited void content in the produced laminate.

3.1 Experimental procedure

Table 3.1: Produced laminate plates.

Denomination	Lay-up	g (g/m ²)	n_p (-)	L (mm)	B (mm)	H (mm)	v_f (-)
4ENF_100_4	[0° ₂₀ /insert/0° ₂₀]	100	40	210	210	3.90	59.1%
DCB_30_4 *	[0° ₆₅ /insert/0° ₆₅]	30	130	180	210	3.89	56.9%
DCB_75_4 *	[0° ₂₆ /insert/0° ₂₆]	75	52	180	210	3.79	58.2%
DCB_150_4	[0° ₁₃ /insert/0° ₁₃]	150	26	220	300	3.88	56.1%
DCB_30_8_s**	[0° ₁₃₂ /insert/0° ₁₃₂]	30	264	210	210	7.93	56.7%
DCB_30_8	[0° ₁₃₈ /insert/0° ₁₃₈]	30	276	210	210	8.28	56.8%
DCB_150_8_s**	[0° ₂₆ /insert/0° ₂₆]	150	52	210	210	7.89	55.2%
DCB_150_8	[0° ₂₈ /insert/0° ₂₈]	150	56	280	280	8.10	57.9%
DCB_30_2	[0° ₃₄ /insert/0° ₃₄]	30	68	210	210	2.02	57.3%
DCB_150_2	[0° ₇ /insert/0° ₇]	150	14	210	210	1.97	59.5%
INTRA_30	[0° ₃₃₆]	30	336	340	200	10.45	54.8%
INTRA_75	[0° ₁₃₅]	75	135	340	200	9.85	58.1%
INTRA_150	[0° ₆₉]	150	69	340	200	9.93	58.2%
CT_CP_30	[[90°,0°] ₈₂ ,90°] _s	30	330	300	150	9.85	57.1%
CT_CP_75	[[90°,0°] ₃₂ ,90°] _s	75	130	300	150	9.47	58.2%
CT_CP_100	[[90°,0°] ₂₄ ,90°] _s	100	98	300	150	9.53	59.3%
CT_CP_150	[[90°,0°] ₁₆ ,90°] _s	150	66	300	150	9.66	57.2%
CT_QI_30	[45°/90°/-45°/0°] _{40s}	30	320	170	300	9.82	55.5%
CT_QI_75	[45°/90°/-45°/0°] _{16s}	75	128	170	300	9.20	59.0%
CT_QI_150	[45°/90°/-45°/0°] _{8s}	150	64	170	300	9.06	59.2%

* Embedded optical fiber

** Scrapped because of the high porosity content

Once the stacking procedure is completed, the uncured laminate is placed on the hot plate of the LMAF autoclave. A 25 mm thick counter-plate ensures the flatness of the plates and the desired thickness is imposed by spacers precisely machined at the thickness target. In UD plates, two spacers constrain the laminate along the 0° edges, preventing the fibers to spread laterally. In QI plates, one spacer is in contact with one of the long side of the plate, in order to keep a direction of reference. To avoid failure of the vacuum bag when applying pressure and allowing resin flow on the

3. Materials and methods

sides of the plates, spacers are placed under the periphery of the counter-plate. The uncured laminate being thicker than the spacers, as depicted in Fig. 3.1, a good compaction is allowed, letting the excessive resin and air flowing from the laminate. The mold is then covered by a layer of breather and sealed in a vacuum bag. Two valves are plugged in order to suck the air from both sides of the plates (Fig. 3.1).

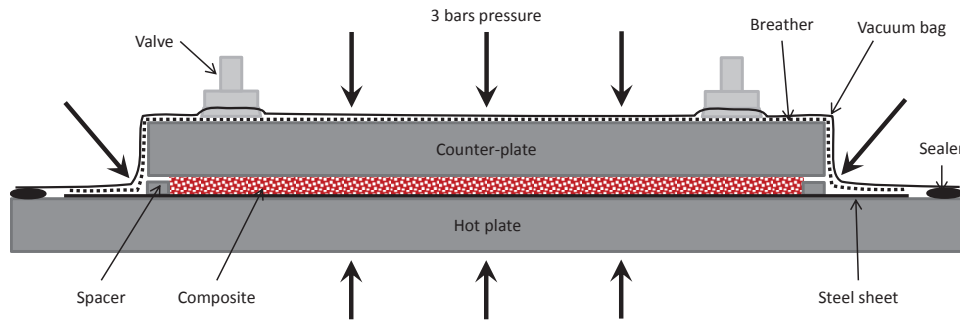


Fig. 3.1: Set-up for the curing of the composite plates.

The aforementioned procedure being completed, the autoclave is switched on and the temperature cycle is programmed, as recommended by the prepreg manufacturer. The autoclave allows a heating ramp of more than $2^{\circ}\text{C}/\text{min}$ but does not have any cooling system. As the autoclave is well isolated, the uniformity of the air temperature inside the autoclave is optimal. The curing cycle, depicted in Fig. 3.2, consists in two plateau levels reached by ramps of $1^{\circ}\text{C}/\text{min}$. The first plateau, at 58°C , kept during 2.5 hours, assures a uniform temperature through the thickness of the plate. This temperature is set just below the limit which leads to a fast increase in the curing rate. The second plateau, at 82°C , is kept during 8.5 hours to fully cure the plate. After 1 hour of the first temperature plateau, 3 bars of pressure are applied. This pressure is then kept constant until the end of the curing cycle, cooling time included.

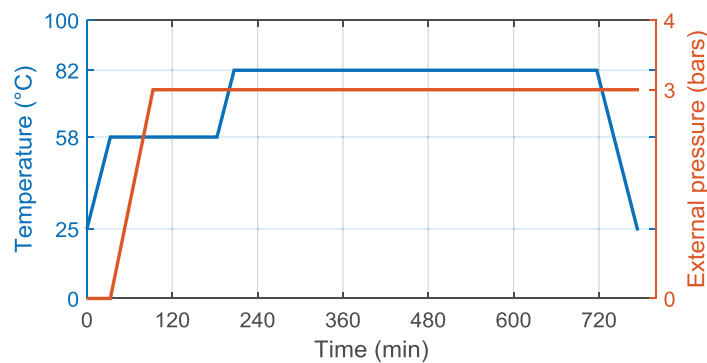


Fig. 3.2: Temperature and external pressure set points

3.1 Experimental procedure

This fabrication procedure leads to very low void content and good uniformity of thickness in the plates. Fig. 3.3 illustrates the amount of voids obtained when the plate is cured respectively with and without a good compaction during the whole curing cycle. This figure shows the importance of having an uncured stack sufficiently thick when compared to the spacers. The uncured stack is approximately 20% thicker than the cured plate in thin-ply ($t=0.030$ mm) and 10% thicker in thick-ply ($t=0.150$ mm). When this is the case, applying 3 bars of pressure is sufficient to decrease the void content to less than 1%. Ensuring a good reproducibility of the fabrication process is essential so that the experimental results can be compared with each other.

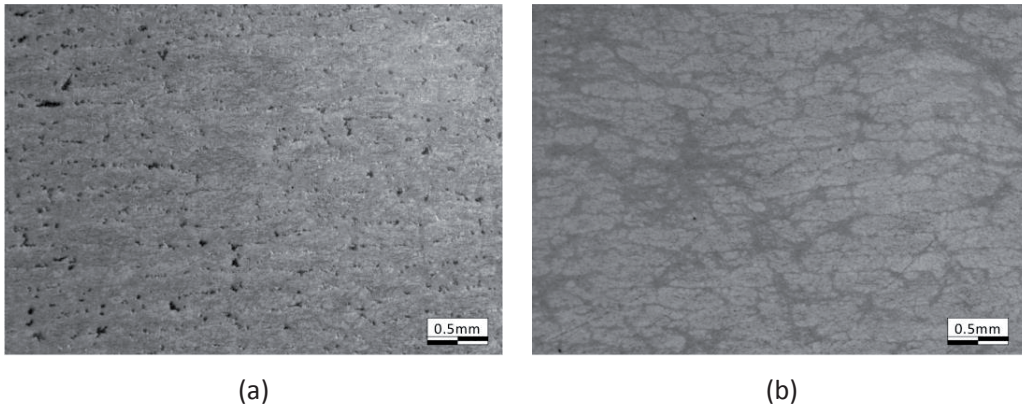


Fig. 3.3: Microstructure of an 8 mm thick plate with (a) low compaction and (b) good compaction (uncured stack sufficiently thick compared to the spacers).

The mode I inter- and intra-laminar fracture is analyzed using the double cantilever beam (DCB) configuration; the mode II interlaminar fracture is measured on four point loading end notched flexure (4ENF) specimens and the mode I translaminar fracture is assessed using the compact tension (CT) configuration (Fig. 3.4). To avoid any confusion, whatever the specimen configuration, the specimen's length l always refers to the dimension in the direction of crack propagation, the specimen's thickness h to the direction normal to the crack plane and the specimen's width b to the direction along the crack tip. While the DCB and 4ENF specimens are cut in the laminate plates with a diamond saw, the CT specimens are machined by CNC or conventional milling using diamond coated tools.

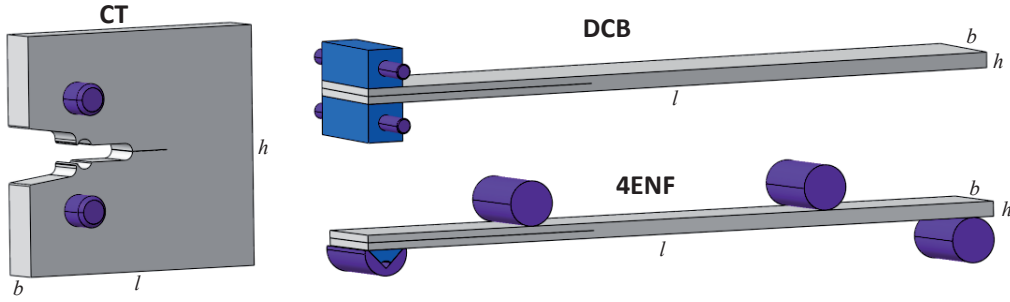


Fig. 3.4: DCB, 4ENF and CT specimen configurations.

The DCB specimens are prepared according to the ASTM standard D5528 [38]. Two steel loading blocs are glued at one end of the specimens with an epoxy two-component adhesive. Note that the crack length is measured from the center of these loading blocs. One edge side of each specimen is painted white and marked every millimeter with a 0.28 mm wide black pen to monitor the crack length. The 4ENF specimens are similarly prepared as the DCB specimens, except that only one triangular loading bloc is required (Fig. 3.4).

The compact tension specimens do not need any fixture system for the loading, as the force is applied by pins on the holes drilled in the specimens. The special shape of the notch allows the use of an extensometer in order to measure the opening displacement closed to the load application point. This measurement is very accurate since it excludes the machine, set-up and contact compliance in order to keep only the compliance of the specimen. One side of the specimens is painted white and marked every millimeter for crack length monitoring. On the other side, very small drops of white paint are sprayed to create a speckle pattern. The randomly distributed white points are required for the application of DIC.

In the interlaminar DCB specimens, the initial crack length is obtained by inserting a non-adhesive PTFE film at the mid-plane of the laminate during the stacking procedure. This film can be chosen since the curing temperature is lower than 177°C. The initial crack length in the intra- and trans-laminar specimens cannot be produced in a similar way because the exact position of the specimens in the plates is not known beforehand. For these specimens, the pre-crack is machined with a diamond wire saw of 0.13 mm in diameter. The pre-crack length varies in the range 55-65 mm in DCB specimens, 59-62.5 mm in 4ENF specimens and 20-28 mm in CT specimens. The precise crack length and specimen dimensions are detailed in the sections dedicated to the respective experimental testing programs.

3.1.2 Material properties

The M40JB/TP80EP carbon-epoxy composite belongs to the first generation of thin-ply composites. The M40JB carbon fiber has a very high modulus (377 GPa) but a relatively limited strength (4410 MPa) and a low strain at failure (1.2%) [99]. The TP80EP matrix is a low curing temperature epoxy and has limited toughness properties (measured at 215 J/m² in single edge notched bending test by NTPT). The lamina properties of the M40JB/TP80EP, which have been fully characterized by Amacher et al. [3], are shown in Table 3.2. The stiffness properties are found independent of ply thickness [3].

Table 3.2: M40JB/TP80EP lamina level properties, normalized for 55% fiber volume fraction [3].

	Unit	$t=30$ (g/m ²)	$t=100$ (g/m ²)	$t=300$ (g/m ²)
Tensile modulus @0°	GPa	222 ± 14	223 ± 12	229 ± 11
Ultimate tensile strength @0°	MPa	2250 ± 139	2350 ± 130	2360 ± 150
Tensile onset of damage @0°	MPa	1644 ± 430	2019 ± 184	1391 ± 382
Poisson's ratio ν_{12}	-	0.314 ± 0.02	0.274 ± 0.02	0.266 ± 0.02
Tensile modulus @90°	GPa	7.01 ± 0.14		
Ultimate tensile strength @90°	MPa	23 ± 4		
Compressive modulus @0°	GPa	213 ± 7.3	201 ± 5	208 ± 4.9
Ultimate compressive strength @0°	MPa	1052 ± 89	869 ± 217	848 ± 150
Compressive modulus @90°	GPa	8.04 ± 0.41		
Ultimate compressive strength @90°	MPa	117.7 ± 7		
Interlaminar shear strength	MPa	79.1 ± 2		
In-plane shear modulus	GPa	4.66 ± 0.14		
Maximum in-plane shear stress	MPa	88.26 ± 1.83		
In-plane shear stress at 0.2% offset	MPa	50.23 ± 1.00		

Using the classical laminate theory (CLT), the homogenized in-plane equivalent stiffness properties can be obtained for CP and QI laminates (Table 3.3).

Table 3.3: M40JB/TP80EP laminate level stiffness properties (in-plane equivalent moduli from CLT).

	Unit	CP	QI
$E_1 = E_2$	GPa	114.9	79.6
ν_{12}	-	0.021	0.318
G_{12}	GPa	4.778	30.2

3.1.3 Fracture tests and data reduction

3.1.3.1 Double cantilever beam (DCB) tests

The DCB specimens, used to characterize the mode I inter- and intra-laminar fracture, are tested in accordance with the ASTM standard [38]. An Instron® 5800 machine equipped with a 2 kN load cell is used to load the specimens under displacement control at a constant rate of 2.4 mm/min. The load point displacement (referred hereafter as displacement) is measured by the built-in LVDT. Both the load and displacement are recorded with a sampling rate of 1 Hz.

A high resolution CCD camera mounted on a translation stage is used to save pictures of the graduated specimen's edge around the crack tip at 1 Hz. The images are analyzed afterwards to visually detect the crack length. The time, load and displacement corresponding to each millimeter of crack increments are considered in the data reduction. Only data points corresponding to crack advance (and thus critical state) are used in the following procedure. At any time, the crack driving force or ERR is defined by Irwin as the rate of change in potential energy with crack area [23]:

$$G = -\frac{1}{b} \frac{\partial \Pi}{\partial a} \quad (3.1)$$

where Π is the potential energy of the system and a the crack length. The potential energy is the difference between the strain energy U and the work applied by the external forces F . The compliance of the system is defined as $C = \Delta/P$, where P denotes the external force applied on the system and Δ the displacement of the load introduction point. When the system behaves linearly, the total ERR is obtained by eq. (3.2), for load and displacement control, and can be split into two distinct contributions:

$$G_{I,tot} = G_{I,i} + G_{I,b} = \frac{P^2}{2b} \frac{dC}{da} \quad (3.2)$$

where $G_{I,i}$ represents the ERR at fracture initiation and $G_{I,b}$ the fracture resistance associated with fiber bridging. Note that when the crack grows, the ERR G also called crack driving force is equal to the critical ERR of the specimen G_c . In this work, since only propagation points are considered, the subscript “c” is omitted and the ERR G invariably refers to the measure of the toughness of the material.

In order to derive the compliance with respect to the crack length without amplifying the inaccuracies due to the experimental noise, the compliance vs crack length data are fitted by an analytical function which is then differentiated. The ASTM standard D5528 [38] proposes two functions:

- $C = N_1 a^{N_2}$, N_1 and N_2 being the fitting parameters. This function is referred to as compliance calibration (CC);
- $C = (a/(hN_3) + N_4)^3$, N_3 and N_4 being the fitting parameters and h the specimen's thickness. This function is referred to as modified compliance calibration (MCC).

The ASTM standard is developed for crack propagation of about 50 mm. Both the CC and MCC methods provides fairly good fitting on such a range of crack propagation. However, in case of large scale bridging, longer crack propagation is required in order to reach steady-state propagation. In this case, both the CC and MCC methods fail to accurately fit the compliance on the whole range of propagation. As an alternative, Pappas and Botsis [59] propose to split the experimental data in two sets: one for the transient data, one for the steady-state. Both sets are then fitted by two independent power laws (DCC method). However, this procedure introduces a discontinuity in the R-curve and requires knowing a priori at which crack length the steady-state is reached. Another alternative consists in building a function with three parameters in order to have an accurate fitting on the whole range of propagation.

In this study the following function is proposed: $C = N_5 (a + N_6)^{N_7}$ (CC3 method). Fig. 3.5 shows an experimental set of compliance vs crack length and the different fitting functions obtained in a $t=0.150$ mm DCB specimen for intralaminar fracture testing. Even if each fit has a R^2 value larger than 0.99, they provide results on the R-curve which are very different. In particular, the ERR at crack initiation and at steady-

state varies by up to 23% and 15% respectively (Table 3.4). In this study the CC3 method is used since it provides a continuous and high quality fitting of both the compliance curve and its slope. It has the best coefficient of determination R^2 . In particular, on the first millimeter of propagation, the fitting is better with the CC3 method when compared to the other functions. In contrast to the other methods, CC3 does not necessarily show a clear plateau. However, since it better represents the compliance curve slope, this is not considered as a drawback. In the context of this work, crack propagation is defined as steady-state when the average ERR value on at least 30 mm remains within the experimental scatter.

The compliance calibration methods are valid only if the linearity of the system is verified. In this work, the system linearity is verified on selected specimens based on the following criteria:

- The strain in the specimen does not exceed the transverse critical strain;
- The specimen's compliance obtained by simulation with and without nonlinear geometry formulation at maximal imposed displacement does not differ by more than 5%;
- The area under the unloading curves, which corresponds to the stored strain energy, does not differ from the energy obtained assuming linear-elasticity by more than 10%;
- The R-curve obtained by compliance calibration does not differ from the J-integral based R-curve by more than 10%.

Since these criteria are fulfilled, the material can be assumed to behave in a linear-elastic manner and geometrical non-linearity is also considered insignificant. An alternate method valid also in case of non-linearity consists in calculating the J-integral using eq. (3.3):

$$J_{I,tot} = J_{I,i} + J_{I,b} = \frac{P\theta}{b} \quad (3.3)$$

where θ is the relative angle between both arms of the specimen at the load application point. This angle is measured by DIC, as detailed in section 3.1.5.1. When the system behaves linearly, the ERR values G and J are supposed to be equal. This affirmation is verified for different cases and is further discussed in section 5.1.2.

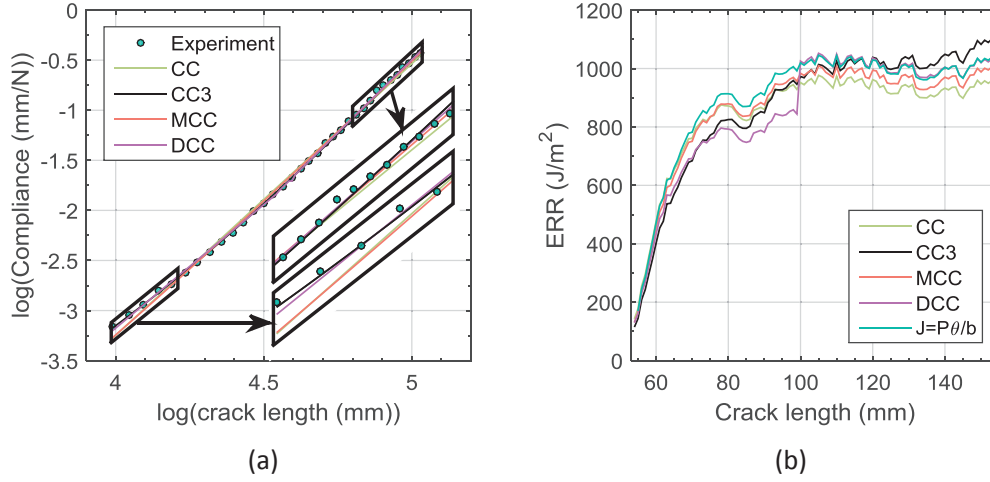


Fig. 3.5: (a) Compliance fitting with different functions; (b) Corresponding R-curves.

Table 3.4: Compliance fitting and corresponding ERR values

Method	Fitting R^2 (-)	$G_{I,i}$ (J/m ²)	$G_{I,ss}$ (J/m ²)
CC	0.9976	177.8	952.9
CC3	0.9997	144.2	1096.4
MCC	0.9990	164.1	996.0
DCC	0.9981	161.7	1026.4
J	-	169.8	1030.6

The R-curve represents the critical strain ERR as a function of the crack length. In practice, the experimental ERR is computed for each millimeter of crack propagation. However, in case of small crack jumps during the test, the points which do not correspond to critical load are removed from the data reduction. Therefore every points considered in the R-curve are locally critical. In order to avoid confusion with the ERR at onset of propagation $G_{I,i}$ often denoted G_{Ic} when it is a material constant (which is not the case when the material follows an R-curve), the word critical is omitted and the critical strain energy released rate is simply referred as ERR.

3.1.3.2 Four points end notched flexure (4ENF) tests

The 4ENF configuration is selected for the characterization of mode II interlaminar fracture, since it leads to stable crack propagation without requiring a complex test

3. Materials and methods

set-up. The specimens are tested on a Walter & Bai machine equipped with a 10 kN load cell, under displacement control at a constant rate of 0.6 mm/min. The displacement is measured by the built-in LVDT. Both the load and displacement are recorded with a sampling rate of 10 Hz. Similarly as for the DCB specimens, the crack length is monitored by observing the images recorded by a high resolution CCD camera at 1 Hz. The time, load and displacement corresponding to each millimeter of crack increments are considered in the data reduction.

As reported by Stutz [54], the friction between the loading pins and the specimens has a significant effect on the test results. Therefore, the fixture used to apply the four points bending is equipped with roller bearings. This way, the effects of friction due to the fixture are limited. An illustration of the fixture is displayed in Fig. 3.6. The effects of friction are quantified by loading-unloading cycles. The dissipated energy in one loading-unloading cycle represents less than 10% of the energy dissipated to propagate the crack on 70 mm. Geometrical non-linear effects are also verified to be negligible by FE simulations with and without non-linear formulation. The lower span is chosen to use the complete length of the specimens. The upper span is set to half of the lower span. With this configuration, the initial crack is at least 10 mm away from the upper loading pin. This way, possible issues related to the local compression applied by the loading pin are avoided.

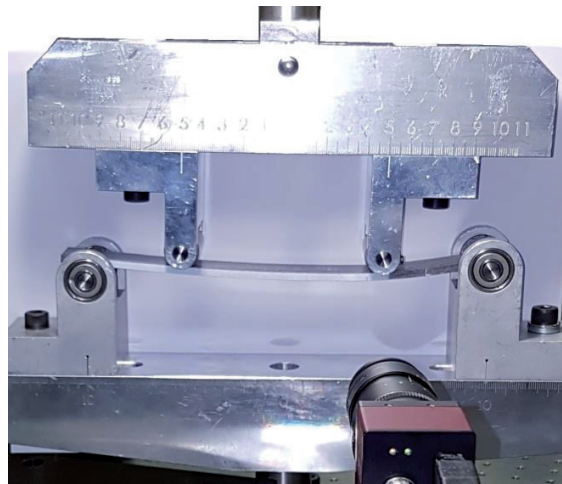


Fig. 3.6: Fixture for mode II experimental testing.

The compliance calibration method is used as data reduction procedure. The fitting function selected for this test configuration is an affine relation $C = N_8 a + N_9$. Indeed, by beam theory calculations, it can be shown that if the crack is between both central loading points, the compliance is equal to [100]:

$$C = \frac{\Delta_1 + \Delta_2}{2P} = \frac{d^2}{E_1 b h^3} (6l - 10d + 9a) + \frac{6d}{5G_{13} b h} \quad (3.4)$$

where, Δ_1 , Δ_2 , P , d and l are defined as depicted on Fig. 3.7, E_1 is the longitudinal Young's modulus, G_{13} the shear modulus, b and h the specimen's width and thickness. As a consequence, the derivative of the compliance with respect to the crack length is a constant and the ERR is expected to be constant along the crack propagation.

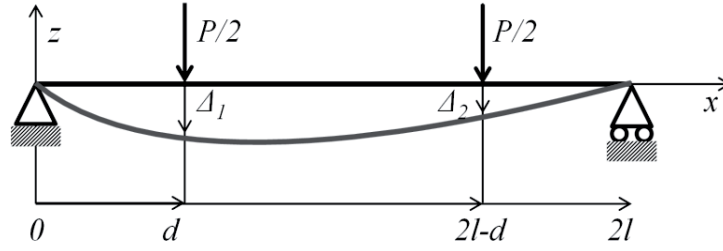


Fig. 3.7: Schematic of a 4ENF specimen (adapted from [100]).

3.1.3.3 Compact tension (CT) tests

The compact tension specimens, mainly used to characterize the mode I translaminal fracture, but also for few intralaminar specimens are tested on a MTS hydraulic machine equipped with a 100 kN load cell. The specimens are loaded under displacement control at 0.5 mm/min for the translaminal specimens and at 0.2 mm/min for the intralaminar specimens in order to limit the crack propagation speed at maximum 1 mm/s.

The data reduction in CT specimens for translaminal fracture is more complex than in DCB and 4ENF tests since the hypotheses required to apply compliance calibration method are not necessarily satisfied. In the present study, the linearity of the system is not verified and the low amount of crack propagation points leads to non-unicity when fitting the compliance data. In the literature a modified compliance calibration method (MCC2) is widely used [94, 95]. In this method, which is not the same as the MMC method suggested in the delamination ASTM standard D5528 [38], the compliance vs crack length curve is obtained by FE models with different notch lengths and then fitted by a modified power law $C = (M_1 a + M_2)^{M_3}$. Based on this fitted curve and the experimental elastic compliance, an effective crack length is

computed: $a_{eff} = (C^{1/M_3} - M_2) / M_1$. For the load that propagates the crack P_c , the fracture toughness is finally obtained as:

$$G = \frac{P_c^2}{2b} \frac{dC}{da} \quad (3.5)$$

where b is the width of the specimen. Even if this method is widely used and easy to implement, the accuracy of the results is questionable. Indeed, the FE models employed to obtain the compliance vs crack length curve do not take into account any dissipative mechanisms such as fiber pull-out or fiber bridging, which are nevertheless deemed to be responsible for size effects. Moreover, the effective crack length does not have any physical meaning and is not reliable if the system behaves in a non-linear manner.

When analyzing CT tests of composite laminates, it is usually very difficult to define clearly a unique crack length. Indeed, the crack front might not be smooth, since the critical ERR is much larger in the 0° plies than in the 90° ones. The effective crack length as defined in [95] is found not very reliable since it directly depends on the linearity of the system, which is usually not verified on the experimental load-displacement curves. The measurement of the crack length by optical inspection of the specimen surface is not reliable either, since it is affected by the orientation of the ply on the surface. In particular in the QI isotropic with a 45° ply on the surface, the apparent crack does not remain on a horizontal plane. Moreover, localized delamination of the outer plies might also affect the visual crack length.

Since the crack length definition and measurement cannot be defined objectively and precisely in the CT specimens, it is necessary to compute the fracture toughness with a method independent from the crack length. Such a measurement can however be achieved by computing the contour J-integral approach based on the displacement fields measured by DIC [88]. In this case, the crack length is only used to define the abscissa axis of the R-curve, but is not used in the J-integral computation. The contour J-integral is computed with eq. (3.6):

$$J = \int_{\Gamma} w \, dx_2 - \int_{\Gamma} \sigma_{ij} n_j \frac{\partial u_i}{\partial x_1} \, ds, \quad i, j = 1, 2 \quad (3.6)$$

where w is the strain energy density, σ_{ij} the stress components, n_j the normal vector components, u_i the displacement components, and ds the differential along the contour Γ .

The contour is chosen to pass near the edges of the specimen, as depicted in Fig. 3.8 (a), because material linearity can be assumed when staying far from the crack singularity. Moreover, some terms of the integral can be neglected because:

- dx_2 is zero on the segments BC and DE
- σ_{22} is assumed to be zero on the segments BC and DE (normal stress at the free edge)
- σ_{11} is assumed to be zero on the segment CD (normal stress at the free edge)

In practice, the segments BC, CD and DE cannot be selected perfectly at the specimen edge because of the limitations of DIC measurements, but remain sufficiently close to the edges (~ 1.5 mm) so that the normal stress can be assumed to be zero.

To obtain the stress and strain tensors from the experimental specimens, a DIC technique is applied on the images showing the speckle pattern painted on the specimens (see section 3.1.5.2). Using the commercial software Vic2D, the horizontal and vertical displacement fields are extracted for the whole surface of the specimen (see section 3.1.5.2 for the DIC parameters). The displacement fields are split in three zones as depicted in Fig. 3.8 (b) in order to exclude the crack singularity. On each zone, the displacements are fitted by the cubic smoothing spline function of Matlab® with a smoothing parameter set at 0.1. Such a low value leads to a relatively strong smoothing. While filtering the measurement noise, it succeeds in capturing the displacement field which is known to be smooth (no singularity). The fitted fields can then be differentiated to obtain the strain data required for the strain energy density term and the derivatives $\partial u_i / \partial x_j$. Extracting the whole displacement fields rather than only the values on the segments allows for a good smoothing and a reduction of the noise level by averaging.

Finally, assuming an orthotropic plane stress linear behavior (3.7), the stress tensor can be computed based on the strain tensor using eq. (3.8) and the strain energy density using eq. (3.9).

$$\mathbf{C}^* = \frac{1}{1 - \nu_{12}\nu_{21}} \begin{pmatrix} E_1 & \nu_{21}E_1 & 0 \\ \nu_{12}E_2 & E_2 & 0 \\ 0 & 0 & G_{12}(1 - \nu_{12}\nu_{21}) \end{pmatrix} \quad (3.7)$$

$$\begin{pmatrix} \sigma_{11} \\ \sigma_{22} \\ \sigma_{12} \end{pmatrix} = \mathbf{C}^* \begin{pmatrix} \varepsilon_{11} \\ \varepsilon_{22} \\ 2\varepsilon_{12} \end{pmatrix} \quad (3.8)$$

$$w = (\varepsilon_{11} \quad \varepsilon_{22} \quad 2\varepsilon_{12}) \mathbf{C}^* \begin{pmatrix} \varepsilon_{11} \\ \varepsilon_{22} \\ 2\varepsilon_{12} \end{pmatrix} \quad (3.9)$$

The J-integral is computed by trapezoidal numerical integration on each of the segments depicted in Fig. 3.8 (a) using Matlab®.

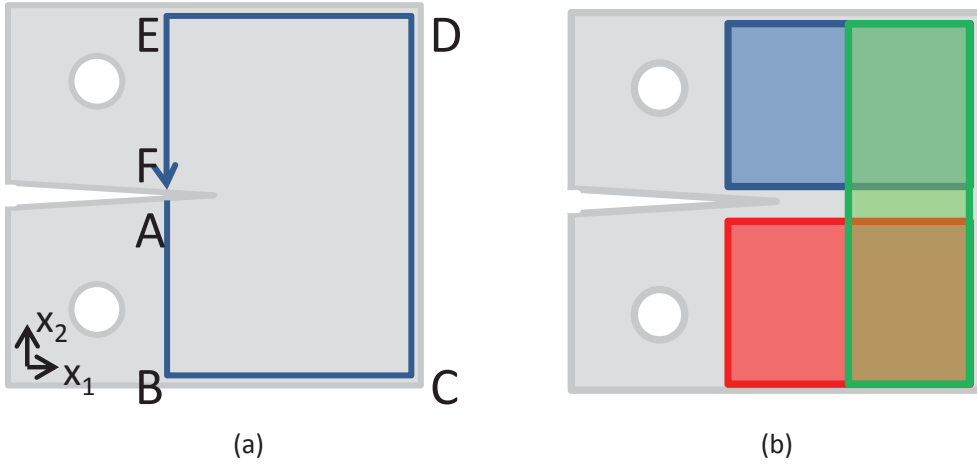


Fig. 3.8: (a) Contour selected for the J-integral; (b) Three zones selected for the displacements fields fitting.

The data reduction for the CT specimens used to measure the intralaminar fracture is however done by compliance calibration method. Indeed, since the load levels reached in intralaminar fracture are much lower than in translaminar fracture, the linearity of the system is verified in practice. Moreover, in this case, the crack propagates smoothly, so that a sufficiently large amount of critical points can be employed for the fitting of the compliance. The measurement of the crack length is done optically. The following parametric function is used to fit the compliance vs crack length data: $C = (M_1 a + M_2)^{M_3}$ [95].

3.1.4 Strain measurements by fiber Bragg grating (FBG) sensors

Some selected DCB specimens are equipped with multiplexed optical fiber Bragg grating sensors in order to measure axial strain. These measurements can be used in a semi-inverse bridging traction identification process (see section 3.3.1.1).

3.1 Experimental procedure

The optical fibers, which are 0.125 mm in diameter, are very brittle and must be handle with extreme caution. The optical fiber can be embedded in the laminate during the stacking process [74, 37, 75, 101]. However, inserting a 0.125 mm fiber in thin-ply ($t=0.030$ mm) composite might be difficult. In such a case, the optical fiber can be glued on the top surface of the specimen with a liquid cyanoacrylate Locktite® 401 [59]. In both configurations, the polymer coating around the optical fiber is removed with sulfuric acid in order to obtain an optimal strain transfer from the specimen to the FBG sensors.

On the optical fibers are inscribed ten wavelength-multiplexed FBG sensors equally spaced by approximately 3 mm, center to center. Each sensor has a gauge length of 1 mm, a reflectivity higher than 50% and a bandwidth of 1.5 nm. At rest, the Bragg wavelengths $\lambda_{B0,i}$ range from 1520 to 1565 nm, by steps of 5 nm. The exact position of each sensor can be obtained by optical low coherence reflectometry (OLCR) technique [102], with a resolution of 0.025 mm. During the test, the response of the FBGs is monitored at 50 Hz with a Micron Optics SM130 sensing interrogator. At constant temperature, the shifts of the reflection Bragg peaks $\Delta\lambda_{B,i}$ are related to the axial strain at each sensor $\varepsilon_{z,i}$, which is the dominant strain component, by:

$$\frac{\Delta\lambda_{B,i}}{\lambda_{B0,i}} = (1 - p_e) \varepsilon_{z,i}, \quad i=1, \dots, 10 \quad (3.10)$$

where $p_e=0.2148$ is the opto-mechanical coefficient [75] (Fig. 3.9)

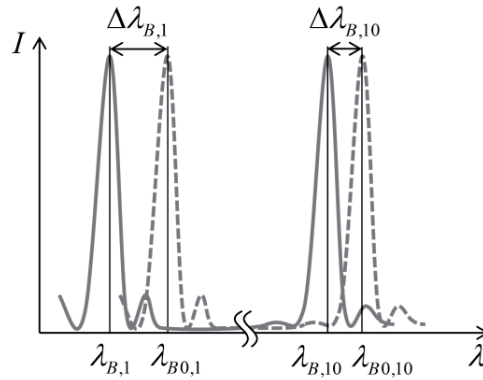


Fig. 3.9: Shift of the Bragg reflection peaks under compressive strain.

3.1.5 Digital image correlation (DIC) measurements

Digital image correlation (DIC) is an optical procedure which tracks the displacement of subsets on successive images. It can be used to reconstruct displacement fields or, after smoothing and differentiation, strain fields. In this work, DIC techniques are used to:

- Measure relative angle of the arms in DCB specimens;
- Extract the displacement field on the surface of CT specimens.

3.1.5.1 Angle measurement

DIC is used to monitor the position of four targets positioned on aluminum profile glued on the loading blocs of the DCB specimens (Fig. 3.10 (a)). The targets are invariants in rotation, so that the accuracy of the displacement measurement is optimized. The image acquisition is performed using a 1.3M pixel CCD camera equipped with a 25 mm focal lens. As 2D DIC is used, the alignment of the camera axis is checked to be perpendicular to the target plane. The DIC is applied using an in-house DIC Matlab® code developed by Dr Joël Cugnoni, using a single subset per target. Knowing the positions of the four targets, the relative angle can be easily calculated. Since the accuracy of the displacement measurements is approximately $0.5 \text{ pixels} \approx 0.042 \text{ mm}$ and the distance between the targets is 90 mm, the accuracy on the angle measurement is approximately $5 \cdot 10^{-4} \text{ rad}$.

3.1.5.2 Displacement field measurement

DIC is also used to extract the horizontal and vertical displacement fields on the surface of CT specimens. These displacement fields are then processed to compute the strains and derivative required in the J-integral computations (see section 3.1.3.3).

The images are acquired using a 1.3M pixel CCD camera equipped with a 25 mm focal lens. Out-of-plane displacements are assumed to be absent in these tests so that 2D DIC can be applied. The camera axis is checked to be aligned perpendicularly to the specimen plane. The DIC procedure is applied using the commercial software Vic2D. The images of the speckle pattern are imported in the software and the calibration is done by indicating a known distance on the reference image. A relatively large subset size of 25 pixels ($\approx 1.4 \text{ mm}$) is used, in order to limit the noise level (Fig. 3.10 (b)). The expected accuracy is about 0.1 pixel ($\approx 0.005 \text{ mm}$). The step between each subset is set to 5 pixels, leading to a resolution of approximately 0.3 mm. To

optimize the computing time, Vic2D uses the displacement of a subset as an initial guess of the displacements of the neighboring subsets. This technique works well for smooth and continuous displacement fields, but often leads to decorrelation in the presence of a singularity, such as a crack. To neutralize this effect, two zones are defined, one on each side of the expected crack path, so that the correlation works on each pixel in at least one of the two zones (Fig. 3.10 (b)). The horizontal and vertical displacement fields are exported in csv files for the selected images corresponding to a critical loading.

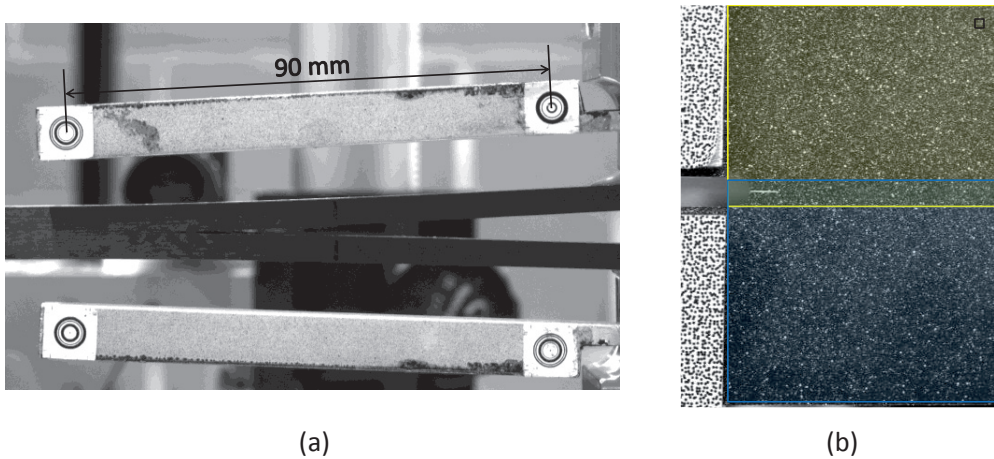


Fig. 3.10: (a) Targets for angle measurement in DCB specimens; (b) Speckle pattern, local window's size (in black) and both zones defined for DIC (yellow and blue).

3.2 Mechanistic investigations

Mechanistic investigations are carried out to analyze the reasons explaining the ply thickness effects in inter-, intra- and trans-laminar fracture. For the DCB configuration, the main toughening mechanism is fiber bridging, so that the investigations focus on the characterization of the bridging ligaments in the wake of the crack. In the CT specimens, fiber pull-out is deemed to be responsible for the size effect. Therefore, for this configuration, the crack surface is analyzed in details.

3.2.1 Fiber bridging characterization

The fiber bridging characterization in DCB specimens is done by preparing and observing successive transverse sections. Selected specimens of each ply thickness are kept open at the end of the fracture tests and embedded in polishing resin, so that the bridging fibers are kept intact and in place. Using a diamond wire saw, the

specimen is then cut in 2.5 mm slices, from the crack tip to the end of the bridging zone, as depicted in Fig. 3.11. After an adequate polishing, images of the sections are taken at 10x magnification. The heterogeneity of the microstructure of the bulk composite can be assessed by computing the coarseness measure, which is defined as the standard deviation of the local fiber volume fraction divided by the mean value (eq. (3.11)):

$$c = \frac{\text{std}(v_{f,local})}{\text{mean}(v_{f,local})} \quad (3.11)$$

where $v_{f,local}$ is the local fiber volume fraction computed based on square windows whose linear size varies from 3 to 10 fiber diameters. The coarseness represents thus a measure of the heterogeneity of the microstructure for a characteristic observation length. The local windows can be selected either randomly or on preferential directions to compute directional coarsenesses. This operation is repeated on at least 10 different sections of size 1.1 x 0.8 mm, excluding the cracked region.

The crack profile and the bridging fibers can be isolated thanks to a semi-automatic thresholding carried out in Adobe Photoshop®. Dividing the overall fiber area by the area of a single fiber, the number of bridging fibers can be evaluated. Moreover, analyzing the connected fiber regions, statistics about the bridging bundles can be extracted, such as the dimensions, major and minor axis of the equivalent second moment of inertia ellipse, and aspect ratio.

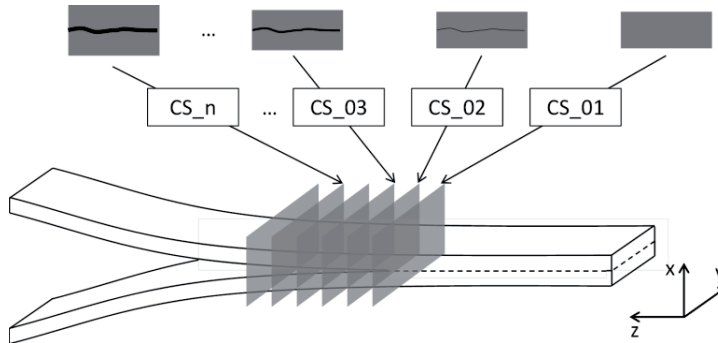


Fig. 3.11: Schematic of the DCB specimen and transverse sections.

3.2.2 Fiber pull-out characterization

Fracture surfaces of the CP CT specimens for translaminar fracture testing exhibit alternately flat areas corresponding to the 90° plies and rough profiles in the 0° plies.

Indeed, the 0° fibers fail at different heights around the crack plane and are subsequently pulled-out. The amount and height of these pull-outs appear to be influenced by the ply thickness, which could potentially explain differences in fracture toughness. Therefore, it is important to characterize the fiber pull-outs in the 0° plies of the CP CT specimens.

The fracture surface is firstly observed with a VHX-5000 Keyence optical microscope. The shape of the pull-outs can be analyzed quantitatively. Then, thanks to a depth from defocus method, the software associated with the microscope builds an accurate 3D image. Using the stitching function, the topography of the surface can be obtained for the whole fractured surface. The surface profiles along the crack propagation direction are extracted for the 0° plies using the exporting toolbox of the microscope. These profiles can then be processed to analyze the dimensions of the pull-out fibers and eventually highlight differences between the specimens of different ply thicknesses.

3.3 Numerical procedure

The final objective of the numerical modeling performed in this work is to simulate the inter-, intra- and trans-laminar fracture of the laminate as a function of the ply thickness. To reach this objective FE models are implemented to:

- Identify the traction-separation relations associated with fiber bridging in the DCB specimens;
- Implement these traction-separation relations in cohesive simulations and validate the obtained relations;
- Build and verify traction-separation relations associated with fiber failure and pull-out in CT specimens.

For each of the FE models, mesh convergence is verified.

3.3.1 Identification of bridging tractions in DCB specimens

Among other methods, the bridging tractions in the DCB specimens can be obtained by an inverse identification procedure based on strain data and developed at the LMAF-EPFL [36, 37, 59, 74, 75]. However, this procedure is very elaborate and not always applicable, since it requires the embedding of an optical fiber in the laminate and suffers from a lack of accuracy in case of low fiber bridging intensity. Therefore, an alternative identification method, based on the experimental R-curves

is developed and applied on each series of tests. The proposed procedure is validated by comparison with the existing strain-based method on selected specimens. Afterwards, the cohesive relation is obtained by appending the identified traction-separation relation representing fiber bridging to a standard linear stiffness degradation relation corresponding to the matrix cracking (See section 3.3.2).

3.3.1.1 Strain based identification

The strain based identification is an inverse method based on the identification of the strain profile close to the crack tip by iterative FE modeling. The strain profile is reconstructed from the FBG sensors data for a given crack length in the steady-state domain of the R-curve. Assuming self-similarity, the strain data are taken on plus / minus 1.5 mm of crack propagation around the selected crack length, in order to obtain a quasi-continuous profile similar as the one shown in Fig. 3.12. The FE model is a 2D plane strain model taking advantage of the symmetry on the fracture plane (Fig. 3.13). It consists in quadrilateral quadratic reduced integration elements (Abaqus CPE8R) of approximately 0.2 mm of linear size. The displacement equal to the corresponding experimental opening is applied on the loading pins and the fiber bridging is represented by a parametric surface traction distribution $\sigma(z)$:

$$\sigma(z) = e^{-\gamma z} \sigma_{\max} \left(1 - \frac{z}{z_{\max}} \right), 0 \leq z \leq z_{\max} \quad (3.12)$$

where σ_{\max} is the maximum stress in the bridging zone, z_{\max} the length of the fully developed bridging zone and γ an exponential parameter accounting for the non-linear decay of tractions.

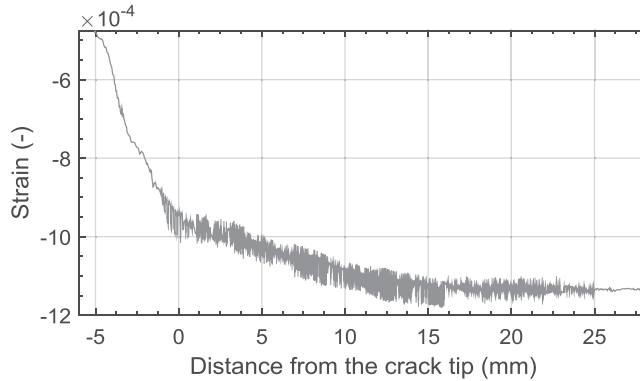


Fig. 3.12: Strain profile close to the crack tip in a representative $t=0.150$ mm DCB specimen for interlaminar fracture testing.

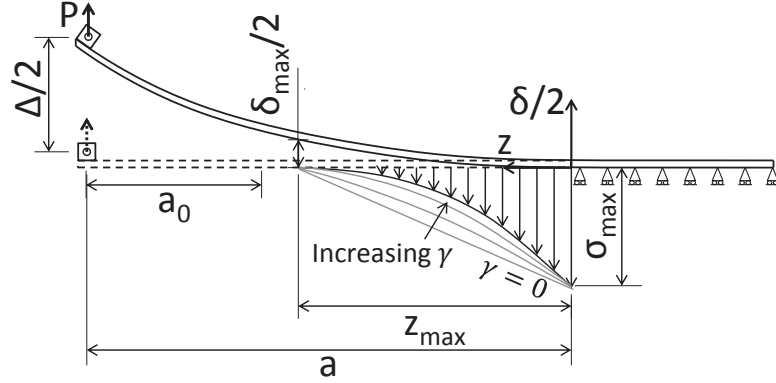


Fig. 3.13: Schematic representation of the model used in the static FE simulations.

The identification procedure consists in a residual error minimization of the objective function which is defined as the relative error between the experimental strain profile and the numerical one:

$$erf = \left\| \frac{\varepsilon_{FE} - \varepsilon_{exp}}{\bar{\varepsilon}_{exp}} \right\| \quad (3.13)$$

where ε_{FE} and ε_{exp} denote discrete strain vectors obtained from FE model and experimental data respectively. $\bar{\varepsilon}_{exp}$ is the mean value of the experimental strain vector. The minimization procedure is implemented in Matlab® using nonlinear least-squares fitting ('lsqnonlin' function) where σ_{max} , z_{max} and γ are the parameters to optimize. When the optical fiber is glued on the surface of the specimen, rather than being embedded, the strain transfer percentage and longitudinal position are not well determined. In such a case, a parameter accounting for a horizontal shift (maximum ± 2 mm) and a parameter representing the strain transfer coefficient are added in the optimization scheme.

Once the error minimization procedure has converged to an optimal solution, the identified profile must be verified by an independent set of data, such as the ERR or the reaction force. The normal COD distribution $\delta(z)$ is then extracted from the FE model and combined with the distribution $\sigma(z)$ in order to obtain the traction-separation relation $\sigma(\delta)$.

3.3.1.2 R-curve based identification

To overcome the difficulties faced with the strain based identification procedure, an efficient identification method based on the R-curve is proposed in this work [80]. The R-curve is a rich set of information, since it reflects both the global load-displacement response and the crack length. The R-curve is usually determined by DCB tests and does not require elaborate and expensive measurement tools.

In this method, the traction-separation relation $\hat{\sigma}_b(\delta)$ is assumed to follow the parametric form (3.14), which is a linear decay with respect to $\sqrt{\delta}$ from the maximum traction σ_{\max} at the crack tip to zero at the critical COD $\delta_{\max} = \delta(z)|_{z=z_{\max}}$, multiplied by a decreasing exponential term parametrized by $\hat{\gamma}$.

$$\hat{\sigma}_b(\delta) = e^{-\hat{\gamma}\sqrt{\delta}} \sigma_{\max} \left(1 - \sqrt{\frac{\delta}{\delta_{\max}}} \right), 0 \leq \delta \leq \delta_{\max} \quad (3.14)$$

Since in DCB specimens the COD profile approximately follows $\delta \propto z^2$, this function corresponds to eq. (3.12) expressed directly in terms of COD, instead of distance from the crack tip. This parametrization has been chosen so that the R-curve based identification results can be compared with the strain-based identification results. However, other nonlinear decreasing parametric functions could have been chosen.

The total ERR $G_{I,tot}$ including the effects of bridging tractions $\hat{\sigma}_b(\delta)$ can be computed with equation (3.15), where $\bar{\delta}$ is the COD at the crack starter before reaching steady-state propagation and the critical COD after having reached the steady-state (eq. (3.16)) [72, 74, 103].

$$G_{I,tot}(a, \bar{\delta}, \sigma_{\max}, \hat{\gamma}, \delta_{\max}) = G_{I,i} + \int_0^{\bar{\delta}(a)} \hat{\sigma}_b(\delta, \sigma_{\max}, \hat{\gamma}, \delta_{\max}) d\delta \quad (3.15)$$

$$\bar{\delta}(a, \sigma_{\max}, \hat{\gamma}, \delta_{\max}) = \begin{cases} \delta(z, \sigma_{\max}, \hat{\gamma}, \delta_{\max})|_{z=a-a_0} & , 0 \leq a-a_0 \leq z_{\max} \\ \delta(z, \sigma_{\max}, \hat{\gamma}, \delta_{\max})|_{z=z_{\max}} & , z_{\max} \leq a-a_0 \end{cases} \quad (3.16)$$

The principle of the method is to match the ERR $G_{I,tot}$ (eq. (3.15)) with the experimental R-curve $R(a-a_0)$ at two selected points, one in the rising part $a = a_1$ and another in the steady-state propagation phase $a = a_{ss}$ (Fig. 3.14).

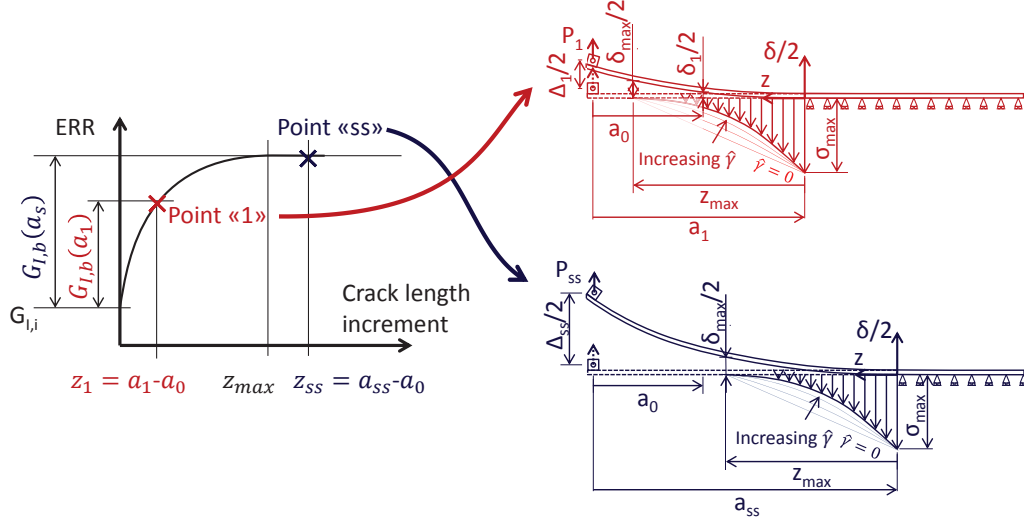


Fig. 3.14: Schematic of the R-curve based fiber bridging identification method.

To obtain this match, firstly the length of the fully developed bridging zone z_{\max} is evaluated from the R-curve as the crack length increment at which the steady-state is reached (plateau level within the experimental scatter). Secondly, $\bar{\delta}$ is extracted from two 2D plane strain FE models corresponding respectively to $a = a_1$ and $a = a_{ss}$, and accounting for the current (initial) estimate of the bridging tractions $\hat{\sigma}_b(\delta)$. These bridging tractions are modeled as a spatial traction distribution $\sigma_b(z)$ obtained by combining the traction-separation profile $\hat{\sigma}_b(\delta)$ and the current estimate of the COD profile $\delta(z)$. Consequently, the identification procedure consists in solving the nonlinear system of equations (3.17) and updating the FE models with the new estimate of the bridging tractions $\hat{\sigma}_b(\delta)$ (Fig. 3.15). The iterative process continues until the COD profile converge, leading to a convergence of the identification parameters σ_{\max} , δ_{\max} and $\hat{\gamma}$. Since this method requires only two FE solutions per iteration and usually converges in less than 7 iterations, it is about 100 times faster than a direct optimization of a nonlinear cohesive FE simulation.

$$\begin{cases} \delta_1 = \bar{\delta}(a_1, \sigma_{\max}, \hat{\gamma}, \delta_{\max}) & (a) \\ \delta_{\max} = \bar{\delta}(a_{ss}, \sigma_{\max}, \hat{\gamma}, \delta_{\max}) & (b) \\ G_{I,tot}(a_1, \delta_1, \sigma_{\max}, \hat{\gamma}, \delta_{\max}) = R(a_1 - a_0) & (c) \\ G_{I,tot}(a_{ss}, \delta_{\max}, \sigma_{\max}, \hat{\gamma}, \delta_{\max}) = R(a_{ss} - a_0) & (d) \end{cases} \quad (3.17)$$

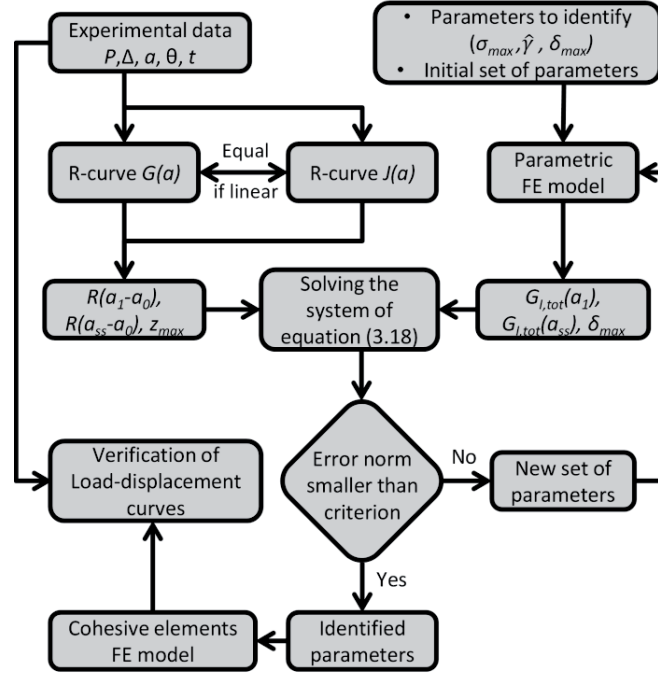


Fig. 3.15: Flowchart of the R-curve based fiber bridging identification method.

The proposed R-curve based method is validated by comparison with the existing strain based identification method on three carbon-epoxy systems having different fiber bridging intensities:

- Interlaminar fracture of a DCB specimen ($t=0.150$ mm, $h=8$ mm) made of M40JB/TP80EP (Fig. 3.16);
- Interlaminar fracture of DCB specimens made of T700/SE70 ($t=0.200$ mm, $h=4, 8, 10$ mm) [36, 80];
- Intralaminar fracture of a DCB specimen ($t=0.150$ mm, $h=6$ mm) made of M40JB/TP80EP (See section 5.3.1).

In each case, the traction-separation relations identified with both methods are in good agreement with each other, as illustrated for the first case in Fig. 3.16 (a). The strain profile obtained with the FBG sensors can be considered as a set of data independent of the data used as input of the R-curve based identification scheme and thus can be used to verify the predictions of the latter. Since the numerical strain profiles are in good agreement with the experimental ones (Fig. 3.16 (c)), it further validates the obtained traction-separation relations. Moreover, the load-displacement responses are very well predicted, in particular in the peak load regions, where fiber bridging is not yet fully developed (Fig. 3.16 (b)). The good agreement of

3.3 Numerical procedure

the global response is somehow expected since the identification process ensures the energetic balance for at least two points of the R-curve. Moreover, the crack advance is also well predicted, leading to the good match in Fig. 3.16 (d).

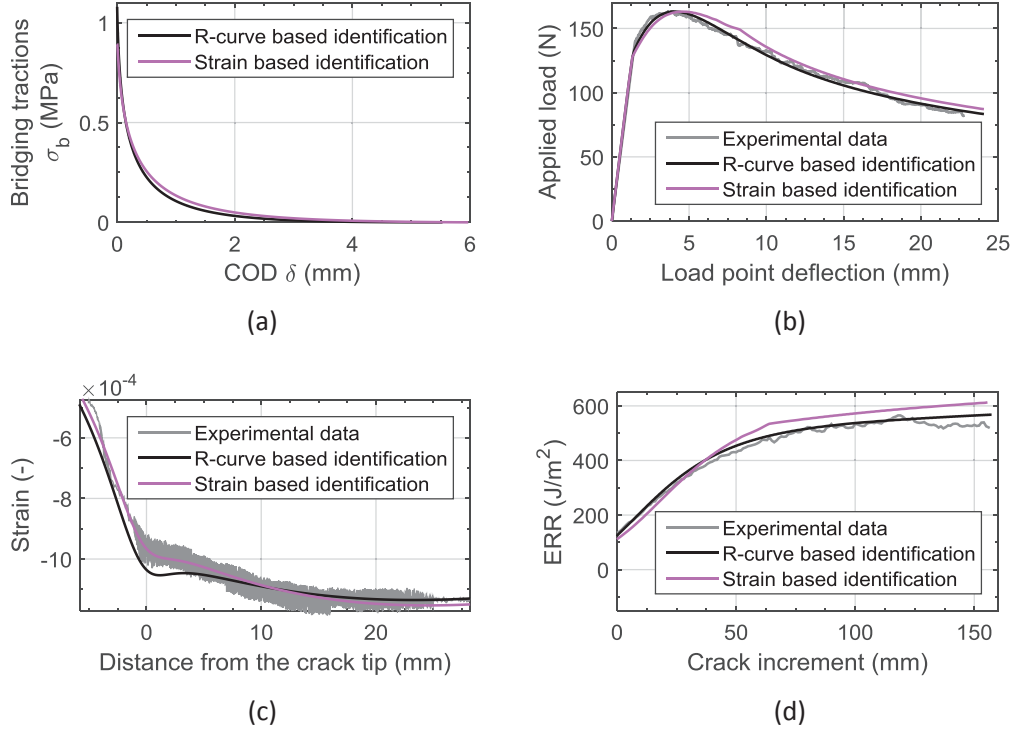


Fig. 3.16: For the interlaminar fracture of a $t=0.150$ mm M40JB/TP80EP specimen, data obtained from (i) the experiment, (ii) a R-curve based identification and (iii) a strain based identification: (a) Bridging tractions distributions; (b) Load-displacement curves; (c) Strain profile in the vicinity of the crack tip at steady-state; (d) R-curves.

The application of the method to the mode I interlaminar fracture of a $t=0.150$ mm M40JB/TP80EP specimen is used to validate some specific aspects:

- Convergence to a unique set of parameters: Starting with different initial tractions profile, the identification scheme always converges and yields to the same set of parameters. This convergence to a practically unique solution is expected since the method consists in solving a nonlinear system of three equations (eq. (3.17) (b-d)) and three unknowns.
- Parametric function: The shape of the parametric function is one of the assumptions of the method. This form is sufficiently generic to successfully represent the bridging tractions. If the parametric function is not suitable, it would fail to predict accurately the load-displacement curves, which is

the case for example for linear decay traction-separation relations (Fig. 3.17 (a)). Moreover, ERRs values computed by integration of eq. (3.17) (c) for other points on the R-curve, match very well the experimental R-curve and thus further validate the shape of the parametric function (Fig. 3.17 (b)).

- Sensitivity: On one hand, the procedure is sensitive to the input data, so that a large range of bridging intensities can be identified. On the other hand, the method is insensitive to the choices adopted to select the input data points. Considering identification point $a = a_1$ at 40, 50 and 60% of $G_{I,b}$ does not affect noticeably the identified traction-separation profile. Note that this verification would not be true if the parametric function was not suited to the case study. The length of the bridging zone z_{\max} is also selected as an input data. Since the plateau is not always clearly defined, this estimation is sometimes subjective. This length directly influences δ_{\max} , but the overall traction-separation relation is not changed significantly, since the other parameters are adapted consequently. Therefore, the traction-separation profile is energetically well identified, but the values of δ_{\max} and σ_{\max} should not be over-interpreted, since they might be subjective to the estimation of z_{\max} .

As a conclusion, the proposed method is robust and rapid, since it converges in a few iterations and is computationally cost effective. It can also be applied to the average R-curve data of each series of tests, rather than on a limited number of selected specimens in order to increase the pertinence of the identified traction model. The global response can be predicted accurately on a large range of bridging intensities. However, the specific values of the identified parameters should not be over-interpreted, since only the overall traction-separation distribution is verified.

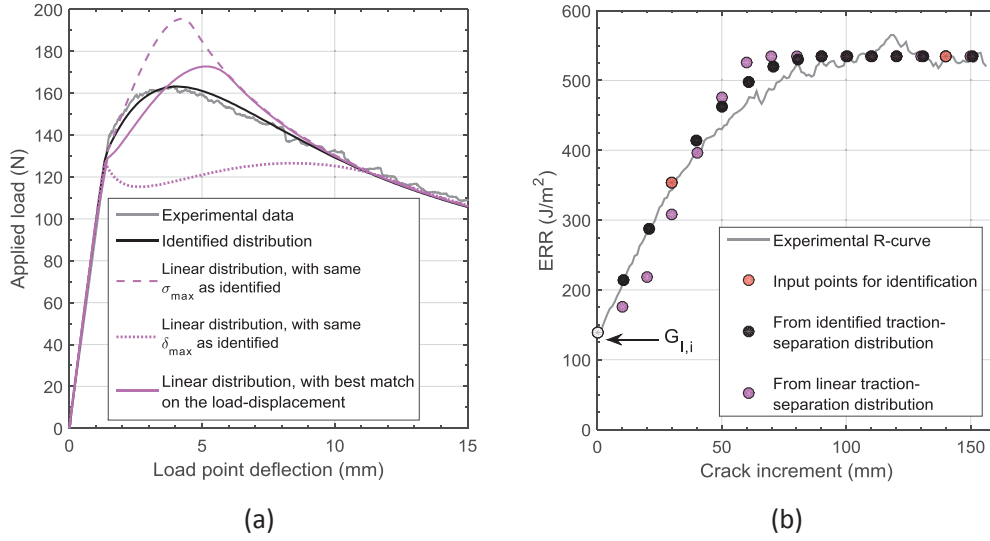


Fig. 3.17: (a) Load-displacement curves obtained from the R-curve based identification and linear distributions. (b) ERR values computed by integration of the identified bridging profile and linear distribution.

3.3.2 Cohesive element modeling of DCB specimens

In this work, crack propagations are simulated using the Abaqus' ability to model cohesive tractions by interpolation of damage vs COD data listed in tabular form. The cohesive traction-separation relations representing the fracture of DCB specimens consist in three parts, as depicted in Fig. 3.18:

- A high penalty stiffness representing the undamaged linear response;
- A linear stiffness degradation modeling the matrix cracking in the crack tip process zone;
- The identified nonlinear stiffness degradation associated with fiber bridging.

The traction-separation relation obtained with the R-curve based identification procedure must be slightly revised to be implemented in the cohesive relation, since a small part of the external work is stored as elastic energy in the cohesive elements due to their stiffness. Otherwise, it would fail to model precisely the evolution of the dissipated energy during damage growth. As schematized in Fig. 3.18, the increment of dissipated energy in the cohesive zone approach dE_{coh} (Fig. 3.18 (b), eq. (3.18)) must match the increment of dissipated energy identified in the fracture mechanics approach dE_{FM} (Fig. 3.18 (a), eq. (3.19)) for each discretization of the COD δ_i .

Keeping the same COD discretization in the identified and modified representations (eq. (3.20) (a)), the corrected tractions are computed incrementally according to eq. (3.20) (c), starting from the end of the bridging zone (eq. (3.20) (b)).

$$dE_{FM} = \frac{(\sigma_A + \sigma_B)(\delta_B - \delta_A)}{2} \quad (3.18)$$

$$dE_{coh} = \frac{\sigma_1 \delta_2 - \sigma_2 \delta_1}{2} \quad (3.19)$$

$$\begin{cases} \delta_2 - \delta_1 = \delta_B - \delta_A, \forall (\delta_A, \delta_B) & (a) \\ \sigma_2(\delta_{max} + \hat{\delta}) = 0 & (b) \\ \sigma_1 = ((\delta_2 - \delta_1)(\sigma_A + \sigma_B) + \sigma_2 \delta_1) / \delta_2, \forall (\delta_1, \delta_2) & (c) \end{cases} \quad (3.20)$$

The indices 1 and 2, respectively A and B , stand for two consecutive increments in the cohesive zone and fracture mechanics approaches. $\hat{\delta}$ is the COD at the end of the matrix cracking zone.

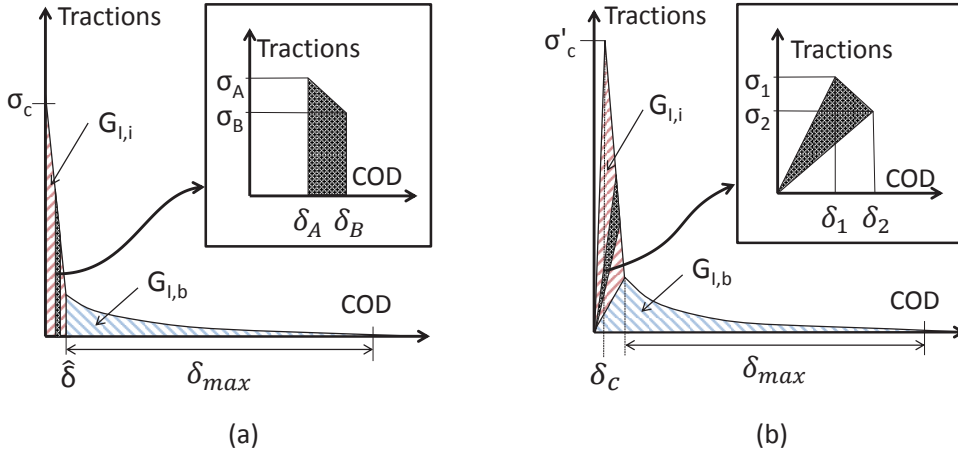


Fig. 3.18: Dissipated energy (a) in the fracture mechanics and (b) cohesive element approaches.

The cohesive relation is represented in Abaqus® as a damage parameter D which evolves from zero below damage threshold to unity at the failure of the element. The damage vs opening relation is computed based on the corrected cohesive relation using eq. (3.21) and is introduced in tabular form with at least 300 entries:

$$D_i(\delta_i) = 1 - \frac{k_i}{k_0} = 1 - \frac{\sigma_i / \delta_i}{\sigma'_c / \delta_c} \quad (3.21)$$

k is the stiffness, σ'_c and δ'_c are the stress and COD at damage initiation. The initial stiffness k_0 is firstly estimated to 1/10 of the COD at the end of the matrix cracking zone and then progressively increased until convergence of the simulated results.

3.3.3 Cohesive element modeling of compact tension (CT) specimens

The translaminar fracture of CFRP involves several dissipative mechanisms such as matrix cracking, fiber/matrix debonding, fiber breakage and fiber pull-out. Although these mechanisms are dispersed on a relatively large volume, the cohesive element model assumes a single crack plane where all the dissipative mechanisms are concentrated.

The shape of the cohesive traction-separation relation is not known a priori. Therefore, in a prospective phase, a multilinear cohesive law with six independent parameters is implemented in order to find the generic shape of the cohesive law. The maximal opening δ_m is estimated from the maximal COD at the crack starter measured optically on the experimental specimens. The opening range is divided into six equally spaced segments at $\delta_{1,...,5,m}$. The six parameters σ_i represent the tractions at the beginning of each segment, as schematized in Fig. 3.19. Since the closing tractions must be positive and the material cannot recover its damage, a condition exists on the stress level as a function of the stress at the previous segment in order to ensure that damage can only grow:

$$0 \leq \sigma_i \leq \sigma_{\max,i} \quad , \quad \text{where } \sigma_{\max,i} = \frac{\delta_i}{\delta_{i-1}} \sigma_{i-1} \quad , \quad i=1,...,5 \quad (3.22)$$

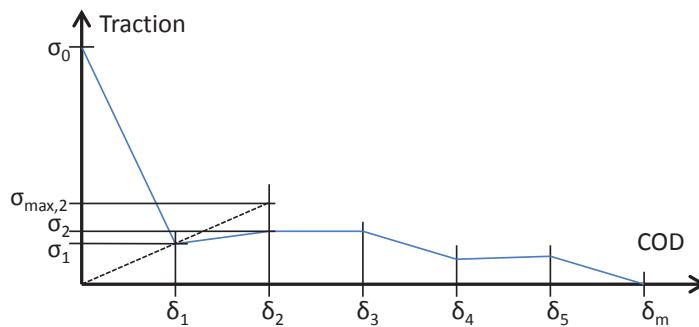


Fig. 3.19: Multilinear traction-separation relation. Illustration of the upper bound for the traction σ_2 .

The so-built multilinear cohesive law is implemented in Abaqus via a Matlab script and optimized with the experimental load-displacement curve as an objective function for one of the $t=0.075$ mm CP specimens studied in chapter 7. Interestingly, the optimized multilinear cohesive relation consists in three parts (Fig. 3.20):

- A high penalty stiffness representing the undamaged linear response until a stress level σ_0 corresponding approximately to the strength of the unnotched CP laminate;
- On the first segment, a linear stiffness degradation representing progressive fiber debonding and failure, which can be associated with the ERR required to initiate the crack propagation;
- On the other opening segments, an almost constant traction level approximately 30 times lower than the initial traction, which can be related to the ERR increase between crack initiation and steady-state propagation.

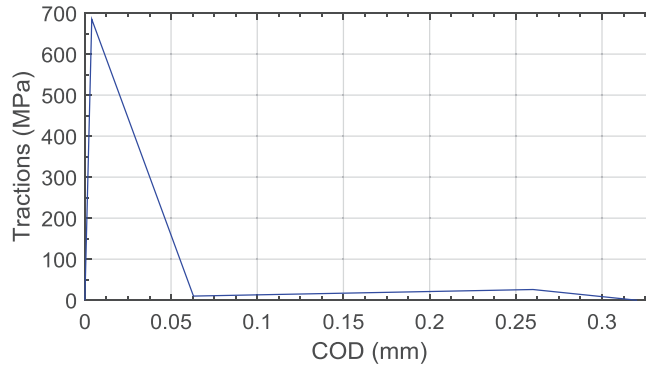


Fig. 3.20: Identified traction-separation relation for a representative $t=0.075$ mm CP specimen.

The optimization requires iterative resolutions of the FE cohesive simulation of crack propagation to minimize the residual between experimental and simulated load-displacement response. This optimization procedure being computationally expensive and time consuming, it is not applied for each series of tests. However, based on this prospective work, the shape of the cohesive relation can be assumed to be represented as depicted in Fig. 3.21 and represented by four parameters: σ_c , δ_m , $J_{I,i}$ and $J_{I,ss}$. These four parameters can be estimated experimentally:

- σ_c is the strength of the unnotched laminate;

3.3 Numerical procedure

- δ_m is the COD measured optically at the crack starter when the crack reach steady-state propagation;
- $J_{I,i}$ and $J_{I,ss}$ are the fracture toughness at initiation and steady-state, respectively, as measured on the R-curve of CT specimens.

Predictions and discussion of those simplified modeling hypotheses are discussed in section 7.3.

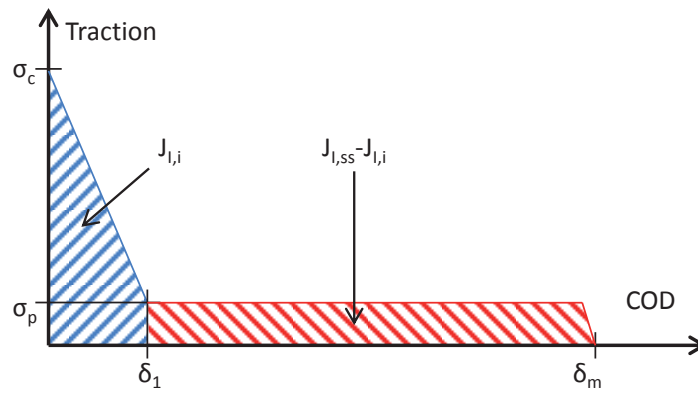


Fig. 3.21: Simplified traction-separation relation for the CT specimens.

Chapter 4

Interlaminar fracture

The mode I interlaminar fracture of laminated CFRP exhibits a strong R-curve behavior due to a dominant toughening mechanism: fiber bridging. As shown in previous studies [36, 37], the large scale bridging is highly size dependent. In particular, the specimen thickness strongly influences the development of fiber bridging. The ply thickness, which is another characteristic length of the laminated composites, might also affect the fiber bridging. This chapter is dedicated to the characterization of the ply thickness effect on the ERR in monotonic interlaminar fracture of UD laminates. Firstly, experimental tests are performed under mode I and II in order to quantify the ERR at initiation and subsequent growth. Secondly, mechanistic investigations are conducted to characterize the laminate microstructure ahead of the crack tip and the bridging fibers in the wake of the crack in order to find an explanation for the observed effects. Finally, the R-curve based identification procedure is applied on the experimental data to obtain the traction-separation profiles associated with fiber bridging and implement cohesive element simulations.

4.1 Mode I experimental testing

4.1.1 Specimens and data reduction

The ply thickness effect on the mode I interlaminar fracture is characterized experimentally by testing three different ply thicknesses: $t=0.030$, 0.75 and 0.150 mm. Since the specimen thickness is known to influence the fiber bridging development, two specimen thicknesses, $h=2$ and 8 mm, are considered in addition to the nominal thickness $h=4$ mm. The specimen's width is kept constant ($b=25$ mm), as it does not influence the R-curve behavior. The specimen's length is set sufficiently long to reach the steady-state crack propagation within the specimen. The initial crack length a_0 is comprised between 55 and 65 mm. In every case, it fulfils the

4. Interlaminar fracture

criteria imposed by the ASTM standard to avoid large deflection of the specimen arms [38]:

$$a_0 \leq 0.042 \sqrt{\frac{h^3 E_1}{G_{I,i}}} \quad (4.1)$$

The most limiting case is the thinnest specimen ($h=2$ mm), where a_0 should be smaller than 130 mm. Since loading blocks are used, the initial crack length is recommended by the ASTM standard [38] to be larger than 50 mm, so that the influence of the blocks can be neglected. The large displacements correction recommended by the standard is applied in the data reduction procedure and reaches 6.4% in the worst case ($t=0.150$ mm, $h=2$ mm). The specimen's dimensions are summarized in Table 4.1. The specimens are produced and prepared as explained in section 3.1.1. Representative specimens of the three different specimen thicknesses are shown in Fig. 4.1. In total thirty-one specimens of seven ply thickness / specimen thickness combinations are tested.

Table 4.1: Dimensions of the specimens for interlaminar fracture testing.

Denomination	Number of speci- mens (-)	g (g/m ²)	h (mm)	b (mm)	l (mm)	a_0 (mm)
DCB_INTER_30_2	4	30	2.02 ± 0.01	24.96 ± 0.01	210	59.0 ± 2.2
DCB_INTER_30_4 *	4	30	3.88 ± 0.04	24.86 ± 0.10	180	64.7 ± 0.5
DCB_INTER_30_8b	4	30	8.46 ± 0.15	24.94 ± 0.01	210	59.3 ± 0.5
DCB_INTER_75_4 *	4	75	3.79 ± 0.03	24.92 ± 0.05	180	60.0 ± 0.0
DCB_INTER_150_2	5	150	1.96 ± 0.02	24.96 ± 0.01	210	56.6 ± 1.1
DCB_INTER_150_4	5	150	3.88 ± 0.02	25.09 ± 0.04	180	57.6 ± 0.6
DCB_INTER_150_8b	5	150	7.98 ± 0.02	24.92 ± 0.02	280	62.0 ± 1.6

* Embedded optical fiber

4.1 Mode I experimental testing

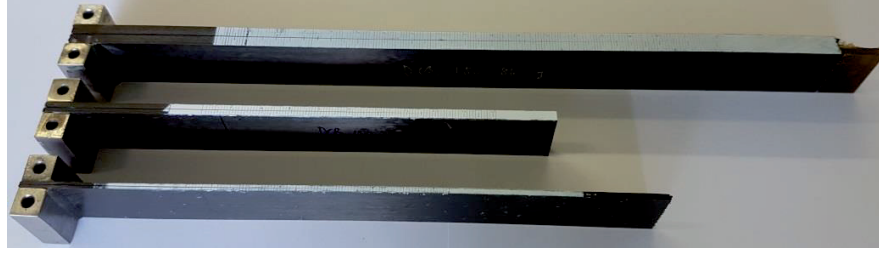


Fig. 4.1: DCB specimens with $h=2, 4$ and 8 mm ($t=0.150$ mm) for interlaminar fracture testing.

The specimens are tested in mode I monotonic opening under a constant displacement rate of 2.4 mm/min, whatever the specimen thickness. Since the thick specimens are stiffer than the thin ones, a given applied displacement results in a longer crack in the thick specimens (Fig. 4.2 (a)). The crack propagation speed is therefore larger in the thicker specimens (Fig. 4.2 (b)) but remains sufficiently low to consider quasi-static crack propagation.

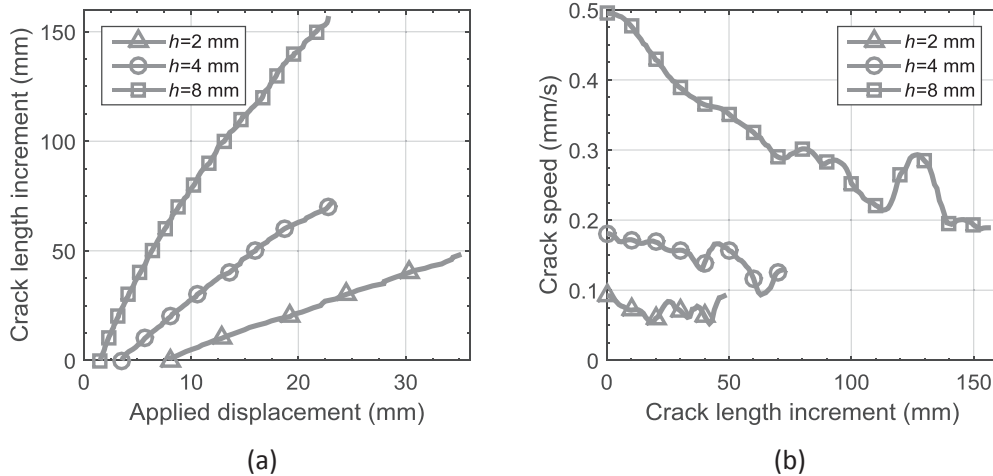


Fig. 4.2: For $t=0.150$ mm and $h=2, 4$ and 8 mm specimens, (a) crack length increment vs applied displacement and (b) crack speed vs crack length increment.

Since the ERR is computed based on the compliance calibration method CC3, as described in section 3.1.3.1, it is necessary to verify that the linearity assumption is valid. In the specimens equipped with FBG sensors embedded 0.3 mm above the crack plane, the recorded axial strain does not exceed 0.3% , which is below the linear-elastic limit of the composite. Moreover, the strain energy stored in the specimen at the maximal applied displacement, computed by numerical integration of the unloading curves, differs by less than 8% when compared to the energy estimated assuming linearity. This discrepancy can be explained by the crushing of the intact

bridging fibers during unloading. Furthermore, static numerical simulations corresponding to the largest experimental crack length increment differ by 1% when changing from the linear to the non-linear geometrical formulations, which practically exclude any geometrical non-linearity. Finally, a selected specimen is equipped with the targets shown in Fig. 3.10 (a), allowing the measurement of the relative angle between both specimen's arms. The J-integral is then computed using eq. (3.3) and compared with the ERR obtained by compliance calibration. At steady-state, the obtained relative difference is smaller than 5%. Based on these considerations, the system is assumed linear elastic for the study of the interlaminar fracture, which allows using the compliance calibration method for the data reduction.

4.1.2 Ply thickness effect

The ply thickness influences the global response of the DCB specimens. Fig. 4.3 shows representative load-displacement curves of $h=4$ mm thick specimens for three different ply thicknesses. The peak load reached in the $t=0.030$ mm specimens is 32% lower than in the $t=0.150$ mm specimens. The difference in initial stiffness between the different curves is due to variations of the initial crack length and small discrepancies of specimen thickness (see Table 4.1). As shown previously by Amacher et al. [3], the ply thickness does not influence the longitudinal modulus as long as the fiber volume fraction is kept the same. The residual displacement at the end of the unloading curves, which is mainly due to the crushing of bridging fibers, is very small. It confirms that the linear-elastic behavior assumed in the compliance calibration data reduction method is valid for these tests.

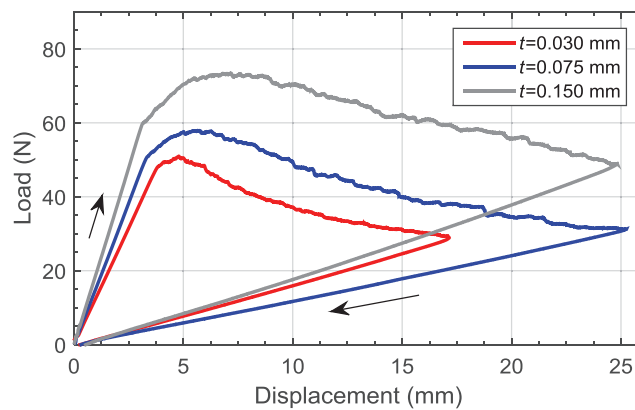


Fig. 4.3: Representative load-displacement curves as a function of the ply thickness ($h=4$ mm).

The average R-curves for the seven series of tests described in Table 4.1 are shown in Fig. 4.4. The results for the nominal $h=4$ mm thick specimens, represented in thick lines, are completed with measurement on two other specimen thicknesses ($h=2$ and 8 mm, light lines). The ERR at initiation is practically identical whatever the specimen and ply thickness: $G_{I,i} = 140 \pm 11 \text{ J/m}^2$. At subsequent crack growth, the ERR is however strongly influenced by both the ply and specimen thicknesses. The R-curves converge to a steady-state plateau level for each curves, except for the $t=0.150$ mm specimens. However, recalling that the fitting function selected in this work converges more slowly towards a plateau than the functions proposed in the ASTM standard [38], it can be assumed that the maximum bridging length is nearly reached. Assuming a similar behavior as in the other specimens and considering the trend of the data, the expected steady-state ERR values are within 5% of the last recorded value. Therefore, the maximum ERRs obtained in the $t=0.150$ mm specimens are considered as the steady-state value.

The so-obtained initiation and steady-state ERR values are summarized in Fig. 4.5. The steady-state ERR is 1.4 to 3.4 times higher than the initiation ERR, depending on the ply and specimen thickness, which shows the importance to characterize the whole R-curve rather than only the initiation value. Changing from standard ply thickness ($t=0.150$ mm) to thin-ply ($t=0.030$ mm), the steady state energy is decreased by 47 to 61%, depending on the specimen thickness. This strong decrease is explained by a reduction of 74 to 82% of the ERR associated with fiber bridging $G_{I,b} = G_{I,tot} - G_{I,i}$. As expected, the specimen thickness also influences the steady-state ERR. However, its influence is less pronounced than the effect of ply thickness. This trend is confirmed by fitting a linear model having the normalized ply thickness and specimen thickness as parameters:

$$G_{I,tot,ss} = 73 + 327 \cdot \bar{t} + 115 \cdot \bar{h} \text{ J/m}^2 \quad (4.2)$$

Where \bar{t} is the ply thickness normalized by 0.150 mm and \bar{h} the specimen thickness normalized by 8 mm. Finally, it can be noticed that for the $h=4$ mm specimens, for which three ply thicknesses are tested, the steady-state ERR scales almost linearly with the ply thickness.

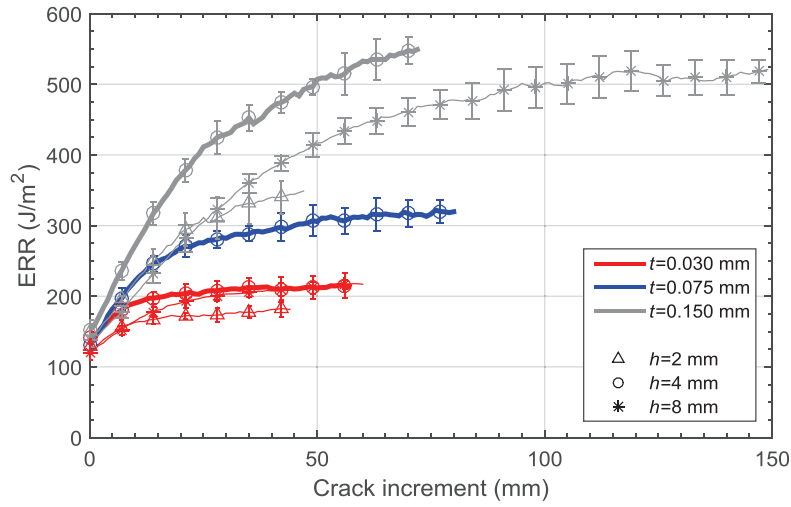


Fig. 4.4: Average R-curves for different ply thicknesses (color) and different specimen thicknesses (symbol).

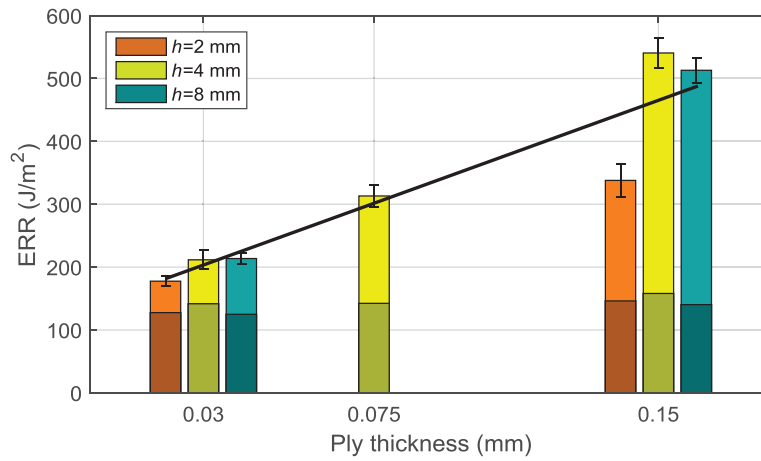


Fig. 4.5: ERR at crack initiation (dark colors) and steady-state propagation (light color).

4.2 Mode II experimental testing

The ply thickness influence on the mode II interlaminar fracture is characterized experimentally by testing three different ply thicknesses: $t=0.030$, 0.100 and 0.150 mm. The specimen thickness ($h=4$ mm), width ($b=25$ mm) and length ($l=200$ mm) are kept constant for each series of tests. The exact dimensions and initial crack lengths are summarized in Table 4.2.

4.2 Mode II experimental testing

Table 4.2: Interlaminar fracture specimen's dimensions

Denomination	Number of specimens (-)	g (g/m ²)	h (mm)	b (mm)	l (mm)	a_0 (mm)
4ENF_30_4	3	30	4.16 ± 0.03	25.07 ± 0.06	200	59.67 ± 0.58
4ENF_100_4	4	100	3.97 ± 0.06	24.99 ± 0.02	200	62.25 ± 0.50
4ENF_150_4	3	150	3.88 ± 0.02	24.97 ± 0.01	200	59.83 ± 0.29

The specimens are tested in mode II by loading the specimen in bending. The test is controlled in displacement, with a constant displacement rate of 0.6 mm/min. The inner support span is set to 94 mm and the outer span to 188 mm. As explained in section 3.1.3.2, the data reduction is done by compliance calibration, with a linear fitting function. This function, which is determined by the simple beam theory, is appropriate since the fitting of the experimental data gives R^2 values always larger than 0.993.

Fig. 4.6 shows a representative load-displacement curve for each of the three ply thicknesses. In every case, the residual displacement is very small (less than 0.05 mm). Moreover, the strain energy computed assuming linear-elasticity differs by less than 6.3% from the energy obtained by numerical integration of the unloading curves. This small difference validates the use of the compliance calibration for the computation of the ERRs.

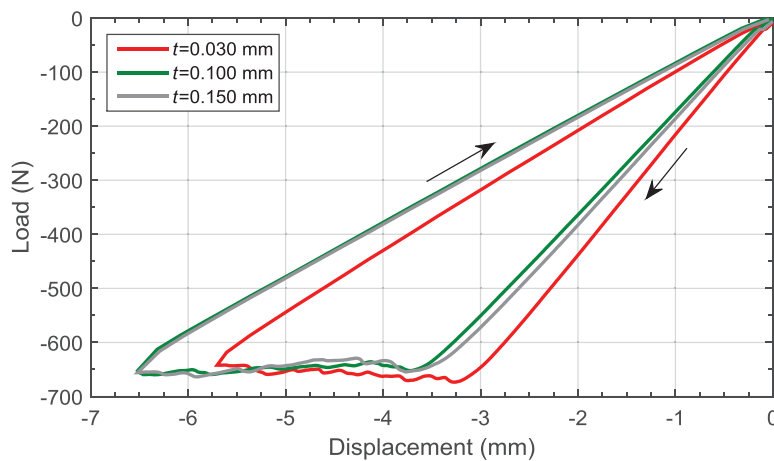


Fig. 4.6: Representative load-displacement curves as a function of the ply thickness ($h=4$ mm).

4. Interlaminar fracture

The average R-curves obtained for the three different ply thicknesses are shown in Fig. 4.7. They all show a steep increase on the first 5 mm of crack propagation followed by a relatively flat plateau at subsequent crack growths. The ERR values obtained at initiation might be influenced by the close presence of the loading roller and by the resin-rich region at the end of the PTFE insert. Moreover, it is difficult to precisely define the crack propagation initiation in mode II, since it is challenging to monitor accurately the crack length. For these reasons, the first 5 mm of propagation should not be over interpreted and the ERR at 5 mm of propagation can be considered as the initiation value $G_{II,i}$. At subsequent crack growths, the ERR values are nearly constant, which indicates the absence of significant toughening or other dissipative mechanisms such as fiber bridging. The whole dissipated energy can be associated with the creation of the new crack faces, under mode II loading.

Only three or four specimens are tested for each series of tests, since the standard deviations are small (in average, less than 5.8%). The average ERR values differ by maximum 62 J/m^2 (11%) between the largest value ($t=0.100$) and the smallest one ($t=0.030$) along the sixty millimeters of crack propagation. The ERR for the $t=0.150$ mm specimens is in average only 19 J/m^2 (3.6%) higher than the corresponding values for the $t=0.030$ mm specimens. It is not possible to highlight a clear effect of ply thickness on the mode II interlaminar fracture because the highest ERR values are obtained for the intermediate ply thickness ($t=0.100$ mm). Moreover, since the scatter of each curves overlap one with each other, the differences can be considered statistically insignificant.

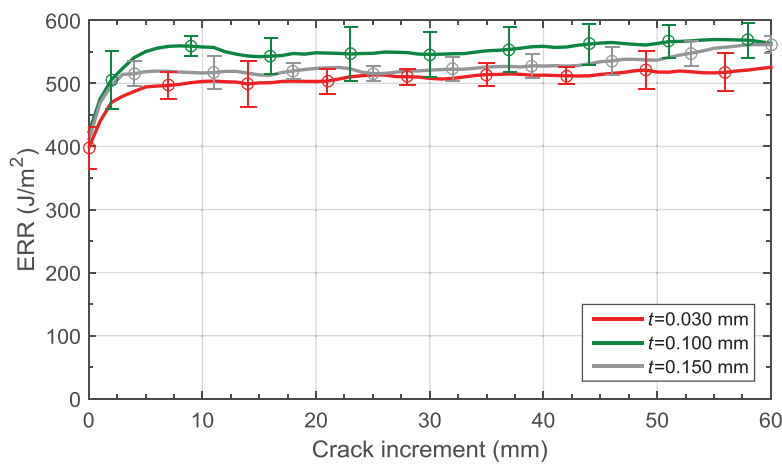


Fig. 4.7: Average R-curves for different ply thicknesses.

Fig. 4.8 summarizes the initiation and steady-state ERR under mode I and mode II loading conditions. While in mode I a clear R-curve behavior is measured, with fiber bridging as toughening mechanism, in mode II the initiation ERR is similar to the propagation value. In average, the initiation ERR is 3.7 times higher in mode II than in mode I. In the standard ply mode I fracture ($t=0.150$ mm), where fiber bridging is the most intense, the steady-state ERR is nearly equal to the mode II ERR.

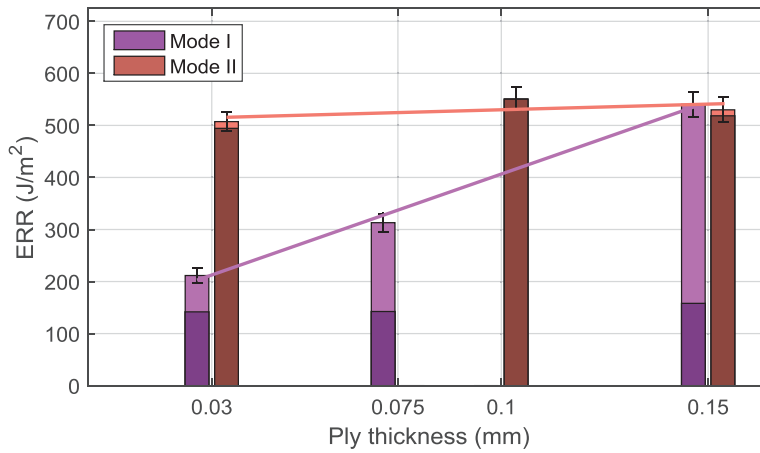


Fig. 4.8: Comparison of interlaminar fracture ERR under mode I and mode II loading ($h=4$ mm) at crack initiation (dark colors) and steady-state propagation (light colors).

4.3 Mechanistic investigations

Since the ERR in mode II is practically insensitive to ply thickness, the mechanistic investigations focus on the mode I interlaminar fracture. Fiber bridging is supposed to be the main mechanism responsible for the scaling effect since the ERR values at crack initiation are scale independent and only the bridging ERR contribution scales with ply thickness (Fig. 4.5). This hypothesis is supported by the side views of the DCB specimens indicating a decreasing amount of bridging fibers with decreasing ply thickness (Fig. 4.9). As fiber bridging is initiated by complex micro cracking and debonding phenomena at the microstructural level, the difference of fiber bridging intensity is potentially caused by differences of microstructure, which is influenced by the ply thickness. Therefore, the mechanistic investigations aim to characterize the microstructure and the bridging fibers bundle morphology to find potential correlations.

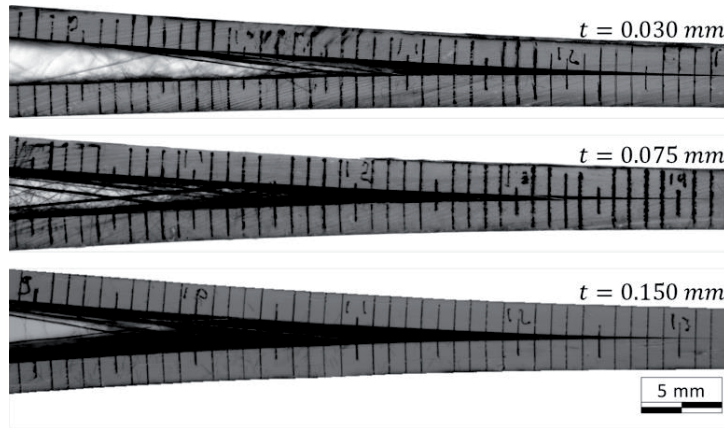


Fig. 4.9: Side views of DCB specimens, where fiber bridging decreases with ply thickness ($h=4\text{mm}$).

4.3.1 Microstructure analysis

The specimens, which differ only by their ply thickness, have significantly different bridging contributions to ERR. To try to explain this phenomenon, the link between microstructure morphology and fiber bridging density is investigated for different ply thicknesses. The microstructure of the laminates is characterized by observing cross sections of the specimens in the zone ahead of the crack tip. As shown in Fig. 4.10 (a)-(c), the fibers appear to be dispersed more uniformly in the thin-ply than in the thicker-ply laminates, leading to a more homogeneous microstructure. To quantify this visual observation, the coarseness measure is computed, using eq. (3.11). The coarseness is the standard deviation of the local fiber volume fraction normalized by the mean fiber volume fraction. Thus, it is a measure of the heterogeneity of the material at a given length scale. This value is sensitive to the size of the local windows selected to obtain the local fiber volume fraction. However, as shown in Fig. 4.10 (d), regardless of the size of the windows, the coarseness value is always significantly lower in the thin-ply laminate, meaning that the variations of local fiber volume fraction are smaller. On the opposite, the coarseness value is relatively high in the thick-ply laminate, indicating the presence of fiber-rich and matrix-rich regions and thus denotes a much more heterogeneous microstructure.

4.3 Mechanistic investigations

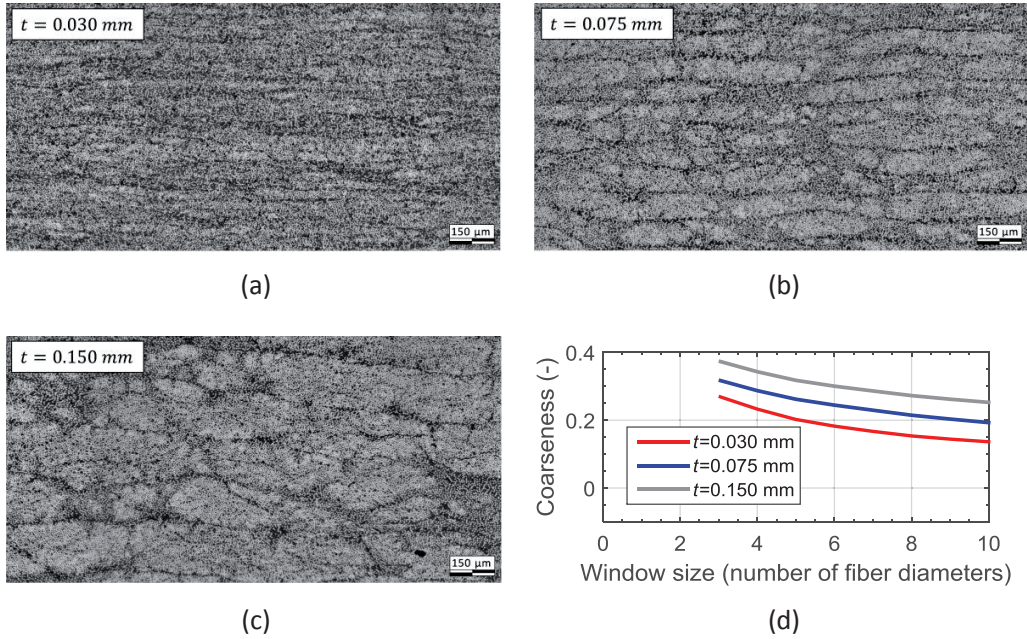


Fig. 4.10: (a)-(c) Representative cross sections for the three ply thicknesses; (d) Corresponding coarseness values.

The difference of homogeneity in the microstructure originates from the production of the prepregs. In order to produce thin prepregs, 12K tows are spread until reaching the required thickness and then impregnated with the resin. During this process, wider spread tow patterns are formed in the thin-ply prepregs than in the thicker ones. These rectangular patterns survive the whole stacking and curing procedures, leading to the patterned microstructure observed in Fig. 4.10. Regardless of the ply thickness, the layers are partially intermingled in the cured UD laminate and can hardly be distinguished one from each other's. Therefore, the crack front cannot be confined between two adjacent plies and must necessarily propagate partially within the plies. Moreover, as shown in [104], micro cracking in transverse loading tends to initiate in regions of high fiber fraction (clustering) and avoid resin-rich zones, which tends to favor mode I micro cracking initiation localized within plies instead of ply interface. In such a case, the interlaminar fracture R-curves could be expected to be of comparable magnitude as the intralaminar fracture R-curves. However, results of chapter 6 will show that it is not the case.

It should also be noted that the significant fiber rearrangement observed in this work is only possible in UD laminate and is caused by the very low viscosity of the resin used in this composite material. For other materials and in multidirectional

laminates different types of microstructure heterogeneity are to be expected, which could affect the scaling of bridging effects with respect to ply thickness.

Fig. 4.11 illustrates the crack profile along the width of a thin-ply ($t=0.030$ mm) and a thick-ply ($t=0.150$ mm) specimen, close to the crack tip. While the through-the-width profile is relatively flat in the $t=0.030$ mm specimen, it is much more wavy in the $t=0.150$ mm specimen. In particular, one can observe that the crack front avoids a particularly large matrix-rich region and follows a path in the fiber-rich regions, where the local stress state and distributed micro-cracking are increased. In several places, the crack jumps from one level to another one, leading to the observed waviness. Since the crack clearly propagates within fiber-rich rather than matrix-rich regions, one can state that the crack waviness is caused by the heterogeneous microstructure.

Fig. 4.12 shows 4 successive cross sections of the $t=0.150$ mm specimen, from the crack tip toward the wake of the crack. On the closest to crack tip cross section, one can observe a crack tortuosity similar to the one illustrated in Fig. 4.11. Due to this waviness, the crack moves from one side of a group of fibers to the other side. Therefore, this bundle of fibers is trapped on the wrong side of the crack, leading to the creation of a new bridging bundle. Such a mechanism generates and develops large bundles of bridging fibers, which exert significant closing forces and are deemed to be responsible for the ply thickness effect. To summarize, a heterogeneous microstructure produces a wavy crack front, which in turn initiates and develops large bundles of bridging fibers. In contrast, in a well homogenized microstructure, the crack front remains flat and thus inhibits the development of bridging bundles.

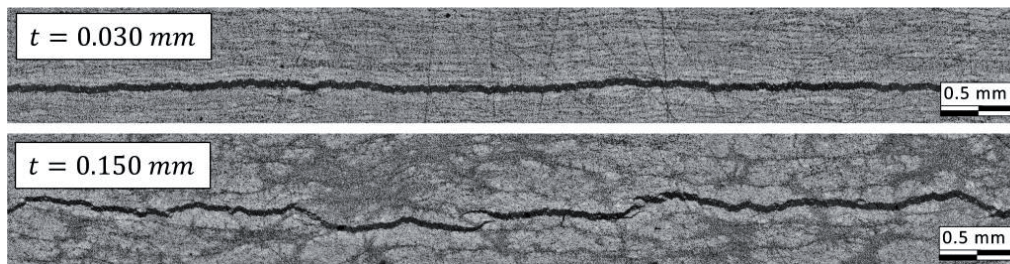


Fig. 4.11: Cross sections of $t=0.030$ and 0.150 mm fractured specimens.

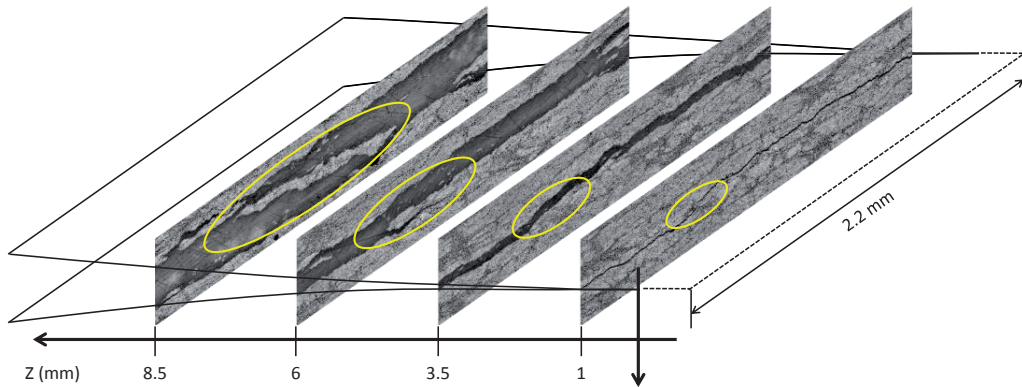


Fig. 4.12: Development of a fiber bridging bundle in a $t=0.150$ mm specimen. The ellipses show consecutive stages of the bundle.

4.3.2 Fiber bridging characterization

Since fiber bridging is the toughening mechanism responsible for the change of R-curve behavior with respect to the ply thickness, it is interesting to characterize and highlight the differences in bridging fibers and bundles of fibers for different ply thicknesses. To do this, microscopy images of the bridging zone spanning half of the width of the DCB specimens are produced from cross sections situated at a distance of 1 to ~ 40 mm from the crack front. The wake of the crack is then isolated from the bulk material using the magnetic lasso tool in Adobe Photoshop and the bridging fibers are isolated by thresholding using the magic wand tool in Adobe Photoshop. As illustrated in Fig. 4.13, the bulk material is replaced by black pixels and the bridging fibers by white pixels, so that the picture can then be analyzed automatically in Matlab.

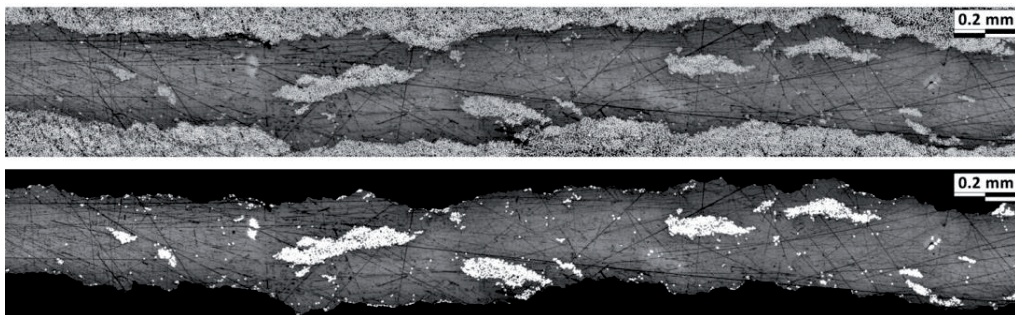


Fig. 4.13: Crack profile and bridging fibers / bundles.

4. Interlaminar fracture

In Matlab, each white region representing bridging fibers or bundles is treated separately. Dividing the connected areas by the area of a single fiber, the number of fibers in each region (bundles) and in the whole specimen can be estimated.

The development of fiber bundles, defined as cluster of at least ten fibers, is mainly detected in the specimens where the microstructure is relatively heterogeneous ($t=0.075$ and 0.150 mm). While the number of isolated bridging fibers decreases with decreasing ply thickness, the amount of bridging fibers clustered in bundles drops significantly in thin-ply laminates (Fig. 4.14). Fiber bridging in thin-ply mainly consists in isolated fibers (80%). In contrast, in thick-ply specimens, 70% of the bridging fibers are clustered in bundles. The large fiber bundles lead to longer bridging zones, since their strength is larger than in isolated fibers [105]. These bundles exert large closing forces and have a dominant contribution to the bridging ERR. Their lower amount in thin-ply laminate is obviously the main factor for the observed decrease in the steady-state ERR.

To summarize, the ply thickness influences the mode I R-curve behavior through a change in the homogeneity of the microstructure. It is hypothesized that the well homogenized microstructure observed in the thin-ply laminate reduces the amount and spread of micro-cracking in the zone ahead of the crack tip and helps the crack to remain on its flat plane (Fig. 4.11). Therefore, the development of large bridging fibers bundles is limited, leading to a lower energy contribution associated with fiber bridging in thin-ply laminates than in thicker ply laminates.

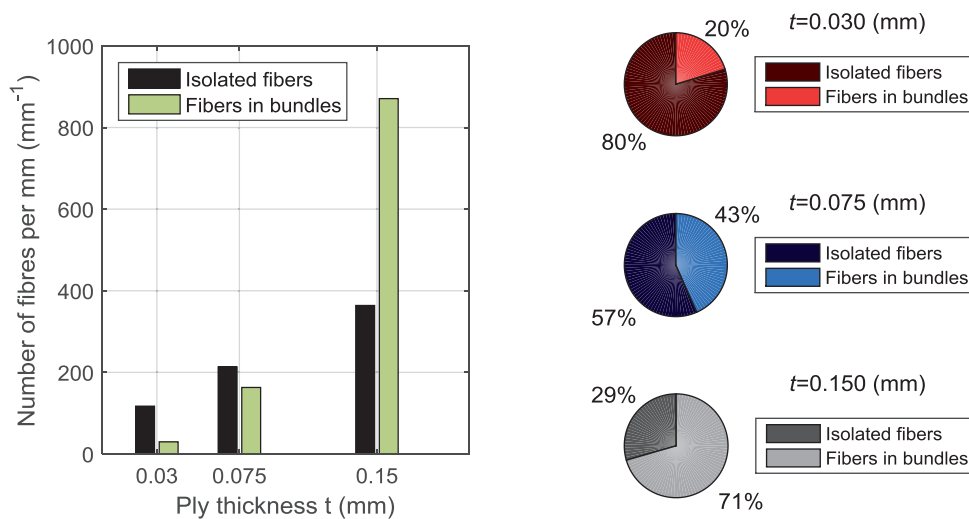


Fig. 4.14: Number of isolated bridging fibers and fibers clustered in bundles per millimeters of crack width.

4.4 Numerical modeling

4.4.1 Mode I

4.4.1.1 Identification of bridging tractions

The R-curve based fiber bridging identification method detailed in section 3.3.1.2 is applied on the data experimentally obtained on the $h=4$ mm thick specimens. The procedure is very time-effective and converges in less than ten minutes on two CPUs. Therefore, the method is not only applied on the average R-curves, but also with the mean values plus/minus the standard deviation, in order to obtain an interval of confidence on the fiber bridging distribution and predicted load-displacement curves.

The identified fiber bridging traction-separation profiles are plotted in Fig. 4.15 and the corresponding identified parameters summarized in Table 4.3. Each curve is highly non-linear, which confirms the necessity of having the exponential term in the parametric function. Due to this nonlinearity, the maximal tractions σ_{\max} and the maximal COD δ_{\max} are reached almost tangentially when the COD and the traction tend respectively to zero. Therefore, a small scatter is expected on these parameters and their numerical values should not be over-interpreted. The critical stress at bridging initiation σ_{\max} is found to be relatively independent of ply thickness with a mean value of 0.73 ± 0.07 MPa. The two other parameters have significantly different values, reflecting the clear ply thickness effect characterized experimentally. The COD at the end of the bridging zone δ_{\max} is divided by 8 from thick-ply to thin-ply specimens. This reflects the observation that the bridging zone length is much smaller for thin-ply. Moreover, the exponential decay parameter $\hat{\gamma}$ is much increased in thin-ply, highlighting a fast decay of tractions in thin-ply. Both trends are fully consistent with the observation that fiber bridging is mostly achieved by isolated fibers in thin-ply, which have an inherently limited extension range, while thicker-ply specimens show large bundles which can develop on much larger distance.

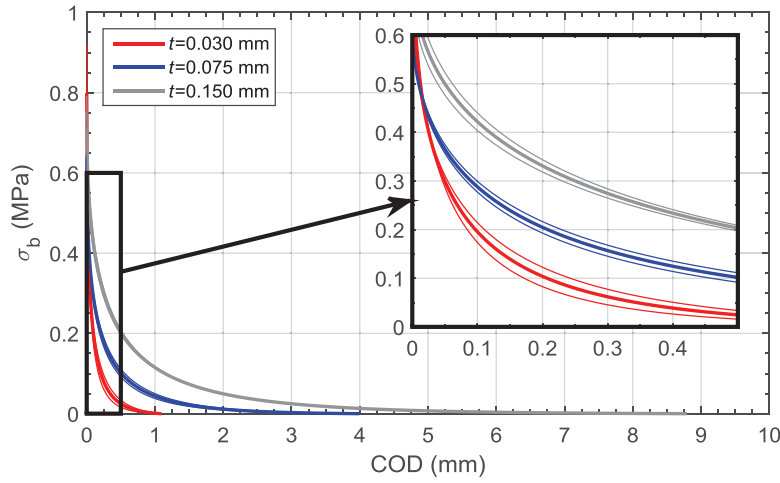


Fig. 4.15: Fiber bridging traction-separation profiles as a function of the ply thickness ($h=4$ mm). The thinner lines represent the identification based on the mean R-curves plus/minus the standard deviation.

Table 4.3: Identified fiber bridging parameters for different ply thicknesses ($h=4$ mm)

t (mm)	σ_{\max} (MPa)	$\hat{\gamma}$ (mm ^{-1/2})	δ_{\max} (mm)
0.030	0.80	3.30	1.08
0.075	0.64	1.99	3.97
0.150	0.75	1.46	8.77

4.4.1.2 Cohesive elements simulations

The identified traction-separation profiles are converted to cohesive relations following the procedure detailed in section 3.3.2. The ERR corresponding to the matrix cracking in the process zone ahead of the crack is represented by the measured ERR at crack initiation $G_{I,i}$ values reported in Fig. 4.5 and the critical stress σ_c is defined as the transverse tensile strength (23 MPa for each specimen). The critical COD which defines the initial stiffness is estimated to one tenth of the COD at the end of the matrix cracking zone and is verified to be sufficiently high so that the simulation results have converged with respect to the penalty stiffness parameter. The final cohesive stiffness is thus set in the range of 11000 to 12000 MPa/mm.

Given the relatively low bridging tractions compared to the transverse tensile strength, the damage parameter is already equal to $D \approx 0.995$ at the beginning of the zone representing the fiber bridging. Furthermore, Abaqus only considers six digits on the damage parameters, leading to a truncation of the end of the fiber bridging traction-separation profile. To overcome this problem, the obtained cohesive relation (blue line in Fig. 4.16) is split into two relations, one for the matrix cracking (red line in Fig. 4.16) and one for the fiber bridging (green line in Fig. 4.16). This way, the initial stiffness for the fiber bridging relation is much smaller, so that the damage parameter is defined more accurately. Both relations are implemented in two superimposed layers of cohesive elements acting similarly as two variable stiffnesses in parallel.

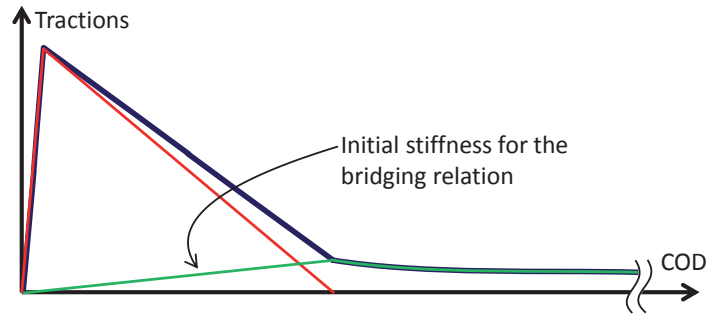


Fig. 4.16: Split of the cohesive relation.

The geometry of the DCB specimens is modeled in 2D plane strain condition, with approximately 50'000 8-nodes quadratic elements (CPE8R). The interlaminar fracture path is reproduced with two superimposed layers of 0.02 mm thick linear cohesive elements (COH2D4). Finally, the cohesive relations are implemented in tabular form with 300 entries for the matrix cracking part and at least 500 values for the fiber bridging profile. The maximal experimental applied displacement is imposed to two reference points kinematically coupled to the holes of the loading blocks.

The load-displacement curves obtained from the cohesive simulations are displayed in Fig. 4.17. The numerical simulations are in very good agreement with the experimental curves, in particular in the prediction of the load peak. This shows that the interlaminar fracture behavior in the transient part, where fiber bridging develops is well captured, as well as the steady-state propagation. The good agreement in the load-displacement curves is somehow expected, since the ERR is forced to be correct in two points of the R-curves. However, the global response can be precisely modeled only if the crack advance is also accurately predicted. This is indeed verified in the present case, since the predicted crack lengths vs applied displacements match the experimental data with less than 1.5 mm of relative error. Finally, the shaded areas in

Fig. 4.17 represent the intervals of confidence obtained from the identification done on the mean R-curves plus/minus the standard deviation. Interestingly, the size of the predicted intervals of confidence is of the same magnitude as the experimental scatter. This shows that the identification and simulation processes do not amplify the experimental errors and actually are able to represent the inherent variability of the fiber bridging process.

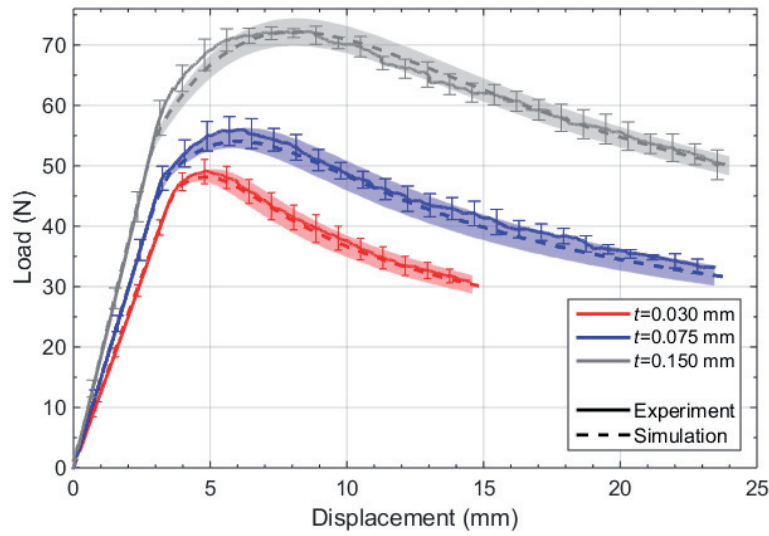


Fig. 4.17: Experimental and simulated load-displacement curves under mode I loading. (see text for details).

4.4.2 Mode II

In mode II, since the R-curve is practically constant, there is not any toughening mechanism in the wake of the crack and the traction-separation simply consists in the linear stiffness degradation representing the matrix cracking in the process zone ahead of the crack. The critical stress is set to the maximum in-plane shear stress (88 MPa) and the area under the traction-separation profile corresponds to the average mode II ERR ($G_{II} = 530 \text{ J/m}^2$ for $t=0.150 \text{ mm}$). The critical COD which defines the initial stiffness is estimated to 1/10 of the COD at failure of the element and progressively increased until convergence of the simulation results at 1/20. The cohesive law is implemented as mode independent in displacement based tabular form with 500 entries.

The flexure of the specimen is imposed through loading rollers modeled with a practically infinite stiffness. The interactions between the rollers and the specimen

are hard frictionless contacts. The maximal experimental applied displacement is imposed to a reference point kinematically coupled to the rigid profile holding the two central rollers. The two external rollers are fully constrained. Since there is no significant ply thickness effect on the mode II ERR, the cohesive simulation is done for a single specimen with $t=0.150$ mm. The numerical load-displacement curve is in very good agreement with the experimental one. As expected from the beam theory and from the constant ERR values obtained in the R-curves, the compressive load stays constant as soon as the maximal shear stress is reached in the specimen. The crack length is verified to be accurately predicted. At an imposed displacement $\Delta = 6$ mm, the difference between the experimentally measured crack length increment and the numerical one is smaller than 0.4 mm (0.54% relative error).

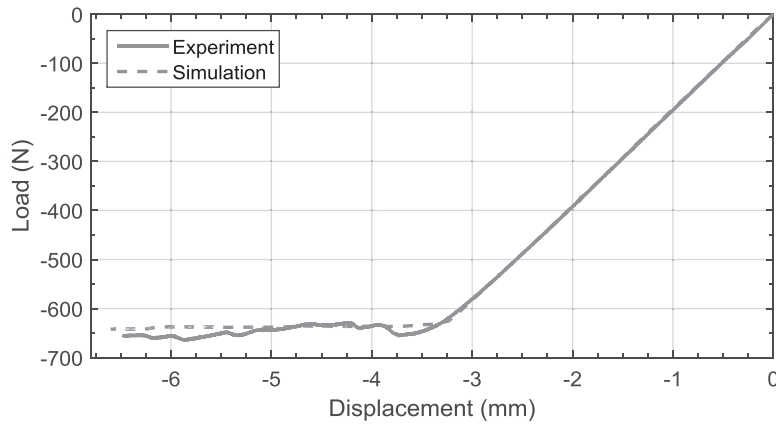


Fig. 4.18: Experimental and simulated load-displacement curve for a $t=0.150$ mm specimen loaded in mode II.

4.5 Summary

The experiments show that the ply thickness significantly influences the mode I interlaminar fracture. While the ERR at onset of propagation is found independent from the ply thickness, the steady state ERR and bridging length are considerably decreased in thin-ply when compared to thicker ply laminates. So, the thin-ply laminate sustains a lower crack driving force than the standard ply laminate.

This difference is attributed to a change in fiber bridging behavior. The thin-ply laminate has a much more homogenized microstructure than the thicker ply laminates which exhibit fiber- and matrix-rich regions. This inhomogeneity, which is governed by the tow spreading process involved in the production of the prepregs,

leads to high local stress values, a high likelihood of creating a large spread of micro-cracks and eventually to a wavy crack front. Such a roughness promotes the creation of large bundles of bridging fibers which exert important closing forces and increase the steady-state ERR. On the opposite, the well homogenized microstructure of the thin-ply laminate lets the crack front remain flat, which prevents the development of bridging bundles. This keeps the ERR level to relatively low values, close to the initiation value.

This size effect can be simulated with cohesive element models. The fiber bridging closing tractions profiles are identified with an effective method based on the R-curve. The scaling is reflected in the traction-separation profile by a reduction of COD at the end of the bridging zone and an increase in the exponential decay parameter for thinner plies. The maximal traction occurring at the crack tip is however relatively similar for each ply thickness. The cohesive simulations very accurately predict the load-displacement responses for each ply thickness. In particular, the peak load, which is reached when fiber bridging is not yet fully developed, is well predicted. An interval of confidence on the global response of the system can be obtained by applying the identification method on the average R-curves plus/minus the standard deviation.

The mode II interlaminar fracture is not affected significantly by the ply thickness. The obtained R-curves are relatively constant, indicating the absence of toughening mechanisms acting in the wake of the crack. In such a case the cohesive relation is mainly dominated by the ERR level. A critical stress level corresponding to the maximum in-plane shear stress followed by a linear stiffness degradation is shown to predict accurately the load-displacement response of the 4ENF specimens.

Chapter 5

Intralaminar fracture

The mode I intralaminar fracture of laminated CFRP is generally associated with large scale bridging of larger intensity than in interlaminar fracture. Comparing the work of Farmand-Ashtiani et al. [36] on interlaminar fracture and Pappas and Botsis [59] on the intralaminar fracture of the same material, it is shown that while the same ERR is measured at crack initiation, the steady-state ERR is approximately 2.7 times higher in intralaminar fracture. Pappas and Botsis show that the intralaminar fracture is strongly influenced by the specimen thickness. The ply thickness, which influences the mode I interlaminar fracture, might also affect the fiber bridging development in intralaminar fracture. Since the mode II interlaminar fracture is shown to be independent of ply thickness, the study on the intralaminar fracture is limited to mode I. This chapter is therefore dedicated to the characterization of the ply thickness effect on the ERR in monotonic mode I intralaminar fracture of UD laminates. Firstly, the ERR at crack initiation and subsequent crack growths is quantified experimentally. Secondly, mechanistic investigations are carried out to characterize the bridging fibers and bundles of fibers. Finally, traction-separation models are identified and cohesive element simulations are implemented to predict the intralaminar fracture as a function of the ply thickness.

5.1 Experimental testing

5.1.1 Specimens and Data reduction

The ply thickness effect on the mode I intralaminar fracture is characterized experimentally by testing three different ply thicknesses: $t=0.030$, 0.075 and 0.150 mm. To distinguish the effect of ply thickness from effect associated with the specimen geometry, two specimen configurations are used: DCB specimens ($h=6$ and 10 mm) and CT specimens. The specimen's width is kept constant and corresponds to

5. Intralaminar fracture

the thickness of the composite plates. The length of the DCB specimens is chosen sufficiently large to ensure that the crack can reach steady-state propagation. The initial crack lengths range from 54 to 65 mm, which fulfils the criteria imposed by the ASTM standard (eq. (4.1) [38]). The CT specimens allow approximately 20 mm of crack propagation, which is not sufficient to reach steady-state propagation. However, this dimension is large enough to characterize the crack initiation and first millimeters of subsequent growth. The CT specimens are pre-cracked at different lengths, at approximately 20, 22.5, 25 and 27.5 mm to exclude any effects due to the initial crack length. All the specimens for intralaminar fracture testing are produced from the plates referred as INTRA_30, INTRA_75 and INTRA_150 in Table 3.1. They are prepared as explained in section 3.1.1 and their dimensions are summarized in Table 5.1. Representative specimens of the CT specimens and DCB specimens with thickness $h=6$ and 10 mm are shown in Fig. 5.1. In total, 38 specimens of eight different configurations are tested.

Table 5.1: Dimensions of the specimens for intralaminar fracture testing.

Denomination	Number of specimens (-)	g (g/m ²)	h (mm)	b (mm)	l (mm)	a_0 (mm)
DCB_INTRA_30_6	6	30	5.79 ± 0.04	10.63 ± 0.11	330	55.8 ± 2.6
DCB_INTRA_30_10	4	30	9.89 ± 0.17	10.67 ± 0.03	330	59.3 ± 0.5
CT_INTRA_30	4	30	60.03 ± 0.0	10.80 ± 0.15	65.08	20.2 – 27.5
DCB_INTRA_75_6	6	75	5.81 ± 0.01	10.02 ± 0.03	280	56.4 ± 4.2
DCB_INTRA_75_10	4	75	10.1 ± 0.01	10.00 ± 0.01	280	59.8 ± 1.7
CT_INTRA_75	4	75	60.06 ± 0.0	10.06 ± 0.09	65.13	20.1 – 27.6
DCB_INTRA_150_6	7	150	5.77 ± 0.02	9.94 ± 0.02	280	54.8 ± 0.4
DCB_INTRA_150_10	3	150	10.0 ± 0.03	9.92 ± 0.01	280	59.7 ± 0.6

5.1 Experimental testing

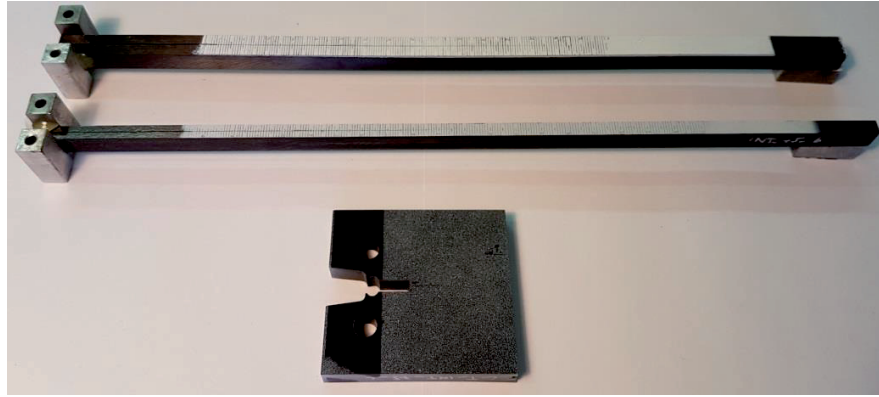


Fig. 5.1: CT specimen and DCB specimens with $h=6$ and 10 mm ($t=0.0750$ mm) for intralaminar fracture testing.

The specimens are tested in mode I monotonic loading with a constant displacement rate of 2.4 mm/min (DCB specimens) and 0.2 mm/min (CT specimens). The loading rate of the CT specimens is adjusted to have a crack speed of the same magnitude as for the DCB specimens. Indeed, since the CT specimens are much thicker than the DCB specimens, a given applied displacement rate results in a faster crack growth in the CT specimen compared to DCB (Fig. 5.2).

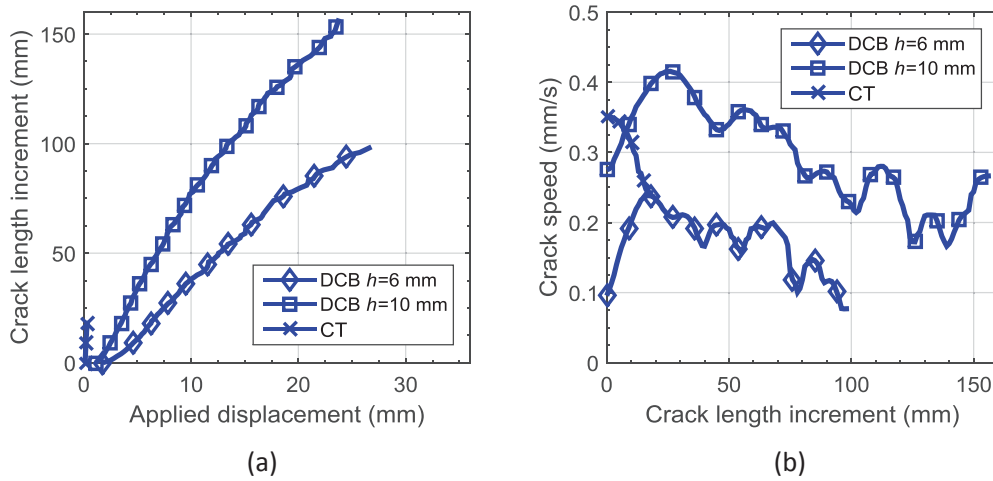


Fig. 5.2: For CT and DCB ($h=6$ and 10 mm) specimens, (a) crack length increment vs applied displacement and (b) crack speed vs crack length increment.

The ERR is computed based on the compliance calibration method, which assumes the linearity of the system. Since the specimens have the same or a larger thickness than the specimens tested in interlaminar fracture, their stiffness is larger and the strain level lower. Therefore, the linearity verifications explained in section 4.1.1 are

also valid for the current chapter. To obtain a validation of the results, the J-integral is also calculated for a majority of the specimens, using eq. (3.3).

5.1.2 Ply thickness effect

The ply thickness affects the global response of the DCB and CT specimens subjected to intralaminar fracture. While Fig. 5.3 (a) shows representative load-displacement curves of $h=6$ mm thick DCB specimens for three ply thicknesses, Fig. 5.3 (b) displays the corresponding curves of the CT specimens for the two ply thicknesses tested in this configuration. Since each DCB specimen has similar thickness, initial crack length and fiber volume fraction, the initial stiffness is equal for each test. The damage initiation, reflected in the loss of linearity in the load-displacement curve, occurs at a slightly higher load in the thin-ply specimens. The peak load is 8% higher in the $t=0.030$ mm specimens when compared to the $t=0.150$ mm specimens. In the post-peak region, the load is slightly lower in the thin-ply laminate. The residual displacement at the end of the unloading curves is approximately 1 mm and is mostly attributed to the crushing of detached bridging fiber bundles. The areas under the unloading curves differ by less than 6% from the energy computed assuming linear elasticity. This small value confirms that the linear-elastic behavior assumption is valid for the data reduction used in these tests.

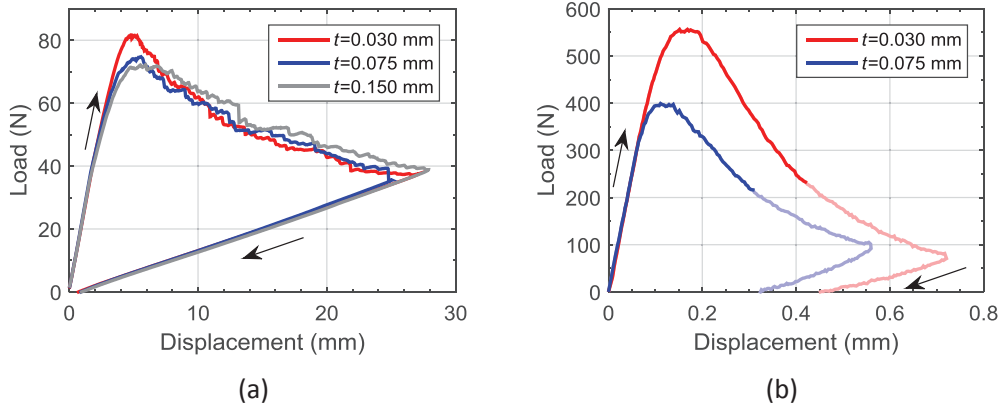


Fig. 5.3: Representative load-displacement curves as a function of the ply thickness for (a) DCB specimens ($h=6$ mm) and (b) CT specimens (light colors indicates the data not considered in the data reduction).

In the load-displacement curves obtained with the CT specimens, the peak load is also higher for the $t=0.030$ mm specimens. The specimens are tested until the ligament at the end of the specimen is smaller than 4 mm. At this stage of the loading, the behavior might not be linear-elastic anymore. This effect combined with

the crushing of intact bridging fibers leads to relatively large residual displacements. In the data reduction, the results are considered only for remaining ligament larger than 10 mm, so that the ligament is at least as long as the width of the specimen.

The average R-curves for the eight series of tests described in Table 5.1 are shown in Fig. 5.4. Two definitions of the initiation of crack propagation are used: the loss of linearity of the load-displacement curve (NL) and the visual observation of crack increment (vis). The distinction is essential in the analysis of intralaminar fracture, since the ERR increases quickly in the first millimeters of propagation. The visual initiation occurs slightly later than the loss of linearity, leading in average to 57% higher ERR values. After five millimeters of propagation the ERR is 2.6 ($t=0.150$ mm, $h=10$ mm) to 4.1 ($t=0.030$ mm, $h=6$ mm) times higher than the initiation ERR $G_{I,i,NL}$. For $t=0.075$ and 0.150 mm, the ERR values increase faster in the thin specimens (DCB $h=6$ mm) than in the thicker specimens (DCB $h=10$ mm, CT). Similarly, the ERR increase rate in the early crack propagation is higher in the thin-ply ($t=0.030$ mm) than in the thick-ply ($t=0.150$ mm) laminate, which denotes a more localized and dense bridging zone in thin-ply laminates than in their thicker counterparts.

The average ERR at crack initiation in the eight series of tests is $G_{I,i,NL} = 139 \pm 27 \text{ J/m}^2$. The values are slightly higher in the thin-ply specimens ($t=0.030$ mm) than in the two other ply thicknesses. This difference is attributed to the microstructure homogeneity and to the uncertainty associated with a precise detection of the crack initiation event. The CT specimens give NL initiation ERR values in good agreement with the values measured on DCB specimens, in particular for the $t=0.030$ mm specimens ($G_{I,i,NL} = 178 \text{ J/m}^2$). The value obtained in the $t=0.075$ CT specimens ($G_{I,i,NL} = 98 \text{ J/m}^2$) is slightly lower than the corresponding values in DCB specimens.

The steady-state ERR is reached at approximately 40% longer crack length increments for thick DCB specimens ($h=10$ mm) compared to thin ones ($h=6$ mm). For instance, in $t=0.075$ mm specimens steady-state propagation is reached at approximately 65 mm in $h=10$ mm specimens and 45 mm in $h=6$ mm specimens. In contrast, the maximal crack length extension achieved in CT specimens is limited to 17 mm by the geometry of the specimens. Thus, steady-state crack growth cannot be reached in this test configuration. Each R-curve associated with the DCB specimens can be considered as converged. On the whole range considered as steady-state, which represents at least 40 mm of propagation, the average plateau values are within the experimental scatter of the respective R-curves. As aforementioned, the J-

integral based R-curves are also computed for a majority of the specimens. The values are in good agreement with the ERR values obtained by the compliance calibration method (Table 5.2). This observation further validates the hypothesis of linearity.

While the ERR at initiation is relatively constant with the ply thickness and specimen configuration, the steady-state ERR is influenced by the ply and specimen thicknesses. The plateau level is 23% lower in the $t=0.030$ mm specimens in comparison with the standard $t=0.150$ mm ply specimens. The ERR in thick specimens ($h=10$ mm) are in average 12% higher than in thin specimens ($h=6$ mm). The steady state ERR values are 5.0 ($t=0.030$ mm, $h=6$ mm) to 9.4 times ($t=0.150$ mm, $h=10$ mm) higher than the NL initiation values. To summarize the effects of ply thickness and specimen thickness, the steady-state ERR is fitted by a linear model:

$$G_{I,tot} = 572 + 317 \cdot \bar{t} + 286 \cdot \bar{h} \quad \text{J/m}^2 \quad (5.1)$$

where \bar{t} is the ply thickness normalized by 0.150 mm and \bar{h} the specimen thickness normalized by 10 mm. As shown in Fig. 5.5, for a given specimen thickness, the steady-state ERR scales almost linearly with the ply thickness, on the range of observations. However, it should be noted that in intralaminar fracture, the ply thickness does not affect the bridging contribution and steady-state ERR as much as in interlaminar fracture. The two fracture modes are compared in more details in chapter 6.

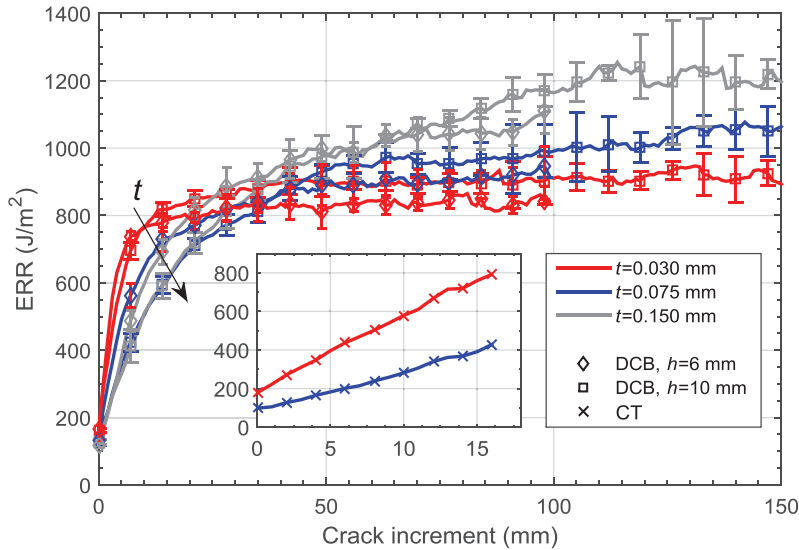


Fig. 5.4: Average R-curves for different ply thicknesses (color) and different specimen configurations (symbol). The insert shows the R-curve for the CT specimens.

5.2 Mechanistic investigations

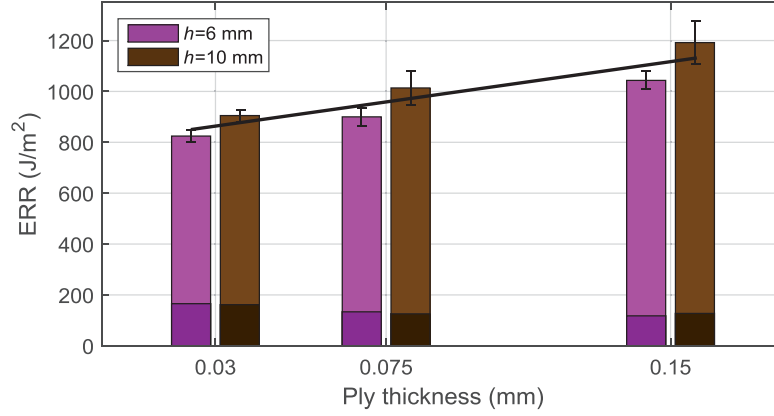


Fig. 5.5: ERR at crack initiation (dark colors) and steady-state propagation (light color).

Table 5.2: ERR computed with compliance calibration and J-integral for initiation by loss of linearity ($G_{I,i,NL}$), visual initiation ($G_{I,i,vis}$ and $J_{I,i,vis}$) and steady-state ($G_{I,ss}$ and $J_{I,ss}$).

			Compliance calibration			J-integral	
t (mm)	h (mm)		$G_{I,i,NL}$ (J/m2)	$G_{I,i,vis}$ (J/m2)	$G_{I,ss}$ (J/m2)	$J_{I,i,vis}$ (J/m2)	$J_{I,ss}$ (J/m2)
DCB	0.030	6	166 ± 5	301 ± 34	825 ± 24	316 ± 31	843 ± 20
DCB	0.030	10	162 ± 7	288 ± 15	905 ± 24	N/A	N/A
DCB	0.075	6	134 ± 5	225 ± 28	900 ± 36	246 ± 31	913 ± 48
DCB	0.075	10	126 ± 10	184 ± 16	1014 ± 67	204 ± 14	1025 ± 109
DCB	0.150	6	118 ± 6	166 ± 21	1043 ± 35	189 ± 20	1043 ± 41
DCB	0.150	10	127 ± 8	163 ± 33	1192 ± 84	N/A	N/A

5.2 Mechanistic investigations

Similarly as in interlaminar fracture, fiber bridging is the dominant toughening mechanism responsible for the strong R-curve behavior observed in intralaminar fracture. While the ERR at crack initiation is practically independent of ply and specimen thickness, differences are measured at subsequent crack growths. The side views of the DCB specimens shown in Fig. 5.6 are taken at the end of the experiments. They indicate a decreasing amount of bridging fibers with decreasing ply thickness. In the thin-ply specimen ($t=0.030$ mm), intact bridging fibers are visible only on the first 40 mm from the crack tip and it is not possible to detect large

bundles of fibers. On the contrary, fiber bridging develops on more than 100 mm in the $t=0.075$ and 0.150 mm specimens. For these ply thicknesses, the diameter of the largest bundles is of the same magnitude as the ply thickness.

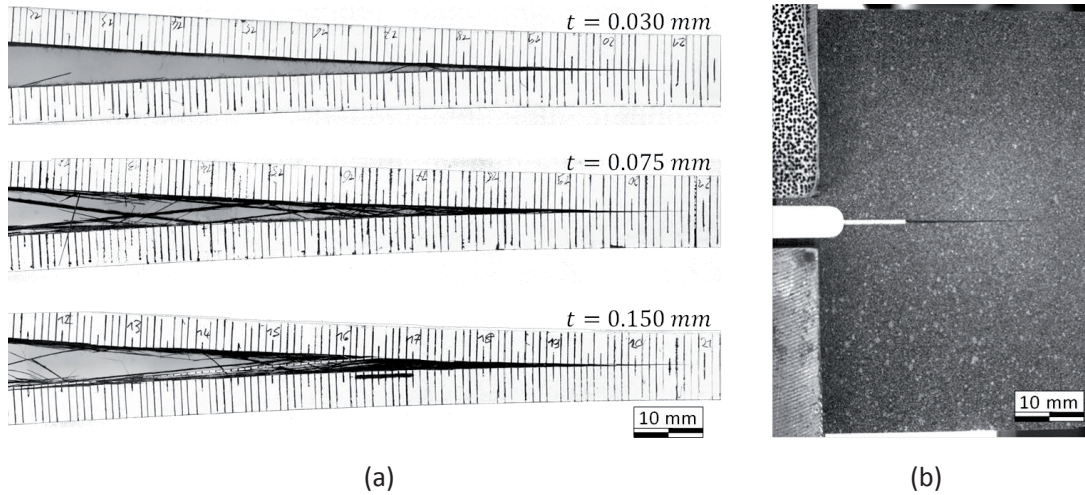


Fig. 5.6: Side views of (a) DCB specimens showing less fiber bridging with decreasing ply thickness ($h=4\text{mm}$) and (b) a CT specimen.

5.2.1 Microstructure analysis

The morphology of the microstructure has an important influence on the development of large bundles of fibers. Therefore, transverse sections of the specimens with the three different ply thicknesses are prepared as explained in section 3.2 in order to analyze the morphology of the bulk composite microstructure, of the crack surface and of the bridging ligaments. Fig. 5.7 shows a representative cross section for each of the ply thicknesses. Even if the laminate layers are not clearly separated from each other's, it is possible to discern their orientation which is rotated by 90° with respect to the crack plane. In the thin-ply laminate ($t=0.030$ mm), the fibers are dispersed rather uniformly along the ply width and thickness. Thus, the microstructure is well homogenized. On the contrary, in the thicker ply laminates, a large amount of fiber-rich and matrix-rich regions can be observed. As explained in section 4.3.1, the heterogeneity of the microstructure locally increases the stress level, in particular in the fiber-rich regions, which eventually promotes crack growth in different planes. Such a waviness of the initiation of the crack front along the specimen width is an important cause for the creation and development of large bundles of bridging fibers. Such bundles are visible on the side views of the thick-ply laminates but are absent in thin-ply laminate. Based on past observations and

literature, the large bundles of fibers which require long distance to fully develop are assumed to be the main source of the ply thickness effect. Indeed, the R-curves for the different ply thicknesses diverge only at large crack increment, when the large bundle of fibers develops. This hypothesis is verified hereafter by analyzing the morphology of the bridging ligaments.

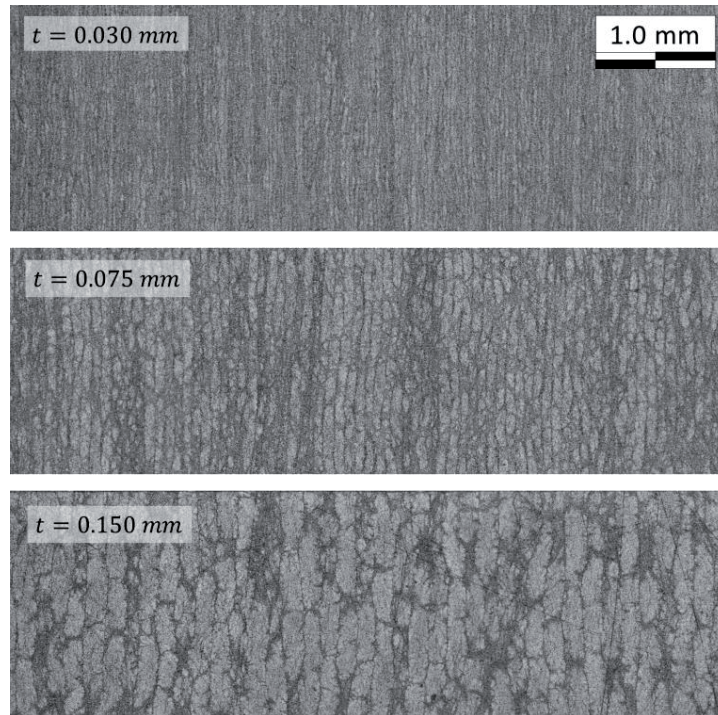


Fig. 5.7: Representative transverse sections for the three ply thicknesses. Please note that the crack plane is horizontal on these images.

5.2.2 Fiber bridging characterization

The bridging fibers and bundles which are responsible for the rising part of the R-curves are studied following the same procedure as for the interlaminar fracture (section 4.3.2). Transverse sections taken at different distances from the crack tip are processed with a semi-automated procedure based on thresholding techniques to extract the crack profile along the width of the specimen and isolate the bridging fibers and bundles (Fig. 5.8). The picture shown in Fig. 5.8 is approximately 9000 pixels in width with a pixel size of only ~ 0.55 microns, so that the resolution is sufficient to distinguish the carbon fibers.

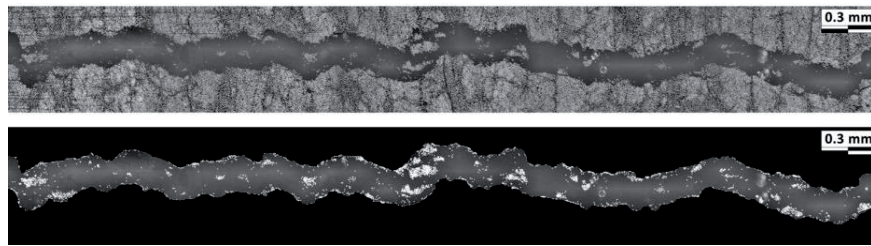


Fig. 5.8: Crack profile and bridging fibers / bundles.

The connected white surfaces representing bridging fiber or bundles are divided by the area of a single fiber to estimate the number of bridging fibers in each individual bundle and then in the whole specimen. Fig. 5.9 summarizes the amount of bridging fibers per millimeter of crack width in the most populated cross section of each ply thickness. A distinction is made between the isolated fibers and fibers clustered in bundles of at least 10 fibers. While the amount of isolated fibers decreases slightly with decreasing ply thickness, the amount of clustered fibers drops significantly. The clustered fibers represent 70% of the bridging fibers in the thick-ply laminate ($t=0.150$ mm) and only 24% in the thin-ply laminate. The large bundles of fibers require long distance to fully develop. Therefore, their presence in the thick-ply specimens explains the large crack increments required before reaching steady-state propagation. In thin-ply, since the amount and size of the bundles are small, the convergence to steady-state propagation is reached earlier, which explains the steep slope of their R-curve.

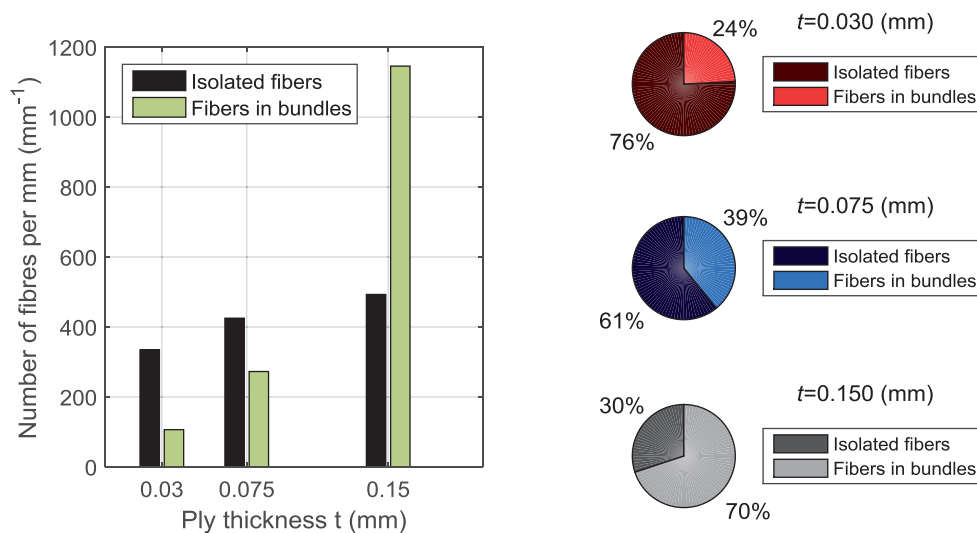


Fig. 5.9: Number of isolated bridging fibers and fibers clustered in bundles per millimeters of crack width.

5.3 Numerical modeling

5.3.1 Identification of bridging tractions

To simulate the intralaminar fracture in the CFRP laminate, the traction-separation relations associated with fiber bridging are required. Therefore, the identification method explained in section 3.3.1.2 is applied on the average R-curves of the DCB specimens. Note that the identification method cannot be applied to the CT specimens since steady-state propagation is not reached, which is one of the requirements of the method.

The identified relations are plotted in Fig. 5.10 and the corresponding identified parameters summarized in Table 5.3. Each of the curves are highly non-linear, so that σ_{\max} and δ_{\max} are reached almost tangentially when the COD and the traction tend respectively to zero. This non linearity is expected since the ERR increases much faster in the first millimeters of fracture than in the subsequent growths. The ply thickness effect is reflected in changes of the bridging parameters (Table 5.3). By decreasing the ply thickness t ,

- σ_{\max} increases significantly because of the very dense bridging zone that develops in thinner plies, which might be related to the reduced microstructure heterogeneity;
- $\hat{\gamma}$ increases because of the larger growth rate of the R-curve;
- δ_{\max} decreases because it is directly related to the bridging length z_{\max} , which is much smaller in the thin-ply specimens.

Interestingly, for a given ply thickness, the maximal opening values δ_{\max} are of the same magnitude in intra- and inter-laminar fracture, but σ_{\max} is much larger in intra- than in inter-laminar fracture. Since the maximal traction σ_{\max} reflects the slope of the R-curve at crack initiation, it was indeed expected to obtain larger values in intra- than in inter-laminar fracture.

5. Intralaminar fracture

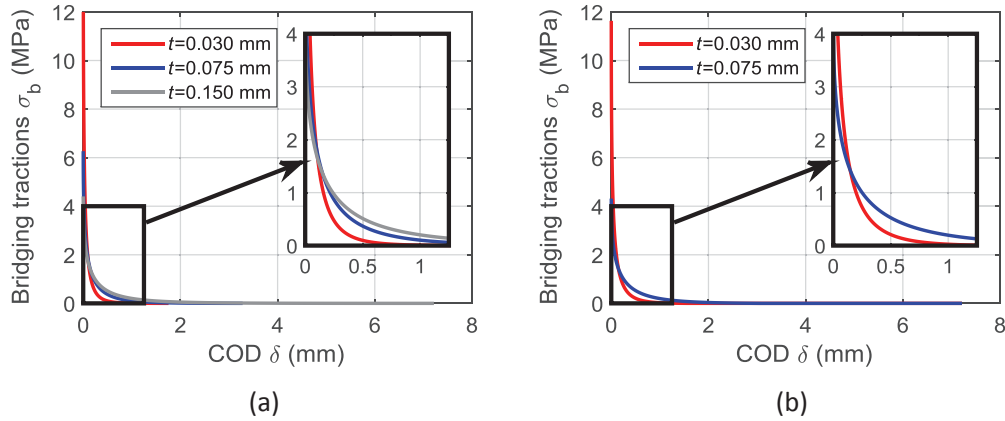


Fig. 5.10: Traction-separation relations as a function of ply thickness t for (a) $h=6$ and (b) $h=10$ mm.

Table 5.3: Identified fiber bridging parameters for different ply and specimen thicknesses.

h (mm)	t (mm)	σ_{\max} (MPa)	$\hat{\gamma}$ (mm ^{-1/2})	δ_{\max} (mm)
6	0.030	16.66	6.16	1.72
6	0.075	6.27	3.30	3.25
6	0.150	4.13	2.59	7.18
10	0.030	11.63	4.51	1.57
10	0.075	4.31	2.24	3.06

Since the energy associated with fiber bridging is approximately 2.5 times higher in intra- than in inter-laminar fracture and the maximal tractions are much higher, the R-curve based identification method (section 3.3.1.2) is compared with the strain-based method (section 3.3.1.1) for verification. An optical fiber is glued on the surface of a $t=0.150$ mm, $h=6$ mm specimen with a liquid cyanoacrylate Loctite® 401 in order to obtain the axial strain profile. Both identification methods are in very good agreement in terms of traction-separation profile (Fig. 5.11a). While the R-curve based identification method slightly underestimates the strain level close to the crack tip (by approximately 7%), it provides a slightly better prediction of the load-displacement response than the strain-based identification method (Fig. 5.11 b-c). Finally, the crack advance as a function of the applied displacement corresponds very well to the experimental data (Fig. 5.11d). Therefore, the R-curve based identification

method is assumed to be validated also for intralaminar fracture where fiber bridging is more intense than in interlaminar fracture.

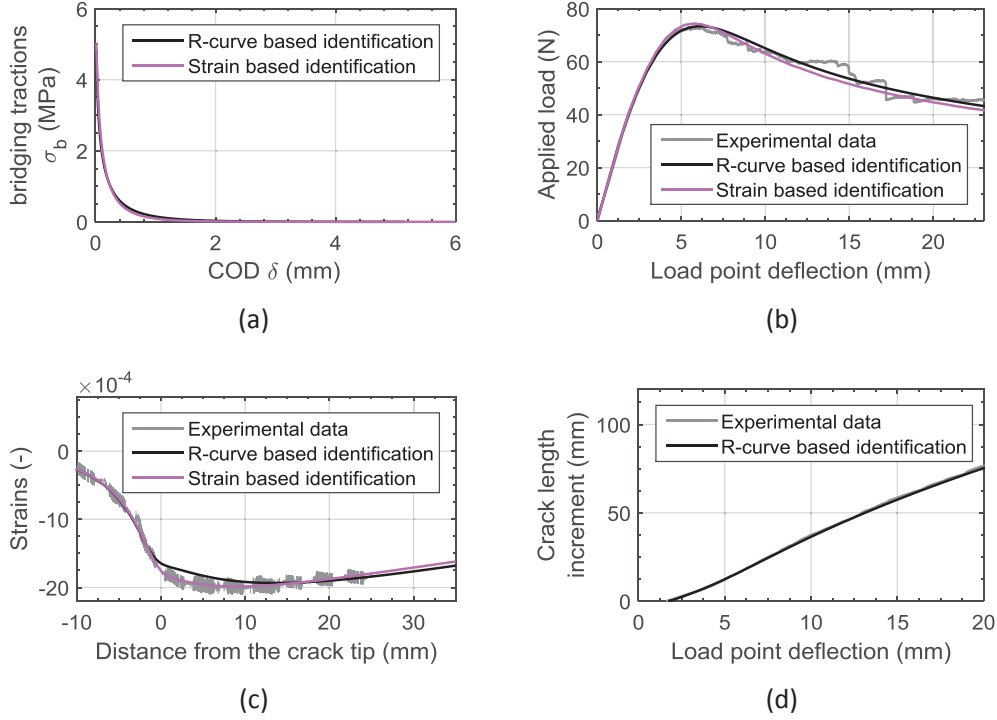


Fig. 5.11: (a) Traction-separation relations obtained with both identification methods; (b) Load-displacement curves, (c) strain profiles and (d) crack length increments obtained experimentally and numerically.

5.3.2 Cohesive elements simulations

The identified traction-separation relations are implemented in cohesive relations following the procedure explained in section 3.3.2. A triangular relation represents the matrix cracking and damage mechanisms in the zone ahead of the crack tip, with an area equal to the ERR at crack initiation $G_{I,i}$. The critical stress σ_c is set to the transverse tensile strength (23 MPa for each specimen [3]). Similarly as explained in section 4.4.1.2 and schematized in Fig. 4.16, the cohesive law is split into two relations, one for the matrix cracking and one for the fiber bridging, to avoid truncation issues in Abaqus. Both relations are implemented in two superimposed layers of linear cohesive elements (COH2D4). The cohesive relations are introduced in tabular form with 300 entries for the matrix cracking and at least 500 entries for the fiber bridging profile. The DCB arms are modeled in 2D plane strain condition with approximately 50'000 quadratic elements (CPE8R).

The numerical simulations reproduce very well the experimental load-displacement curves obtained on the DCB specimens, as shown in Fig. 5.12. The agreement is excellent not only in the steady-state propagation, which is mainly governed by the steady-state ERR, but also in the transient part where fiber bridging develops. Therefore, the cohesive model predicts very well the entire intralaminar fracture, including the peak load level.

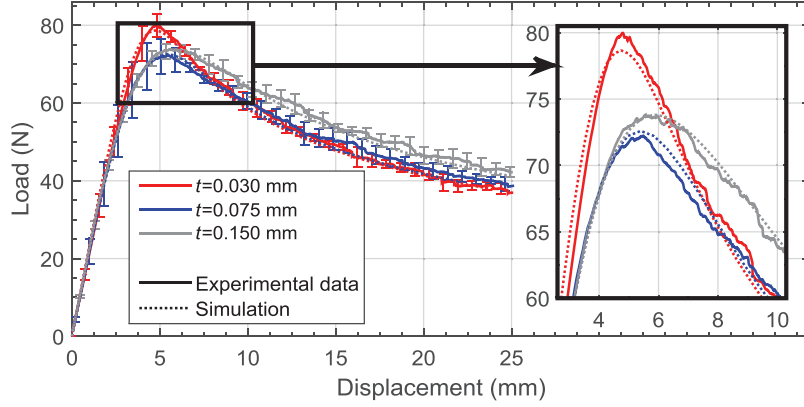


Fig. 5.12: Experimental and simulated load-displacement curves for DCB specimens with different ply thicknesses.

The bridging traction cannot be identified on the CT specimens using the R-curve based identification method, because the maximal crack length increment is not large enough to reach steady-state propagation. While the DCB specimens deform mostly in bending and have a non-linear COD profile with crack length, the CT specimens are shear dominated and have an almost linear COD profile. Despite these fundamental differences, the bridging traction-separation relations identified on the DCB specimens are used to predict the intralaminar fracture of the CT specimens. Indeed, the maximal stress σ_{\max} depends on the local microstructure and is independent from the far field loading [29], so that its value for the CT specimens should be the same as the corresponding values in DCB specimens. Moreover, the maximal COD at the crack starter $\bar{\delta}$ reached in the CT specimens, $\bar{\delta} = 0.22$ ($t=0.030$ mm) and $\bar{\delta} = 0.17$ mm ($t=0.075$ mm), are much smaller than the identified COD at the end of the fully developed bridging zone $\delta_{\max} = 1.57$ and 3.06 mm, respectively. Therefore, only a small part of the traction-separation relation is active on the fracture of the CT specimens. On so small maximal openings, the proposed relation works well, but other nonlinear decay formulations could also give good predictions.

As shown in Fig. 5.13, the traction-separation relation identified on the $h=6$ and 10 mm thick DCB specimens predict accurately the load-displacement curves obtained experimentally with the CT specimens. In particular, the peak load is very well predicted by the relations identified on the $h=10$ mm DCB specimens: only 1.0% ($t=0.030$ mm) and 0.7% ($t=0.075$ mm) relative error. Overall, the prediction is slightly better with the relations identified on the $h=10$ mm than on the $h=6$ mm specimens. This observation indirectly suggests that the specimen thickness effect is close to saturation at $h=10$ mm thick specimens, so that the corresponding traction-separation relation can be used to adequately model the behavior of much thicker structures or specimens such as the CT configuration.

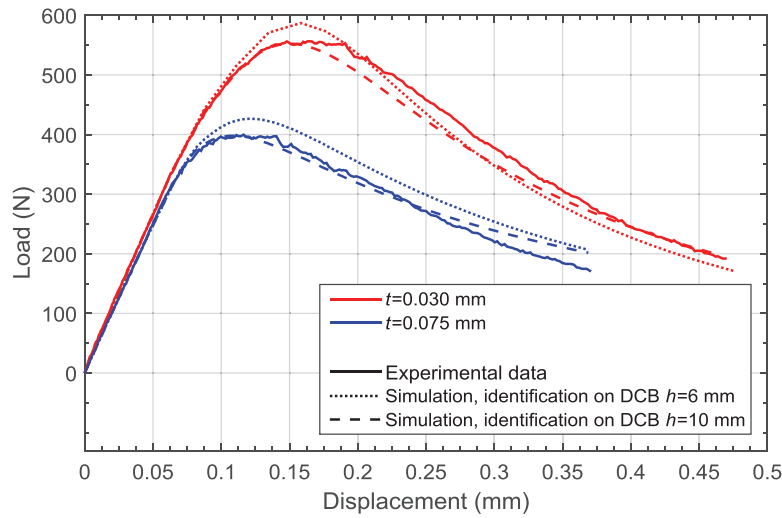


Fig. 5.13: Experimental and simulated load-displacement curves for CT specimens with different ply thicknesses.

5.4 Summary

The experiments show that the ply thickness significantly influences the mode I intralaminar fracture. The ERR at onset of crack propagation is practically independent of the ply thickness, even if a slightly higher ERR is obtained in the thin-ply specimens. The ERR increases rapidly in the 20 first millimeters of crack advance, with a resistance to fracture at least tripled after five millimeters. The growth rate is larger in thin-ply laminates but the steady-state ERR is reached at a shorter crack length and at a lower plateau level. Therefore, the resistance to fracture on the first 20 mm of crack advance is larger in thin-ply, which might be important since the cracks do not always have space to grow on larger distances, for instance in impact

damage or open-hole configuration. The steady-state ERR is 5 ($t=0.030$ mm, $h=6$ mm) to 9.4 ($t=0.150$ mm, $h=10$ mm) times higher than the initiation value. Thus, considering only the initiation ERR values would strongly underestimate the intralaminar resistance to fracture. The trends observed with the DCB specimens are confirmed by the experiments carried out with CT specimens: the ERR increases more slowly in thicker specimens. However, in CT specimens, the measurements are limited to less than 20 mm and the steady-state propagation is not reached.

The difference of R-curves with respect to the ply thickness is attributed to changes in fiber bridging behavior. The R-curves for different ply thicknesses diverge at large crack increment, where large bridging bundles develop in thicker-ply composites. The number of large bundles of bridging fibers scales with the ply thickness, leading to smaller ERR steady-state values in thin-ply. The development of such bundles is attributed to the amount of fiber- and matrix-rich regions which promote distributed damage nucleation and deviate the crack from its initial plane.

Cohesive element models are implemented to predict the intralaminar fracture in the DCB and CT specimens. The fiber bridging traction-separation relations are identified only on the DCB specimens because the CT specimens do not reach steady-state propagation. The identification method is reliable since it accurately predicts the load-displacement responses, in particular in the load peak region. The bridging tractions identified on the DCB specimens give also good prediction of the intralaminar fracture in the CT specimens. Thus, the traction-separation relations identified on relatively thick DCB specimens can reasonably be used to simulate the fracture of thick structures. Since in intralaminar fracture of thin-ply composites fiber bridging is more localized and intense on a small distance and does not extend as far as in thick-ply, σ_{\max} and $\hat{\gamma}$ are increased and δ_{\max} decreased with thinner plies.

Chapter 6

Comparison between inter- and intra-laminar fracture

The layers of the thin-ply laminate partially intermingle with each other during the curing cycle, rather than staying well separated as it usually is the case with standard composites. Therefore, in interlaminar fracture, the crack is likely to propagate within laminae, rather than at the interface between two plies. This behavior is furthermore enhanced by the presence of fiber-rich regions where damage nucleates due to the locally increased stress state. Therefore, although the pre-crack (PTFE film insert) is really between two plies at the crack starter, the crack likely migrates to within a ply right after the onset of propagation. In such a case, it becomes somehow questionable to still call this fracture mode “interlaminar”, but this term is kept for the sake of simplicity to describe the mode I fracture with loading perpendicular to the layers. However, even if the interlaminar cracks actually propagate within a lamina, results in chapters 4 and 5 show very different bridging behaviors and steady-state ERR values for interlaminar compared to intralaminar crack growth. Therefore, this chapter aims at comparing the R-curve behaviors in inter- and intra-laminar fracture and proposes an explanation for the different bridging behaviors.

6.1 Experimental data

Fig. 6.1 shows the R-curves for the interlaminar fracture in $h=4$ mm thick DCB specimens and the intralaminar fracture in $h=6$ mm thick specimens. The ERRs at initiation of crack propagation are nearly identical in inter- ($G_{I,i} = 140 \pm 11 \text{ J/m}^2$) and intra-laminar fracture ($G_{I,i} = 138.6 \pm 20 \text{ J/m}^2$). However, at subsequent crack growths, the behavior is totally different. In interlaminar fracture, the ERR increases slowly up to the steady-state propagation and the resistance to fracture is always smaller in the thin-ply when compared to the thick-ply laminate. In intralaminar fracture the ERR

6. Comparison between inter- and intra-laminar fracture

increases much faster on the first 20 mm of crack propagation. At this stage, the resistance to fracture is larger in the thin-ply laminate. At crack increments larger than 20 mm, the resistance to fracture becomes however smaller in the thin-ply laminate. Interestingly, regardless of the ply thickness, the steady-state propagations are reached approximately at the same crack length increments in the inter- and corresponding intra-laminar fracture. Moreover, the intralaminar R-curves from a crack increment of 20 mm and up are relatively similar to the interlaminar R-curves. It suggests that the fiber bridging mechanism on long crack length increment is similar in inter- and intra-laminar fracture and that a slightly different mechanism affects the first millimeters of intralaminar fracture.

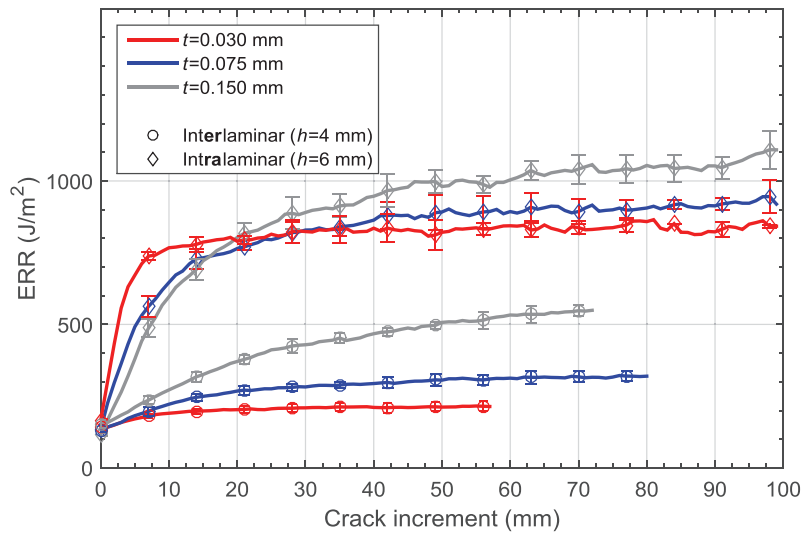


Fig. 6.1: Average R-curves for different ply thicknesses (color) in inter- and intra-laminar fracture (symbol).

Fig. 6.2 summarizes the initiation and steady-state ERR in inter- and intra-laminar fractures for 3 ply thicknesses and 2 specimen thicknesses. In both the inter- and intra-laminar fractures, the ply thickness has a comparatively larger influence on the steady-state ERR than the specimen thickness. The decrease in the ERR associated with fiber bridging between the thick-ply ($t=0.150$) and thin-ply ($t=0.030$) is of the same order of magnitude for each of the four configurations shown in Fig. 6.2 ($287 \pm 43 \text{ J/m}^2$). The difference between the inter- and intra-laminar fracture comes from the ERR associated with fiber bridging, which is surprisingly large in the thin-ply intralaminar fracture specimens when compared to the interlaminar fracture in thick-ply specimens. The ply thickness affects the bridging ERR to a similar absolute level in both the inter- and intra-laminar fractures. However, a very intense bridging ERR

6.1 Experimental data

develops over the first 20 millimeters of intralaminar fracture in each ply thickness, but is not present in interlaminar fracture, which constitutes the main difference between the two modes of fracture.

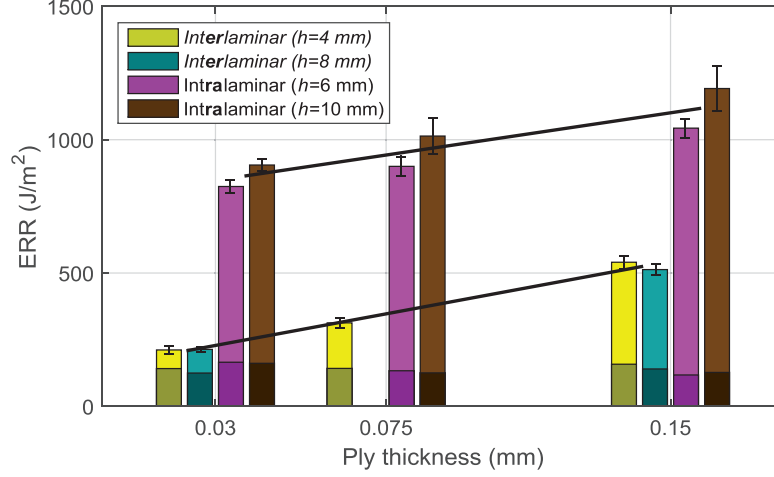


Fig. 6.2: ERR at crack initiation (dark colors) and steady-state (light colors) for inter- and intra-laminar fracture.

Fig. 6.3 presents the bridging traction-separation relations identified on the DCB specimens for the inter- ($h=4$ mm) and intra-laminar ($h=6$ mm) fracture tests. Since the ERR increasing rate at crack initiation is larger in intra- than in inter-laminar fracture, the maximal tractions σ_{\max} are much larger in the intra- than in the inter-laminar relations (Table 6.1). Interestingly, for each ply thickness, the CODs at the end of the fully developed bridging zone δ_{\max} are of comparable values in inter- and intra-laminar fracture. Moreover, the exponential decay parameter is smaller in the inter- than in intralaminar case, thus showing that the bridging tractions decay faster in the latter. Overall, the combination of those parameters leads to much higher bridging energies in intra- than in inter-laminar fracture at steady-state.

6. Comparison between inter- and intra-laminar fracture

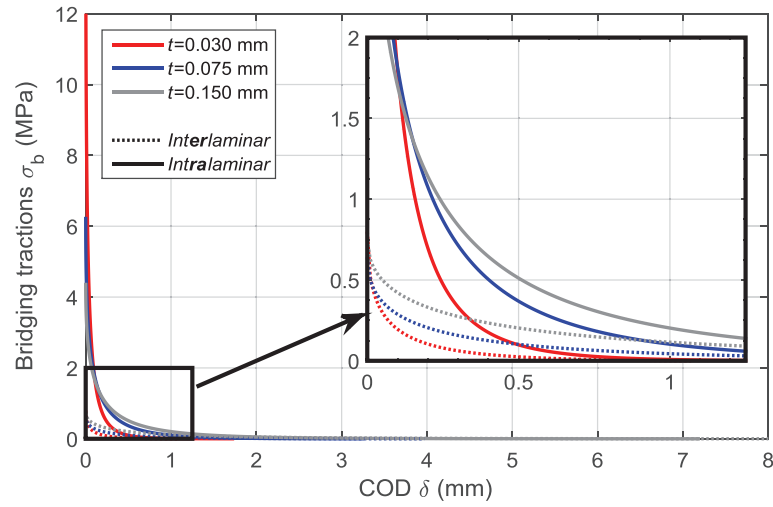


Fig. 6.3: Traction-separation relations as a function of ply thickness t for interlaminar fracture ($h=4$ mm) and intralaminar fracture ($h=6$ mm).

Table 6.1: Identified fiber bridging parameters for the different ply thicknesses in inter- and intra-laminar fracture.

Fracture mode	h (mm)	t (mm)	σ_{\max} (MPa)	$\hat{\gamma}$ (mm ^{-1/2})	δ_{\max} (mm)
Interlaminar	4	0.030	0.80	3.30	1.08
Interlaminar	4	0.075	0.64	1.99	3.97
Interlaminar	4	0.150	0.75	1.46	8.77
Intralaminar	6	0.030	16.66	6.16	1.72
Intralaminar	6	0.075	6.27	3.30	3.25
Intralaminar	6	0.150	4.13	2.59	7.18

In interlaminar fracture, the ERR contribution of bridging at steady-state $G_{I,b,ss}$, the maximal bridging traction σ_{\max} and the COD at the end of the fully developed bridging zone δ_{\max} vary linearly with the ply thickness on the range of observations, as shown in Fig. 6.4. Based on these three values, the exponential decay parameter $\hat{\gamma}$ can be back calculated. Therefore, such linear relations can be used to interpolate the bridging traction-separation relations for intermediate ply thicknesses based on data obtained experimentally for two extreme ply thicknesses. While in interlaminar fracture the maximal bridging traction σ_{\max} is constant with respect to the ply

thickness, in intralaminar fracture it varies nonlinearly with the ply thickness. Therefore, the accuracy of interpolated parameters for intermediate ply thicknesses is not ensured if only two extreme cases are identified experimentally.

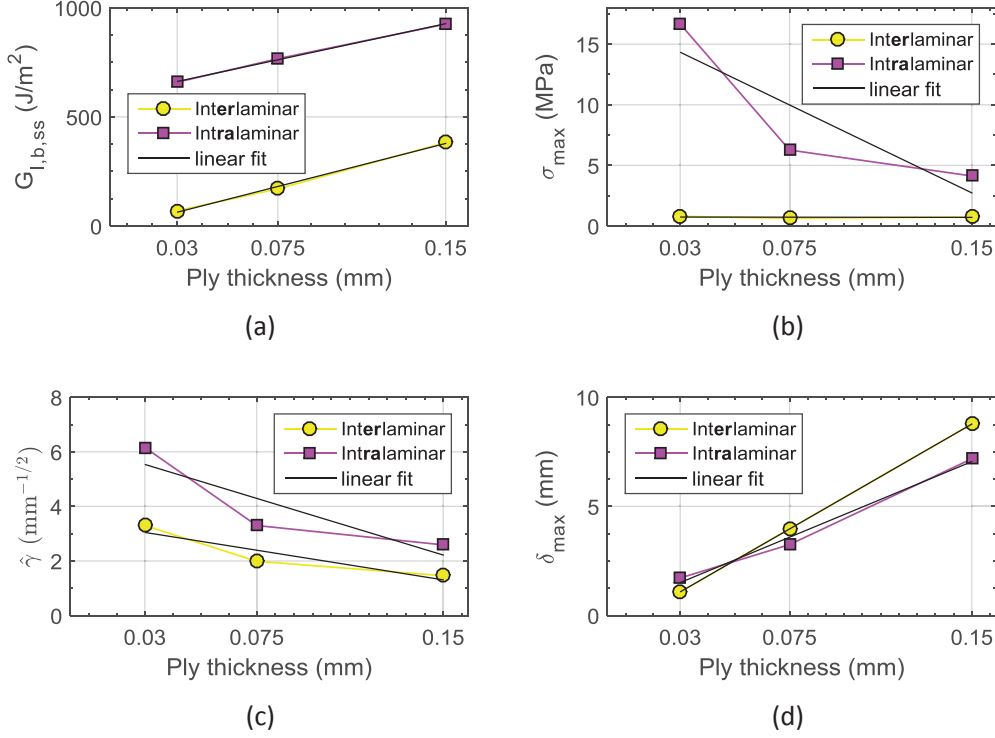


Fig. 6.4: For the inter- and intra-laminar fracture, linear scaling relations as a function of ply thickness for (a) bridging ERR at steady-state, (b) the maximal bridging traction, (c) the exponential decay parameter and (d) the COD at the end of the bridging zone.

6.2 Mechanistic investigations

As explained in sections 4.3 and 5.2 fiber bridging is the main toughening mechanism responsible for the increase in ERR when the crack propagates. Fig. 6.5 shows a comparison of representative cross sections in inter- and intra-laminar fracture for the thin ($t=0.030$ mm) and thick ($t=0.150$ mm) ply laminates. A first observation is that in interlaminar fracture of the thin-ply laminate, the crack profile is smooth and flat. Globally, for a given ply thickness, the crack profiles along the width of the specimens are more tortuous and rough in the intralaminar fracture tests. As this tortuosity is observed even very close to the crack tip, it proves that damage nucleates further away from the initial crack plane in intralaminar fracture, eventually leading to the creation of large bundles of bridging fibers.

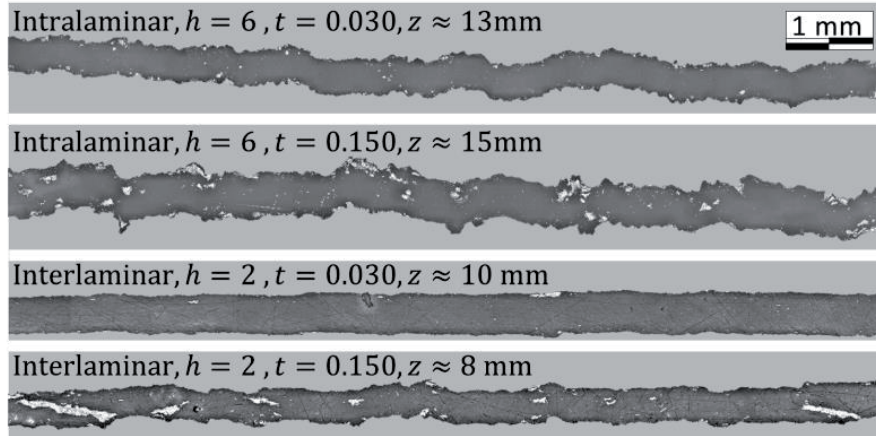


Fig. 6.5: Representative crack profiles and bridging fibers for different ply thicknesses t in specimens tested in inter- and intra-laminar fracture.

While in inter- and intra-laminar fracture of thin-ply laminates the number of bridging bundles is close to zero, in thick-ply laminates their amount is high. The large bridging bundles are relatively slender (with their main axis oriented parallel to the crack plane) in the interlaminar fracture specimens and almost circular in the intralaminar fracture specimens. This difference can be explained by the characteristic length scale of microstructure heterogeneity across the crack front which depends on the orientation of the plies. Indeed, the main fluctuation of local volume fraction happens between plies along the stacking direction with a period equal to the ply thickness. Moreover, it is known that micro-cracking initiates at fiber-rich regions. Thus, the characteristic length scale of the fluctuation of volume fraction should in principle control the spread of the damage initiation leading to bridging bundle formation. Because of the different ply orientation, the ply thickness could thus limit the width of the bundles in intralaminar fracture and the thickness dimension in interlaminar fracture, as schematized in Fig. 6.6. This hypothesis is confirmed by measuring the major and minor axes of the ellipses of equivalent second central moment for the ten largest bridging bundles. While in interlaminar fracture the major axis is almost 3.2 times larger than the minor axis, the aspect ratio is 2.0 in intralaminar fracture. Interestingly, the measured minor axis length of the bundles is clearly bounded by the thickness of the plies. In inter- and intra-laminar fracture, the equivalent diameters (or area) are of the same magnitude and scale almost linearly with the ply thickness (Fig. 6.7).

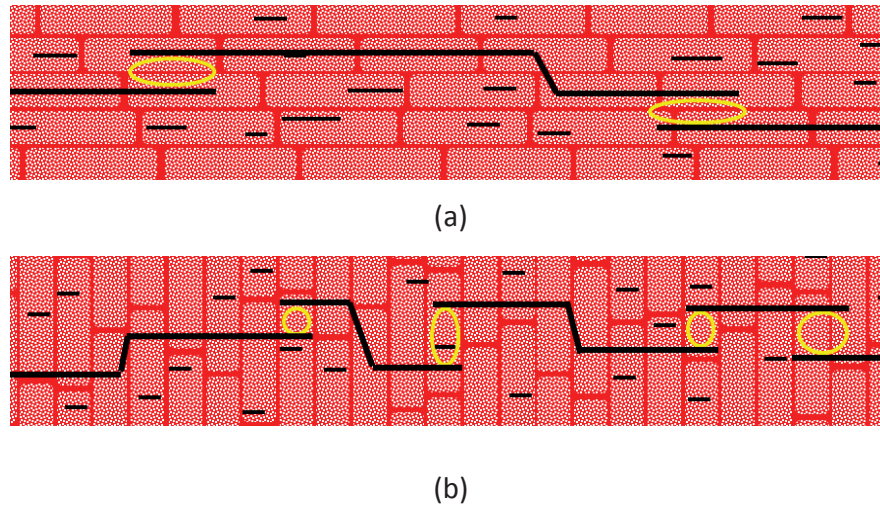


Fig. 6.6: Schematic view of the ply orientation, micro-cracking, crack tortuosity and bundle aspect ratio in (a) inter- and (b) intra-laminar fracture.

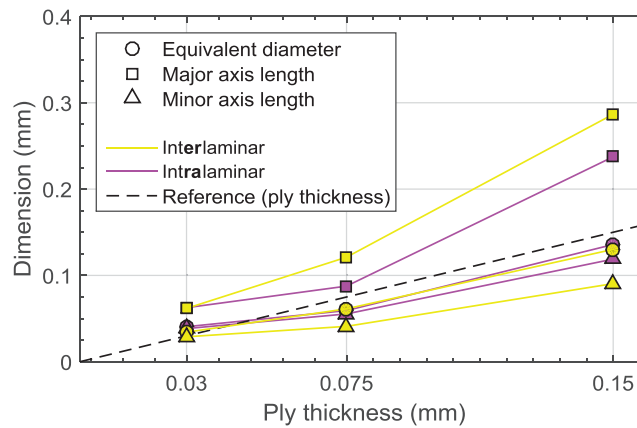


Fig. 6.7: Average equivalent diameter, major axis length and minor axis length for the ten largest bridging bundles in each ply thickness.

Fig. 6.8 (a) summarizes the amount of bridging fibers per millimeter of crack width. It distinguishes the amount of fibers counted in the cross sections close to crack tip (at approximately $z=3$ mm), from the fibers observed in cross sections close to the steady-state propagation. In each specimen, while the bridging fibers close to the crack tip are mainly isolated fibers, at larger distances from the crack tip a non-negligible amount of fibers is clustered in bundles of at least 10 fibers. The amount of fibers in bundles is more affected by the ply thickness than the amount of isolated fibers. This observation suggests that the large bundles of fibers are responsible for

6. Comparison between inter- and intra-laminar fracture

the ply thickness effect on the steady-state ERR in inter- and intra-laminar fracture as their size is directly limited by the ply thickness as discussed above.

For each ply thickness, regardless of the distance from the crack tip, the amount of bridging fibers is larger in the intra- than in inter-laminar fracture specimens. In both the inter- and intra-laminar fracture considered separately, the amount of bridging fibers scales with the ply thickness and consequently affects the steady-state ERR (Fig. 6.8 (b)). However, even if the amount of bridging fibers in intralaminar fracture of thin-ply ($t=0.030$ mm) is smaller than the corresponding value for the interlaminar fracture of thick-ply ($t=0.150$ mm), the steady-state ERR is higher in intra- than in inter-laminar fracture.

This observation shows that the amount of detected bridging fibers only partially explain the steady-state ERR level. This can be explained by the fact that the cross sections analysis is not able to distinguish broken bridging fibers from active ones and do not reflect the bridging fiber angle which could relate to the closing traction forces. Moreover, this analysis does not allow determining the longitudinal stresses carried by each of the bridging fibers and bundles, which appears to be different in both cases. Therefore, even though the number of bridging fibers is sufficient to explain the ply thickness effect in inter- and intra-laminar fractures separately, it fails to explain the difference of ERR level between inter- and intra-laminar fractures.

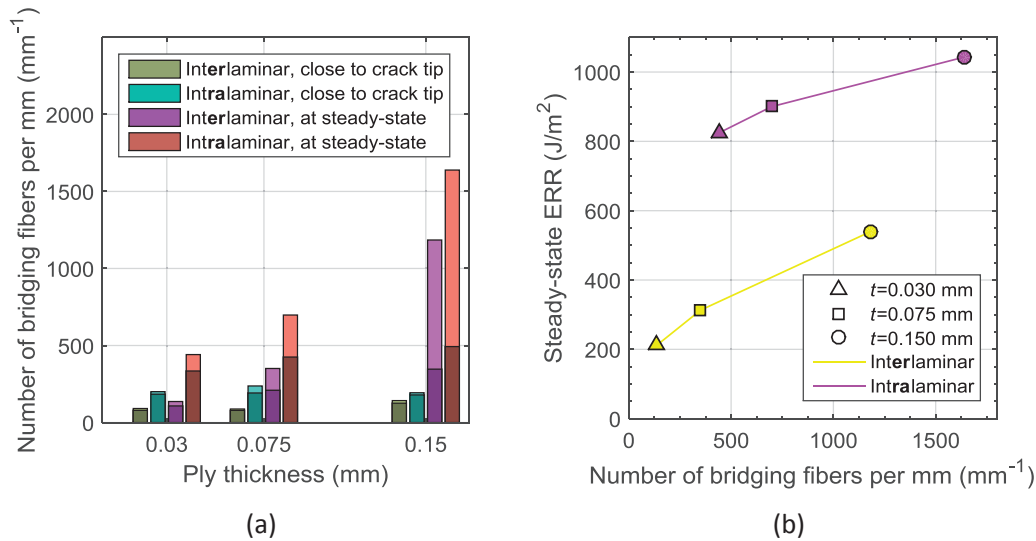


Fig. 6.8: (a) Number of isolated bridging fibers (dark colors) and bridging fibers in bundles (light colors); (b) Steady-state ERR as a function of number of bridging fibers.

Fig. 6.9 illustrates a possible explanation for the difference between inter- and intra-laminar fractures related to fiber waviness and misalignment. Indeed, in the stacking procedure by hand lay-up, it is likely to generate misalignments of up to 1° between the plies. In addition, the tow spreading process generates in-plane fiber waviness which might scale with the spreading ratio (initial diameter/final ply thickness). In the direction orthogonal to the plies, the thickness of the ply limits the fiber misalignment to approximately 0.04° for thick-ply laminate ($t=0.150$ mm) on 220 mm long specimens. Therefore, the probability that a fiber crosses the crack plane and becomes a bridging fiber is much higher in intra- than in inter-laminar fracture due to simple geometric effects.

Moreover, because of the limited fiber migration and waviness in the stacking direction, the bridging fibers are mostly aligned with the crack faces in interlaminar fracture. Thus, bridging ligaments in interlaminar fracture can easily debond from the matrix and propagate on long crack increments without being geometrically anchored by entanglement and thus avoid being overloaded and fractured prematurely (Fig. 6.9). Therefore, in interlaminar fracture, the stress in the bridging bundle is directly related to the interfacial toughness between the bundle and the bulk composite as shown in Spearing and Evans [106] and Sørensen et al. [107].

In intralaminar fracture, the potentially large fiber waviness and misalignment allow for a higher probability of geometric anchorage of fiber bundles in the surrounding composite due to their larger angle with respect to the crack faces. Thus, such fibers are pinned to the surface and thus have the potential to carry much higher forces than bridging fibers in interlaminar fracture. These highly loaded bridging fibers are deemed to be responsible for the fast and large ERR increase measured on the early crack propagation. However, due to the strong geometric anchorage, these fibers cannot debond and thus break in the region close to the crack tip, rendering their observation in transverse sections difficult. The other, better aligned, bridging fibers and bundles will similarly behave as in interlaminar fracture and debond over large distance as it is observed in the cross sections. This mechanism correlates very well with the ply thickness effect observed on the R-curves in inter- and intra-laminar fracture.

6. Comparison between inter- and intra-laminar fracture

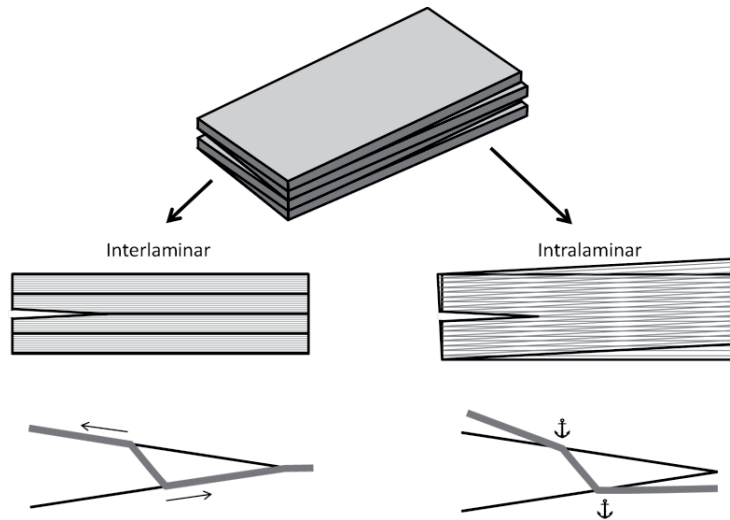


Fig. 6.9: Fiber misalignment in inter- and intra-laminar fracture.

Fig. 6.10 illustrates the average closing tractions per bridging fibers at approximately 3 mm from the crack tip. To obtain this graph, the CODs at 3 mm from the crack tip are extracted from the FE simulations for the inter- ($h=4$ mm) and intra-laminar ($h=6$ mm) fracture DCB specimens. The closing tractions are then extracted from the identified traction-separation profiles for the corresponding COD values. These closing tractions are finally divided by the number of bridging fibers observed on the cross sections to obtain the average tractions per fibers. Interestingly, the average traction is approximately 3.5 times larger in the intra- than in the inter-laminar fracture specimens. Therefore, this observation supports the aforementioned explanation that the bridging fibers are better anchored and carry higher forces in intra- than in inter-laminar fracture.

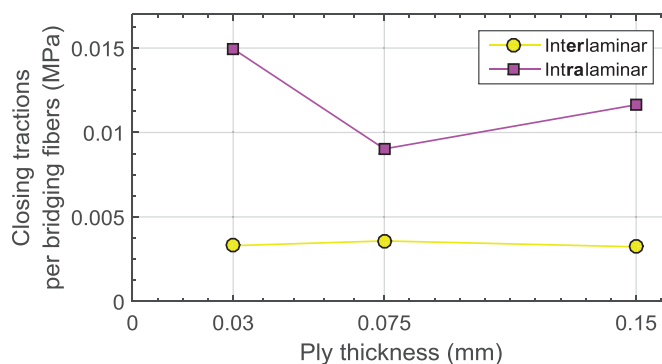


Fig. 6.10: Average closing tractions per bridging fibers in inter- and intra-laminar fracture ($z \approx 3$ mm).

Chapter 7

Translaminar fracture

Composite laminates are often used in structures for their outstanding in-plane strength properties. These structures are generally highly loaded in in-plane tension but are susceptible to include holes and cut outs which act as important stress concentrators and critical damage initiation points. Therefore, it is important to investigate the resistance to fracture under in-plane tension conditions. This fracture mode, which is called translaminar fracture, involves ultimately the failure of fibers under tension. Translaminar fracture cannot be tested on UD laminates, since the specimens would fail in shear, rather than propagate the crack across the fibers. Therefore, cross-ply (CP) and quasi-isotropic (QI) laminates are used in this study.

Since the in-plane strength properties of CP and QI laminates are highly influenced by the ply thickness, it might also be the case for the translaminar toughness property. Therefore, this chapter is dedicated to the characterization of the ply thickness effect on the ERR in monotonic translaminar fracture of CP and QI laminates. Firstly, experimental tests are carried out to quantify the ERR at initiation and subsequent crack growths. Secondly, mechanistic investigations are conducted to characterize the fracture surface of the broken specimens. Finally, cohesive element simulations are implemented to predict the global response of notched specimens under in-plane loading.

7.1 Experimental testing

7.1.1 Specimens and data reduction

The ply thickness effect on the mode I translaminar fracture is characterized experimentally by testing four different ply thicknesses: $t=0.030$, 0.075 , 0.100 and 0.150 mm. Two laminates lay-ups are considered. The CP laminate is used to study

7. Translaminar fracture

the basic dissipative mechanisms involved in the translaminar fracture such as fiber breakage, fiber/matrix debonding and fiber pull-out. This lay-up allows the quantification of the ERR associated with the 0° plies, since the ERR of the 90° plies is known from the intralaminar fracture study [84]. The QI laminate is used to study the fracture toughness of a laminate which is typically used in real structures.

The CT configuration is chosen for the translaminar fracture toughness measurements since it is the most widely used [85]. The design of the notch is adapted so that an extensometer can be used to measure the opening displacement of the crack faces at the distance corresponding to the load application point (Fig. 7.1). The initial crack lengths range from approximately 20 to 27.5 mm in order to evaluate the influence of the crack starter length on the ERR. All the other specimen dimensions are kept constant, so that the ply thickness is the only parameter that can be responsible for scaling trends of the ERR.

The specimens are machined from the CP and QI laminated plates by CNC machining using diamond coated tools. This process ensures a very good reproducibility in the specimen's dimensions. The width of the specimens that corresponds to the thickness of the plates reported in Table 3.1 varies also with a small scatter, thanks to the good compaction and precise thickness obtained with the production process explained in 3.1.1. The pre-crack is machined with a diamond wire saw of 0.13 mm in diameter. The radius of 0.065 mm at the tip of the pre-crack is much smaller than the limit of 0.25 mm, below which the initiation toughness is found independent of notch radius by Laffan et al. [91]. The exact dimensions of the specimens are reported in Table 7.1 (See Fig. 3.4 for the definition of the dimensions). In total, 28 specimens of seven ply thickness / lay-up configurations are tested. The specimens are prepared as explained in section 3.1.1, with a speckle pattern on one face and a ruler on a white background on the other face (Fig. 7.1).



Fig. 7.1: Compact tension configuration adapted for opening displacement measurement with an extensometer.

7.1 Experimental testing

Table 7.1: Dimensions of the specimens for translaminar fracture testing.

Denomination	Number of specimens (-)	g (g/m ²)	h (mm)	b (mm)	l (mm)	a_0 (mm)
CT_CP_30	4	30	60.0	9.86 ± 0.05	65.0	19.9, 22.3, 24.8, 27.3
CT_CP_75	4	75	60.0	9.44 ± 0.03	65.0	20.2, 22.7, 25.3, 27.8
CT_CP_100	4	100	59.9	9.53 ± 0.03	65.0	20.1, 22.6, 25.0, 27.5
CT_CP_150	4	150	60.2	9.66 ± 0.01	65.2	25.4, 25.6, 25.6, 25.8
CT_QI_30	4	30	60.1	9.93 ± 0.04	65.1	20.1, 22.5, 24.9, 27.4
CT_QI_75	4	75	60.2	9.24 ± 0.01	65.2	20.2, 22.7, 25.1, 27.6
CT_QI_150	4	150	60.1	8.99 ± 0.01	65.1	20.0, 22.5, 25.0, 27.4

The specimens are tested in mode I monotonic opening under a constant displacement rate of 0.5 mm/min using a MTS hydraulic machine equipped with a 100 kN load cell. The tests are immediately interrupted if compressive damage is visually detected on the ligament. In contrast to the DCB specimens, the CT specimens for translaminar fracture testing are very rigid in the direction of loading. As a consequence the displacement measured by the built-in machine LVDT does not accurately represent the displacement at the point of load application. Thus, an extensometer (MTS 632.03F-30) is used to measure the opening displacement of the specimen's crack faces close to the load application point. The difference between the measurements obtained from the LVDT and the extensometer allows comparing the rigidity of the set-up and the specimen. This comparison is necessary to verify that the rigidity of the machine and the set-up are sufficiently high in order to avoid dynamic effects due to the release of the strain energy stored in the machine itself when crack propagates in the specimens. After a nonlinear rigidity settlement due to contact in the bearing of the set-up and at the load application point, the rigidity of the machine and set up reaches approximately 20.8 kN/mm. The stiffness of the specimens with the shortest pre-cracks is 2.5 times lower (8.2 kN/mm). When the crack in the specimen becomes longer, the stiffness ratio increases, ensuring a better stability of the crack advance (see results in section 7.1.2).

The data reduction is done using the J-integral calculation based on DIC measurements of the displacement fields at the specimen's surface, as detailed in 3.1.3.3. In translaminar fracture testing, the crack propagates by successions of jumps. The J-integral values are therefore critical only at the moment just before the

crack jump. Therefore, even if the data reduction method does not require the load, displacement and crack length measurement to compute the fracture toughness, these values are monitored to determine the displacements (or time frames) when the loading becomes critical. In CP specimens the crack jumps can be observed visually on the surface of the specimen and correspond to sudden changes of specimen compliance. In QI specimens the surface observation does not provide reliable information about the crack advance, so that the critical displacements are determined from the jumps in the load-displacement response. The fracture toughness values are represented in the R-curves, where the x-axis refers to the crack length increment. Therefore it is necessary to define what is considered as the crack length.

The crack length is intrinsically difficult to define in CP or QI CT specimens. Indeed, due to the orientations of the different layers, the crack does not propagate similarly in each ply, so that there is not a single crack front. Moreover, the crack is not necessarily confined to a horizontal plane, especially in the $\pm 45^\circ$ plies where it propagates easily along the direction of the fibers. In such a case, the crack length could be assumed to be the orthogonal projection of the observed crack (visible damage) onto the horizontal plane defined by the crack starter. In addition, the visual observation of the crack on the surface of the specimen might not be representative of the crack length in the bulk. The change from plane stress conditions on the surface to plane strain at the crack tip in the center of the specimen might induce a curvature of the crack front [79]. More importantly, due to the large shear stress around the crack tip, localized delamination can occur between the most outer plies and the rest of the specimen, which would hide the real crack advance.

Another approach to determine the crack length is to compute it from the experimental compliance and a compliance calibration curve obtained by FE simulation, as detailed in [108]. However, this method assumes the linearity of the system, which might not be verified in CT tests. Moreover, in the computation of the compliance calibration curve, the FE model does not account for dissipative mechanism in the wake of the crack. This assumption is questionable, since fiber pull-out is known to dissipate more energy than fiber breakage [94].

Finally, a last approach consists in using the displacement fields on the surface of the specimens obtained by DIC. Since the CT specimen is a shear dominated loading configuration, the crack faces remain practically straight (linear COD profile). The vertical displacements along the initial upper and lower crack faces are tracked by DIC and fitted with a linear function. The intersection between these two linear

regressions is defined as the crack tip. This crack length measurement compares very well with the visual observation on the CP laminates.

In this work, the crack length measurement obtained by DIC is considered, since it is the most objective and reliable method. The accuracy of the crack length measurement is not as crucial as it would be if compliance calibration were used as a data reduction method. Indeed, the J-integral computation does not require the crack length measurement, which is only used for defining the x-axis of the R-curve.

Generally two important values are extracted from the R-curves: the ERR at crack initiation ($J_{I,i}$) and at steady-state ($J_{I,ss}$). However, it is difficult to define the initiation event in the CT specimens. Similarly as discussed earlier about the crack length, the onset of damage does not necessarily occur at the same time in plies of different orientations. Since the translaminar fracture tests aim to measure the ERR in the 0° plies, the first 0° fiber failure should be considered as the initiation event, rather than the onset of damage in the 90° plies. However, the detection of such an event is difficult. It can be obtained indirectly by tracking a change of compliance of the specimen. Indeed, since the rigidity in the 0° plies is approximately 30 times larger than in the 90° plies, damage in the 0° plies affects the compliance more considerably than damage in the 90° plies. Such an increase in the compliance is reflected by a sudden load drop, which can therefore be considered as the initiation event. Another approach consists in defining the initiation ERR as the value obtained at 0.5 mm of crack length increment. Such a crack length is small enough to be considered as the initiation value and occurs after the first load drop. The main advantage of this method is to be totally objective. Therefore, it is the definition considered hereafter for the ERR at crack initiation.

The steady-state ERR is not easy to define either, due to the relatively short crack increments achievable in the CT specimens. Indeed for some of the specimens, the tests are interrupted at relatively short crack length increments due to compressive damage on the ligament. In such a case, assuming a behavior similar to the other specimens and considering the trend of the data, a steady-state ERR value can be extrapolated. If a clear plateau is obtained on the R-curve, the steady-state ERR is computed as the average value on the range where steady-state is considered.

The fracture toughness computed by the J-integral method corresponds to the toughness of the laminate. In the CP specimens, since the toughness of the 90° plies is known from the intralaminar fracture tests (chapter 5), the toughness of the 0° plies can be obtained using the following rule of mixture [84, 109]:

$$G_I^0 = \frac{G_I^{lam} b^{lam} - G_I^{90} b^{90}}{b^0} \quad (7.1)$$

where, b^{lam} is the specimen width and b^0 and b^{90} are the total width of 0° and 90° plies within the laminate, respectively. This equation assumes that all the energy is dissipated by either the 0° or 90° plies, on a single crack plane parallel to the pre-crack, excluding the possible contribution of delamination. This assumption is reasonable since the inter- and intra-laminar fracture toughness are two orders of magnitude smaller than the translaminar fracture toughness. In QI specimens, the toughness of the $\pm 45^\circ$ plies cannot be directly distinguished from the contribution of the 0° plies. However, if the toughness of the 0° and 90° plies is known, for example from translaminar tests on CP specimens, the toughness of the $\pm 45^\circ$ plies can be estimated as [109]:

$$G_I^{\pm 45} = \frac{G_I^{lam} b^{lam} - G_I^0 b^0 - G_I^{90} b^{90}}{b^{\pm 45}} \quad (7.2)$$

where $b^{\pm 45}$ is the total width of $\pm 45^\circ$ plies within the laminate.

7.1.2 Ply thickness effect

Our test results show that the ply thickness strongly influences the global response of the CT specimens. Fig. 7.2 presents the load-displacement curves for CP specimens of four different ply thicknesses and QI specimens of three different ply thicknesses pre-cracked at approximately $a_0 = 25$ mm. The loading curves are not linear until the first load drop, especially for the CP specimens. In the most extreme case ($t=0.150$ mm), the secant stiffness at the first load drop is $\sim 16\%$ lower than the initial stiffness of the specimen. To investigate the causes of such a nonlinearity behavior, two loading-unloading cycles until a non-critical displacement of $\Delta = 1$ mm are carried out on a $t=0.150$ mm CP specimen (Fig. 7.3). After the second loading, a pause of 5 minutes corresponding to the time of a typical CT test is applied before unloading the specimen. This test indicates a visco-plastic behavior, with a residual displacement of 0.03 mm and maximal variations of the apparent stiffness of $\pm 7\%$ with respect to the secant stiffness. Verification on the numerical models detailed in section 7.3 shows that the in-plane shear stress limit at 0.2% offset (50.23 MPa) is locally exceeded in particular around the crack tip. Further considerations about the reduction of apparent shear modulus are discussed in section 7.3. The loading curves are more linear in the QI than in the CP specimens. Such a difference is explained by much higher resistance to shear in the QI laminate than in CP laminate due to the presence

7.1 Experimental testing

of the $\pm 45^\circ$ plies. The initial stiffness of the QI specimens is larger than for the CP specimens due to their much higher shear modulus.

The first load drop is considered when the load drops by more than 0.05 kN in 0.1 s (which is approximately 10 times the noise level on the linear loading part). Such a load drop reflects a significant change of specimen compliance and therefore most likely corresponds to the failure of 0° fibers. Interestingly, the first load drop occurs at a 33% lower load level in the $t=0.030$ mm than in the $t=0.150$ CP specimens, and 41% lower in the QI specimens. This change indicates qualitatively that much less energy is required to initiate the translaminar fracture in thin-ply.

The cracks propagate by successions of jumps. These jumps become generally smaller at larger crack length increment, indicating a more stable propagation. This behavior is a combined effect of the increase in the stiffness ratio between the machine and specimen, and the increase in the ERR with crack length due to the toughening mechanism acting in the wake of the crack.

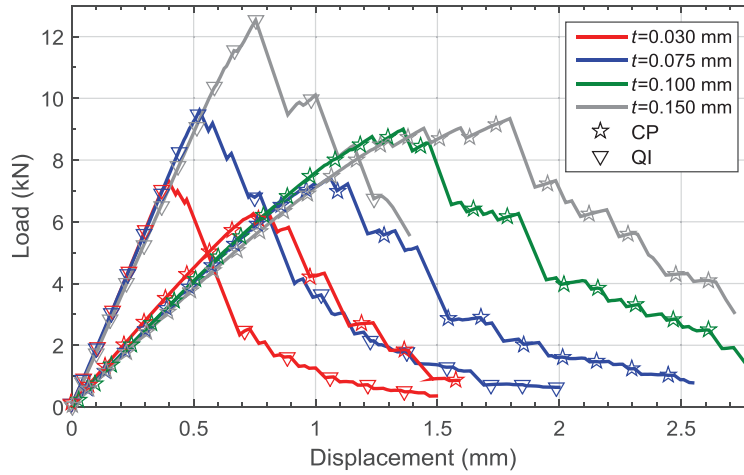


Fig. 7.2: Representative load-displacement curves as a function of the ply thickness in CP and QI specimens ($a_0 \approx 25$ mm).

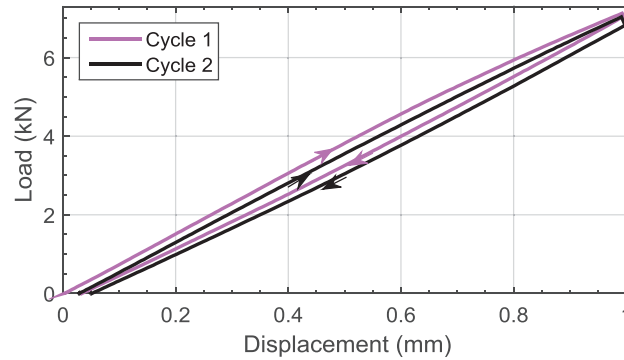


Fig. 7.3: Two loading-unloading cycles up to a noncritical displacement in a selected $t=0.150$ specimen.

The average R-curves for the seven series of tests described in Table 7.1 are shown in Fig. 7.4. A strong effect of ply thickness can be clearly observed in CP and QI specimens. As already mentioned in the analysis of the load-displacement curves, less energy is required to initiate the crack propagation in the thin-ply specimens. This observation is confirmed in the R-curves, since the initiation ERR scales remarkably linearly with the ply thickness. The initiation ERR, which is defined as the ERR at 0.5 mm of crack increment, is 70% lower in the thin-ply ($t=0.030$ mm) than in the thick-ply ($t=0.150$ mm) CP specimens and 72% lower in the corresponding QI specimens. The values obtained in the QI specimens are of similar magnitude as the corresponding values in CP specimens, except for the intermediate ply thickness ($t=0.075$ mm), where the QI value is 26% lower (Fig. 7.5).

At subsequent crack growths, the increase in the resistance to fracture also depends on the ply thickness. In the thin-ply laminate ($t=0.030$ mm), the ERR stays almost constant from the beginning, indicating the absence of toughening mechanisms in the wake of the crack. On the contrary, in the thick-ply laminate ($t=0.150$ mm), the ERR increases significantly. After a rapid rise on the first 2 mm of crack propagation, the ERR increases almost linearly with the crack advance. For this ply thickness, the R-curve does not completely reach steady-state, because of the relatively small maximal crack increment. The crack length increment necessary to converge to steady-state propagation is larger in the specimen having increasing resistance to fracture with crack advance. However, since the resistance to fracture is higher, the compressive load on the specimen ligament is also larger, leading to micro buckling, compression damage and a premature end of the test.

The steady-state ERR is 80% lower in the thin-ply ($t=0.030$ mm) than in the thick-ply ($t=0.150$ mm) CP specimens and 74% lower in the corresponding QI specimens.

7.1 Experimental testing

The values obtained in the QI specimens are ~25% lower than the corresponding values in CP specimens for $t=0.075$ and 0.150 mm and almost identical for $t=0.030$ mm. As shown in Fig. 7.5, the initiation and steady-state ERRs scale linearly with the ply thickness. This observation is particularly evident in the CP laminates where four different ply thicknesses are tested.

The observed decrease in the ERR with decreasing ply thickness confirms the trend observed by Teixeira et al. [95]. In their work, two ply thicknesses were tested for different grades of a thin-ply carbon / epoxy CP laminates. They obtained a significant increase in the ERR for both the initiation and propagation values with the increasing ply-block thickness. Our work is fully consistent with their conclusions. Moreover, by adding intermediate ply thicknesses, we show that the relation between ply thickness and ERR at initiation and subsequent propagation is linear. Furthermore, our work extent the observation of the ply thickness effect on the fracture toughness of QI laminates.

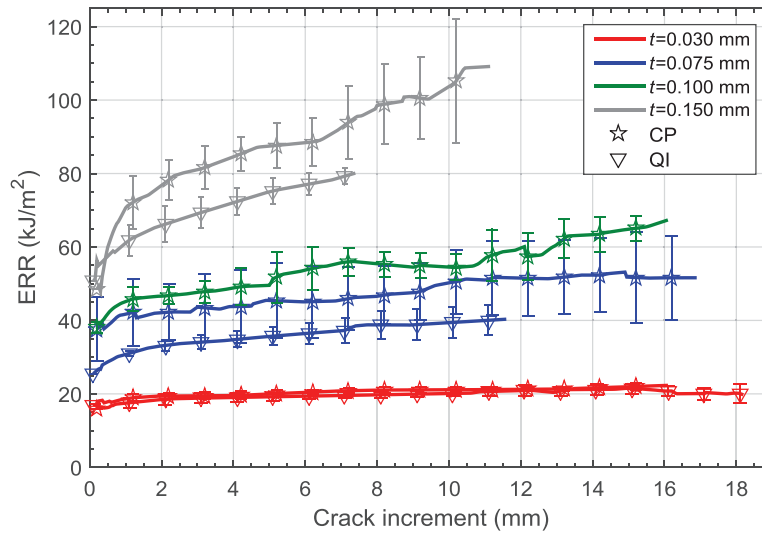


Fig. 7.4: Average R-curves for different ply thicknesses in CP and QI laminates.

7. Translaminar fracture

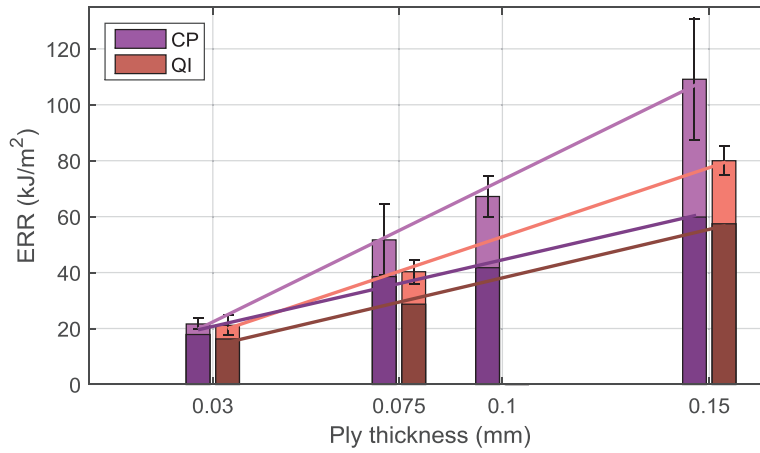


Fig. 7.5: ERR at crack initiation (dark colors) and “steady-state” propagation (light colors).

From the intra- and CP translaminar fracture tests and using eq. (7.1), the fracture toughness of the 0° plies can be computed. The toughness values at initiation and in propagation are shown in Table 7.2. Note that neglecting the toughness of the 90° plies which is much smaller than in the 0° plies in eq. (7.1) would induce an error of less than 2% on the toughness of the 0° plies.

Combining the results of the QI translaminar fracture tests with the toughness of the 0° plies calculated in Table 7.2 allows the computation of the toughness in the $\pm 45^\circ$ plies (eq. (7.2)). As shown in Table 7.3, the fracture toughness of the angled plies is significantly smaller than the value of the 0° plies. Part of this effect is explained by geometrical considerations. In the $\pm 45^\circ$ plies, the crack propagates by a succession of splitting along the fiber direction followed by fiber failure in the direction normal to the fibers, as schematized in Fig. 7.6. The length where fibers are broken in the $\pm 45^\circ$ plies is $\sin(45^\circ) = 1/\sqrt{2}$ times the crack length increment in the horizontal crack plane. The $\pm 45^\circ$ plies are also split on the same length, but this mechanism dissipates much less energy than fiber failure and pull-out. Moreover, the broken fibers are pulled out on a distance that also scales as $\sin(45^\circ) = 1/\sqrt{2}$ times the COD δ (Fig. 7.6). These simple geometric considerations alone could explain a reduction of toughness of the $\pm 45^\circ$ plies by at least a factor of two ($\sin^2(45^\circ) = 1/2$) with respect to the 0° plies, which is interestingly accurately verified for thin-ply. However, in thicker plies, this factor of two remains a lower bound as more complex changes in pullout mechanisms might develop. Overall, the translaminar toughness of $\pm 45^\circ$ plies lies in the bound of 25% to 50% of the 0° plies. As a coarse estimate, the rule of mixture could be used to extrapolate the translaminar fracture toughness to different

7.1 Experimental testing

multidirectional laminates. The following equation is proposed to compute the toughness of angled plies: $G_I^\theta = r \cdot \sin^2(\theta) \cdot G_I^0$. In this equation, θ is the relative angle of the ply with respect to the 90° ply and r is a reduction factor accounting for the interaction with the neighboring plies (based on results of Table 7.3, $r \approx 0.7$ for $\pm 45^\circ$ plies).

Table 7.2: Fracture toughness of the 0° plies.

t (mm)	b^0/b^{90} (%)	Initiation ($\Delta a = 0.5$ mm)			Propagation ($\Delta a = 11$ mm)		
		G_I^{lam} (kJ/m ²)	G_I^{90} (kJ/m ²)	G_I^0 (kJ/m ²)	G_I^{lam} (kJ/m ²)	G_I^{90} (kJ/m ²)	G_I^0 (kJ/m ²)
0.030	49.70	17.9	0.16	35.8	21.6	0.77	42.7
0.075	49.23	38.6	0.13	78.2	51.7	0.50	104.5
0.100	48.98	41.7	0.13 *	85.1	67.2	0.51 *	136.7
0.150	48.48	60.3	0.13	124.3	109.1	0.51	224.5

* Extrapolated value

Table 7.3: Fracture toughness of the $\pm 45^\circ$ plies.

t (mm)	Initiation ($\Delta a = 0.5$ mm)				Propagation ($\Delta a = 11$ mm)			
	G_I^{lam} (kJ/m ²)	G_I^{90} (kJ/m ²)	G_I^0 (kJ/m ²)	$G_I^{\pm 45}$ (kJ/m ²)	G_I^{lam} (kJ/m ²)	G_I^{90} (kJ/m ²)	G_I^0 (kJ/m ²)	$G_I^{\pm 45}$ (kJ/m ²)
0.030	16.3	0.16	35.8	14.6	21.1	0.77	42.7	20.5
0.075	28.7	0.13	78.2	18.2	40.3	0.50	104.5	28.1
0.150	57.5	0.13	124.3	52.7	90 *	0.51	224.5	67.5

* Extrapolated value

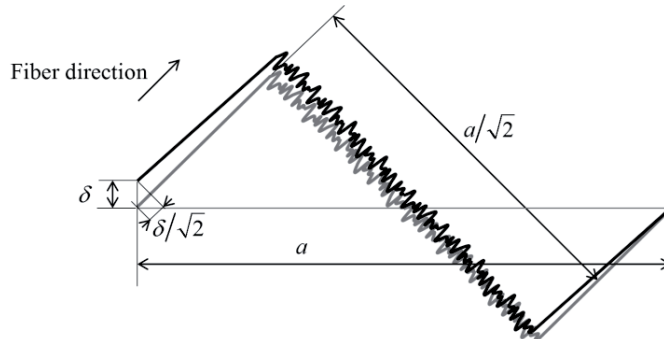


Fig. 7.6: Propagation of the crack in the $\pm 45^\circ$ plies by succession of splitting and fiber failure.

7.2 Mechanistic investigations

The fracture toughness is strongly affected by the ply thickness. Since the total thickness of 0° plies is the same in the specimens of each ply thickness, the same amount of fibers are broken to propagate the crack to a given extent. Therefore, the dissipated energy associated with fiber failure is expected to be independent of ply thickness. As a consequence, the difference of ERR with respect to ply thickness is caused by another dissipative mechanism. To try to understand the reasons of the ply thickness effect, the fracture surface of the specimens is analyzed.

7.2.1 Cross-ply (CP) specimens

A representative view of the fracture surface of the CP specimens for each of the four ply thicknesses is shown in Fig. 7.7 (a)-(d). For each image, the zone illustrates approximately 2.3 mm along the width and 5.5 mm along the crack advance direction. The same color scale represents the topography height in the four ply thicknesses. The images are obtained with A VHX-5000 Keyence optical microscope, at a magnification of 700x and with a vertical pitch of ~ 0.005 mm. Thanks to the stitching function and the depth from defocus technique, the topography of the surface can be obtained.

The practically flat 90° plies (orthogonal to the loading direction) can be easily distinguished from the relatively rough 0° plies in Fig. 7.7. The arrows indicate the double 90° ply at the mid-plane of each specimen. One can also clearly observe the crack starter on the bottom of each view. Interestingly, the fracture surfaces of the 90° plies do not always start from the same side of the pre-crack cut. Therefore, some of the 90° crack surface appears 0.130 mm higher than the others.

The 0° plies are much rougher than the 90° plies. Indeed, some 0° fibers do not break on the initial crack plane level. These fibers, or group of fibers, are debonded from the surrounding matrix and progressively pulled-out when the crack faces move away from each other. The pull-out mechanism dissipates energy due to the fiber / matrix debonding and the friction between the fibers and the matrix. Since the height of the pull-out fibers seems to vary significantly with ply thickness, this dissipative mechanism is deemed to be responsible for the ply thickness effect on the translaminar fracture toughness.

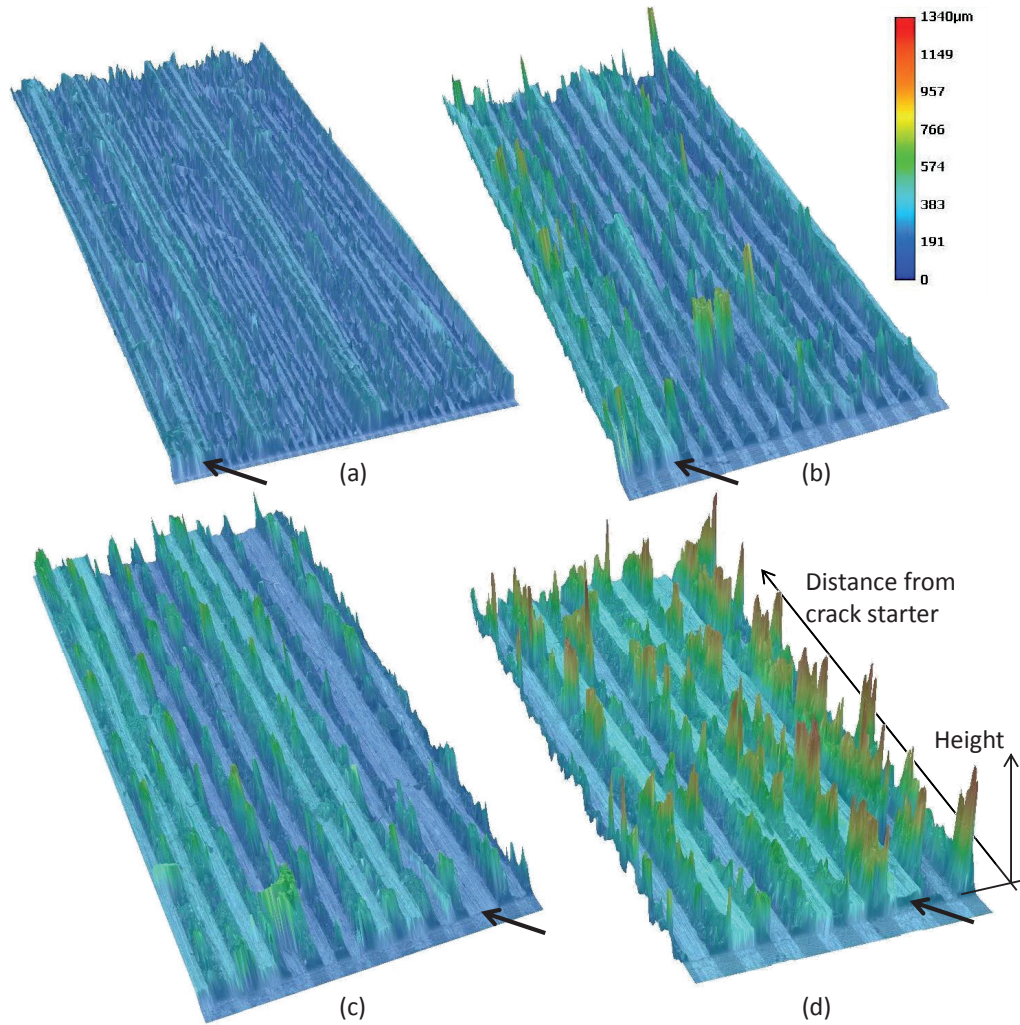


Fig. 7.7: Representative view of the fracture surface in the CT CP specimens with (a) $t=0.030$ mm, (b) $t=0.075$ mm, (c) $t=0.100$ mm and (d) $t=0.150$ mm. The arrow indicates the double 90° ply at the center of the specimens.

Crack surface profile in the 0° plies such as the ones represented in Fig. 7.8 are extracted from the topography images using the exporting toolbox of the Keyence microscope. The local variations of height in the profiles represent the pull-out fibers. While in the thin-ply specimen ($t=0.030$ mm) only few small pull-out are observed, in the thick-ply specimen ($t=0.150$ mm) more and higher pull-out are detected.

Interestingly, the fracture profiles appear relatively constant along the crack length increment. In particular, relatively high pull-out fibers are developed right after the crack tip. A constant average pull-out height along the crack propagation is fully consistent with shape of the R-curves shown in Fig. 7.4. Indeed, after the 0.5 first millimeters of crack propagation, the ERR increases almost linearly with the crack

length increment. Since $\sigma(\delta) = \frac{dJ}{d\delta}$ [72] and the COD vs distance from crack tip is practically linear, the slope of the R-curve would not be constant if the amount of closing tractions associated with fiber pull-out was changing along the crack extension. This observation clearly supports the modeling hypothesis proposed in section 3.3.3, where the pull-out mechanism is proposed to be modeled by a constant closing traction.

The fracture profiles along the crack growth direction, in the middle of the 0° plies, are extracted from the observations shown in Fig. 7.7. These profiles, for which representative examples are shown in Fig. 7.8, are analyzed by a wavelet decomposition for each specimens except the $t=0.030$ mm where too small pull-out fibers are observed. Using Matlab, the signal is decomposed with 14 levels of Haar wavelets that have respective width of 2^n ($n=1,\dots,14$) pixels. The level for which the root mean square of the detail coefficient is the highest corresponds to the characteristic length scale of the signal. Interestingly, the same characteristic size is found for the three ply thicknesses, corresponding to a typical pull-out bundle width in the direction of crack propagation of ~ 0.15 mm. This observation means that the frequency of pull-out development along the crack extension is of the same order of magnitude in each ply thickness. Therefore, the ply thickness does not affect considerably the amount of pull-out fiber bundles.

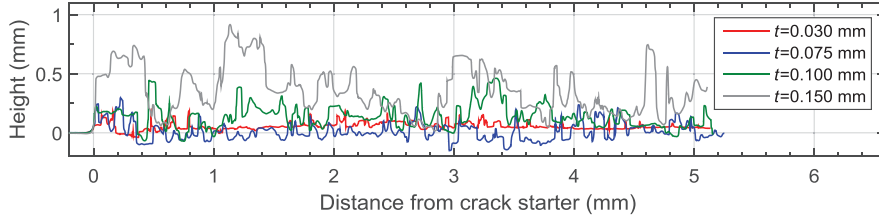


Fig. 7.8: Representative surface profile in 0° plies of CP CT specimens for different ply thicknesses.

In Fig. 7.8, the pull-out fibers appear significantly lower in the $t=0.030$ mm than in the $t=0.150$ mm specimens. To generalize this observation on more than one ply, the top and bottom profile envelopes are computed based on all the profiles of the 0° plies shown in Fig. 7.7. For each pixel along the crack extension direction, the maximal and minimal heights among the individual profiles are noted to define the top and bottom envelope profiles. For each of the ply thickness, the top and bottom envelope profiles let a zone of approximately 0.13 mm blank (Fig. 7.9). This zone corresponds to the height of the pre-crack cut. Since the 90° plies propagates at a height

corresponding to one of the sides of the cut, the top profile is obtained by pull-out observed in the vicinity of the “high” 90° profile and the bottom profile in the regions close to the “low” 0° plies.

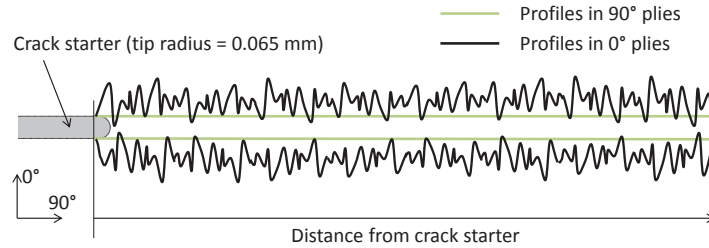


Fig. 7.9: Schematic of the crack starter and crack profiles in the 0° and 90° plies.

The histograms of the top and bottom envelope profiles are then computed and fitted by normal laws (Fig. 7.10 for the top profile). The mean, standard deviation and extreme values are reported in Table 7.4 for both the top and bottom envelope profiles. After the removal of the height of the pre-crack cut, the difference between the top and bottom profiles is a quantifier of the pull-out height. The difference between the mean values correlates with the ply thickness. The largest average pull-out height is measured in the thick-ply laminate, where the translaminar fracture ERR is the largest. The average pull-out height in the $t=0.075$ mm is almost as high as in the $t=0.100$ mm. However, the R-curve of the observed $t=0.075$ mm specimen is relatively large compared to the average R-curve of the series of tests. In contrast, the observed $t=0.100$ mm specimen has a relatively low R-curve compared to the other specimen of the series. Therefore, the small contrast observed on the pull-out height of the $t=0.075$ and 0.150 mm reflects the small contrast in the R-curves. Finally, the smallest pull-out fibers are seen in the thin-ply laminate, for which the smallest resistance to fracture is obtained. These observations indicate that the pull-out height is the parameter controlling the ply thickness effect (Fig. 7.11). The same trend is qualitatively reported by Teixeira et al. [95], who noticed an increasing pull-out height with increasing 0° ply thickness. Therefore, it supports our conclusions.

The last column in Table 7.4 contains the differences of height between the maximal value of the top profiles and minimal value of the bottom profiles. Once the COD at the crack starter $\bar{\delta}$ reaches these values, the fibers are completely pulled-out from their initial matrix surrounding and thus cannot exert resistance to opening anymore. These values reflect the COD from which the crack propagates in a steady-state manner (see also section 7.3.1).

7. Translaminar fracture

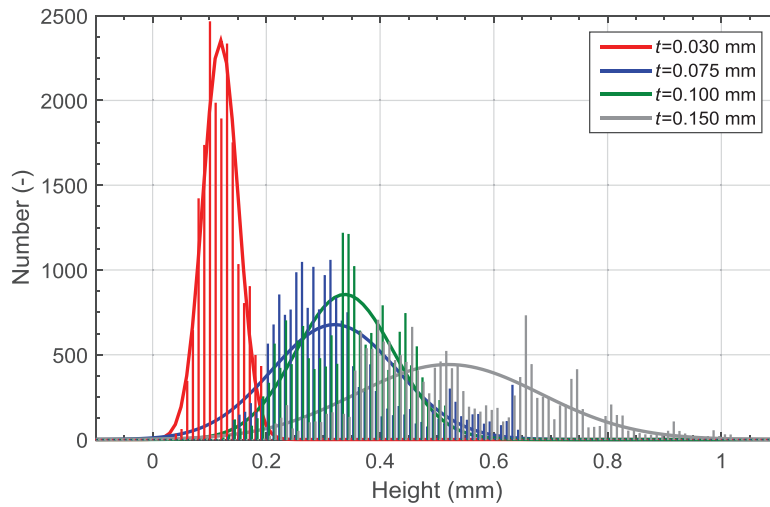


Fig. 7.10: Histogram of the height of the top envelope profile as a function of ply thickness and corresponding fitted normal distributions.

Table 7.4: Mean, standard deviation and extreme values of the top and bottom envelope profiles as a function of ply thickness.

t	Top profile			Bottom profile			Difference	
	Mean	Std	Max	Mean	Std	Min	Mean*	Extremes**
30	0.12	0.03	0.19	-0.03	0.02	-0.10	0.02	0.16
75	0.32	0.11	0.64	-0.04	0.03	-0.15	0.23	0.66
100	0.34	0.09	0.52	-0.03	0.04	-0.17	0.24	0.55
150	0.52	0.16	1.02	-0.02	0.07	-0.21	0.41	1.10

* Top profile mean – Bottom profile mean – 0.13

** Top profile max – Bottom profile min – 0.13

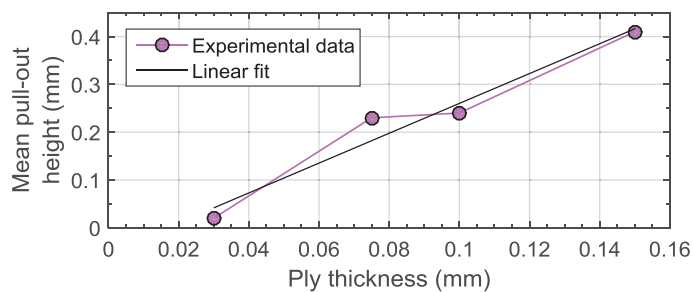


Fig. 7.11: Correlation between ply thickness and mean pull-out height.

To explain the higher pull-out fibers in the thick than thin-ply specimens, a fragmentation length can be computed as proposed by Jalalvand et al. [110]. The 0° plies can be seen as a low strain material and the more compliant 90° plies as a high strain material. Consequently, the critical fragmentation length l_c can be expressed as $l_c = t \cdot S / \tau_y$, where $S \approx 1600$ (MPa) denotes the tensile strength and $\tau_y \approx 80$ (MPa) the shear strength. Interestingly, this relation indicates the proportionality of the fragmentation length with respect to the ply thickness. Even if the so-computed critical fragmentation length are approximately 3 times larger than the observed largest pull-out fibers for each ply thickness, it shows how the pull-out height can be related to the ply thickness.

7.2.2 Quasi-isotropic (QI) specimens

A representative view of the fracture surface of the QI specimens for each of the three ply thicknesses is shown in Fig. 7.12 (a)-(c). The fracture surface of the CP $t=0.150$ mm is also shown for comparison. These fracture surface images are obtained following the same procedure as for Fig. 7.7. The topography of the surface is reconstructed based on images taken from the top. Therefore, the region below an inclined group of pull-out fibers always appears as a material region while it could be empty. Thus, the interpretation of the images for the QI specimens require some more care than for the CP specimens where every feature is oriented at either 0° or 90° .

The fracture surface of the QI specimens is much rougher than for the corresponding CP specimens. This change is caused by the presence of the $\pm 45^\circ$ plies. Indeed, a crack requires much less energy to propagate in the direction parallel to the fibers (intralaminar fracture) than in the direction orthogonal to the fibers (translaminar fracture). Therefore, in the $\pm 45^\circ$ plies the crack preferentially propagates along the fiber direction and thus tends to move away from the initial horizontal crack plane, in the 45° direction.

Similarly as for the CP specimens, the surface of the QI thin-ply specimens is much less rough than in the corresponding thick-ply specimens. The height of the profiles in the $\pm 45^\circ$ plies increases on the first millimeter of propagation and then remains globally constant along the crack extension. Again, this observation is fully consistent with the modeling hypotheses proposing a constant closing traction to represent the pull-out dissipative mechanism.

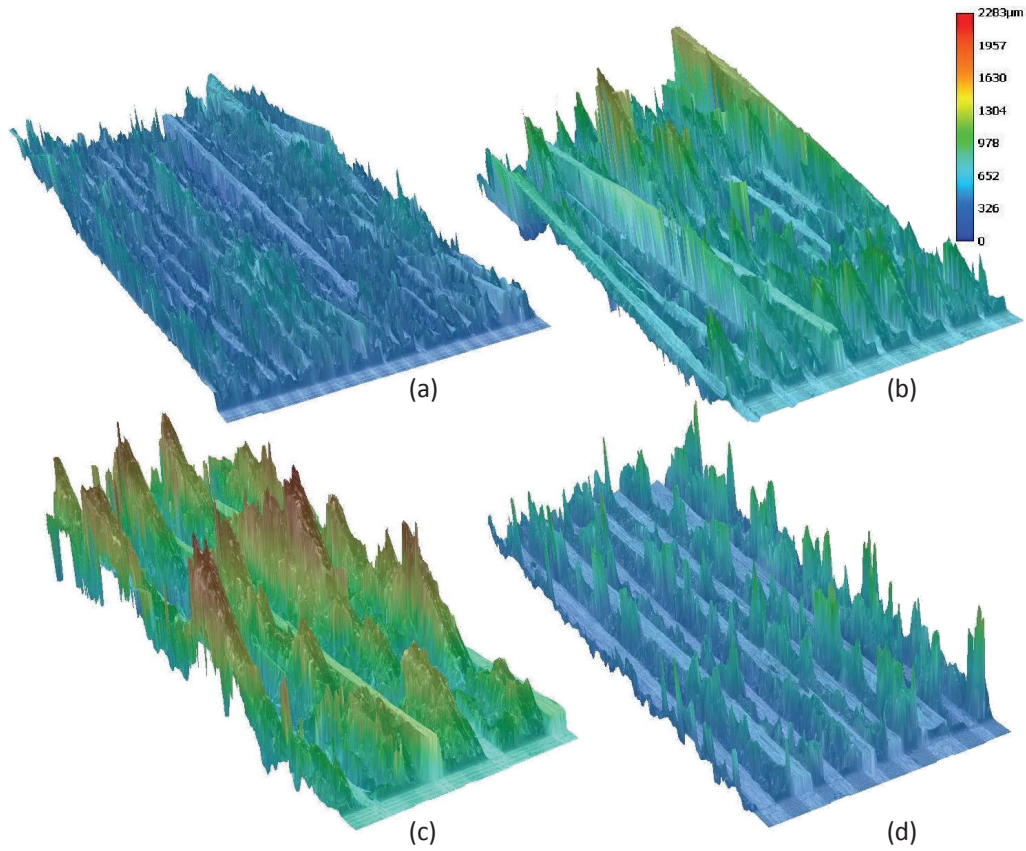


Fig. 7.12: Representative view of the fracture surface in the CT QI specimens with (a) $t=0.030$ mm, (b) $t=0.075$ mm, (c) $t=0.150$ mm. (d) For comparison, CT CP specimen with $t=0.150$ mm.

For the $t=0.150$ mm laminate, the highest point in the QI specimen is approximately twice higher than in the CP specimen. However, the height of the profile in the $\pm 45^\circ$ plies is not directly related to the fracture toughness since it mainly reflects the splitting of the $\pm 45^\circ$ plies. This mechanism dissipates much less energy than the pull-out mechanism.

The laminate fracture toughness measured in the QI specimens is lower than in the CP specimens. Geometrical considerations exposed at the end of section 7.1.2 explain that the resistance to fracture of the $\pm 45^\circ$ plies is expected to be two times lower than for the 0° plies. However, assuming that the rule of mixture (eq. (7.2)) is applicable, the experimental results show that if the ERR of the 0° plies is the same in the CP and QI specimens, the ERR of the $\pm 45^\circ$ plies lies in the bound of only 25% to 50% of the 0° plies. These calculations suppose that the plies of each orientation behave independently from the neighboring plies. But the fracture surface observation tends to prove that this hypothesis is not fully realistic.

The crack profile of four successive plies in the QI $t=0.150$ mm specimen is shown in Fig. 7.13. This graph validates the model of crack propagation for the $\pm 45^\circ$ plies shown in Fig. 7.6. The crack propagates alternatively in a plus and minus 45° direction. More importantly, this figure illustrates that the plies of different orientations have a strong interaction. Indeed, the profile of the 0° ply, which lies between the $\pm 45^\circ$ plies, is guided by the crack profile in the neighboring plies. Such an interaction is not observed in the CP specimens. The height of the pull-out in the 0° plies should not be considered in absolute value but rather in relative value with respect to the profile of the adjacent plies. Therefore, even if the profile of the 0° plies reaches higher values, the actual pull-out length in the 0° plies is probably lower in the QI specimens than in the CP specimens because of the interaction between the 0° and $\pm 45^\circ$ plies. Such an observation explains why the resistance to fracture is lower in the QI specimens compared to the CP specimens.

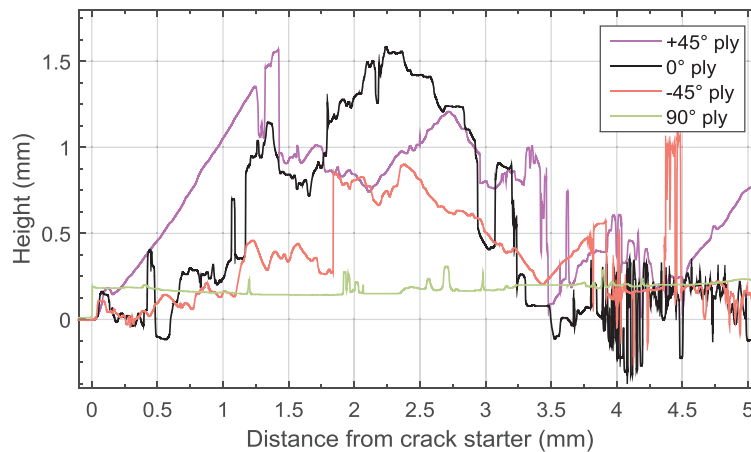


Fig. 7.13: Representative crack profile in four successive plies of a QI $t=0.150$ mm specimen.

7.3 Numerical modeling

7.3.1 Identification of bridging tractions

As explained in section 3.3.3, the cohesive traction-separation relations for translaminal fracture can be represented by a triangular law corresponding to the initiation ERR, followed by a constant traction level representing the fiber pull-out (Fig. 3.21). This generic shape has been obtained by optimization of a multilinear relation with the load-displacement curve as the objective function. Based on this preliminary work, the traction-separation relations of the seven series of tests are

7. Translaminar fracture

estimated, using four experimentally measured parameters: (i) σ_c the strength of the unnotched laminate [3] [for CP, S. Kohler, private communication], (ii) δ_m the COD at the crack starter when steady-state propagation is reached, (iii) $J_{I,i}$ the fracture toughness at initiation and (iv) $J_{I,ss}$ the fracture toughness at steady-state. Table 7.5 summarizes the obtained traction-separation parameters for the representative specimens of the seven series of tests. Interestingly, the estimated values of the pull-out length δ_m scale with the ply thickness (Table 7.5) and lead to almost equal values of the pull-out traction $\sigma_p = 35$ MPa in each series of tests (Fig. 7.14 (a)). Moreover, the pull-out lengths δ_m (Table 7.5) correlate well with the maximal pull-out heights observed on the fracture surface of representative specimens (Table 7.4). The almost equal pull-out traction $\sigma_p = 35$ MPa in each series of tests is fully consistent with the observation that the frequency of pull-out creation along the crack propagation is of the same order of magnitude in each ply thickness. This empirical scaling relation combined with σ_p could be used to predict the pull-out contribution $J_{I,p}$ and compute the total ERR $J_{I,tot} = J_{I,i} + J_{I,p}$. Moreover, the initiation ERR, steady-state ERR, unnotched strength and maximal COD also scales linearly with the ply thickness. Therefore, empirical relations as shown in Fig. 7.14 (b)-(e) can be simply established by testing the two extreme cases. These relations can then be used to interpolate the traction-separation parameters for intermediate ply thicknesses.

Table 7.5: Traction-separation parameters for the translaminar fracture.

Lay-up	t (mm)	σ_c (MPa)	δ_m (mm)	$J_{I,i}$ (kJ/m ²)	$J_{I,ss}$ (kJ/m ²)
CP	0.030	913	0.15	19.5	23.9
CP	0.075	1004	0.50	32.2	46.8
CP	0.100	1010	0.64	47.6	66.9
CP	0.150	1066	1.12	59.6	97.3
QI	0.030	847	0.18	15.8	22.9
QI	0.075	781	0.25	29.6	37.7
QI	0.150	753	0.85	55	84.3

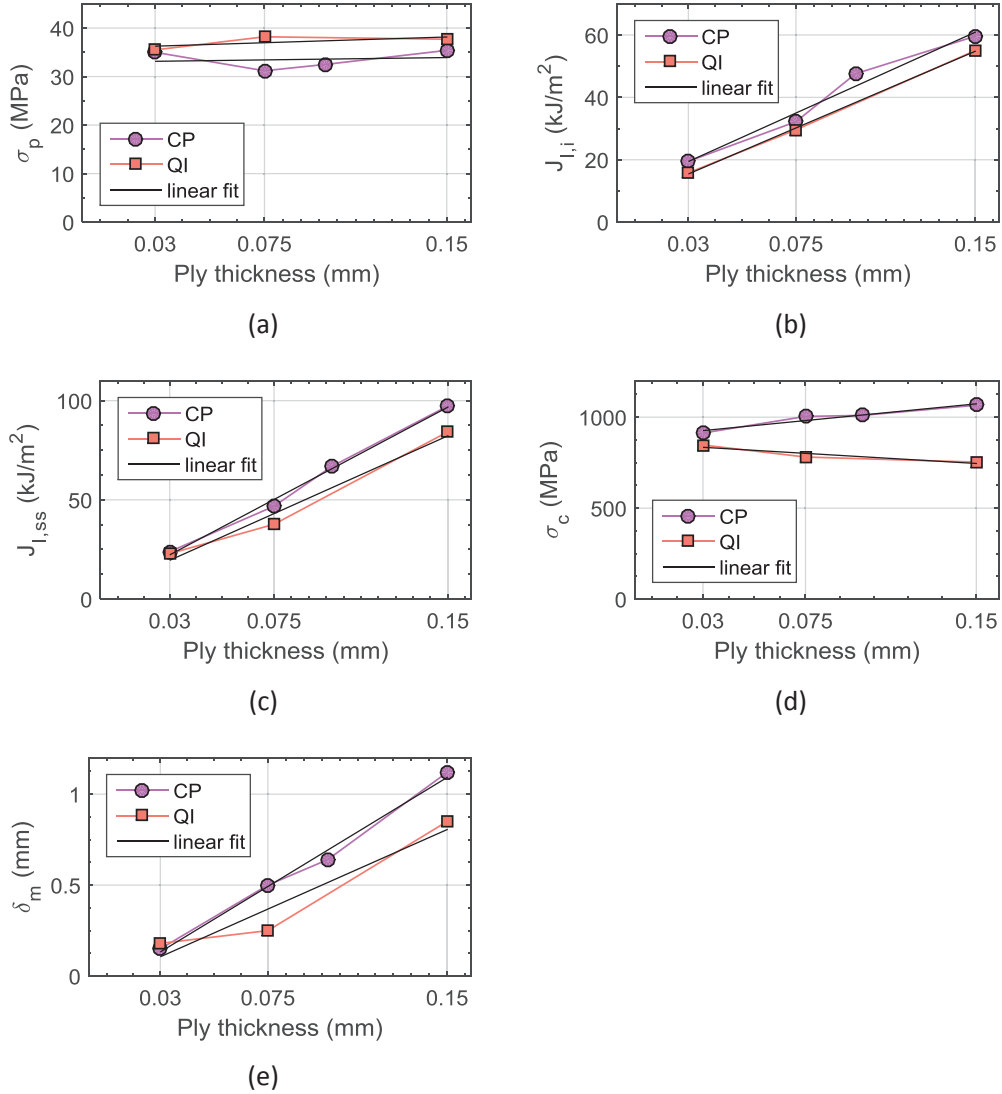


Fig. 7.14: For the CP and QI specimens, linear scaling as a function of ply thickness of (a) the pull-out tractions, (b) the initiation ERR, (c) the steady-state ERR, (d) the unnotched strength and (e) the maximal COD.

7.3.2 Cohesive elements simulations

The obtained traction-separation profiles are implemented in cohesive element models in Abaqus. Similarly as the approach used in section 4.4.1.2, the cohesive relation is split into two relations, one representing the initiation ERR and one for the fiber pull-out mechanism. This technique allows a more precise definition of the

damage parameter D . Both relations are then implemented in two superimposed layers of cohesive elements acting similarly as two stiffnesses in parallel.

The geometry of the CT specimens is modeled in 2D plane stress condition, with approximately 18000 8-nodes quadratic elements (CPS8R). The translaminar fracture path is reproduced with two superimposed layer of 0.02 mm thick linear cohesive elements (COH2D4). Finally, the cohesive relations are implemented in tabular form with 300 entries for the initiation part and 330 values for the fiber pull-out relation. The maximal applied displacement is imposed to two reference points kinematically coupled to the holes where the loading pins are inserted.

The load-displacement curves obtained from the cohesive simulations of the four CP tests are displayed in Fig. 7.15. The numerical simulations are globally in very good agreement with the experimental curves. The stiffness of the loading part before the first load drop is accurately predicted. Note that the $t=0.150$ mm specimens are initially less stiff than the other specimens because its initial crack is 2.5 mm longer. Since the material is considered linear elastic in the model, it fails to represent the plastic behavior occurring in the $t=0.150$ mm specimen. As shown in Fig. 7.2, the secant stiffness at the first load drop is reduced by 16% when compared to the initial stiffness. Reducing the shear modulus in the same proportion helps to predict the correct load level at crack initiation and subsequent crack growths (Fig. 7.16).

The peak load, which is mainly related to fracture toughness at initiation is well predicted. In average on the four ply thicknesses, it is overestimated by only 2.4 %. On the post-peak region, the prediction is very good as well. Of course, the static model cannot represent the crack advance by successions of small jumps, which is a dynamic effect. However, the predicted load is within the experimental scatter engendered by the load jumps and is in very good agreement on the parts where the cracks propagate in a stable manner.

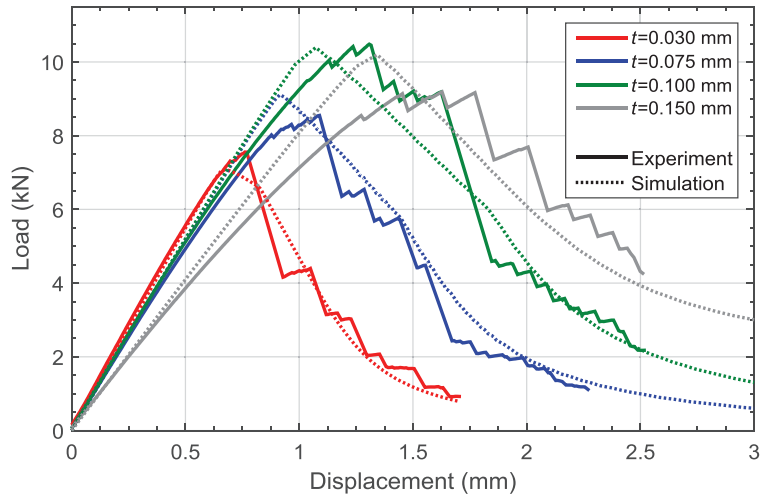


Fig. 7.15: Experimental and simulated load-displacement curves for CP specimens.(see text for details)

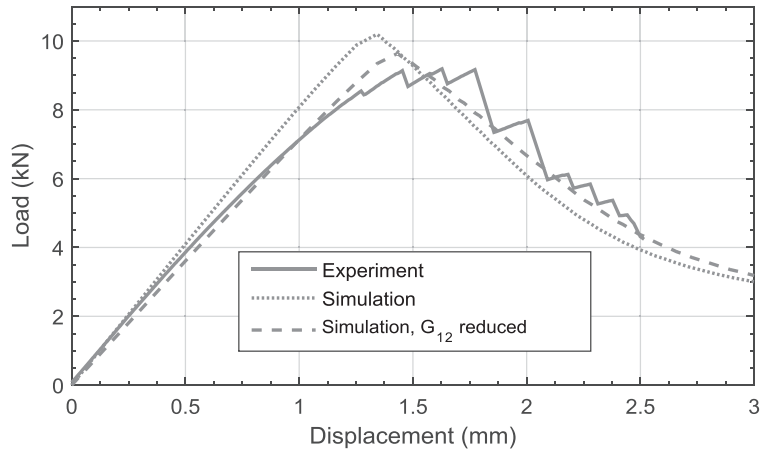


Fig. 7.16: Simulation of the load-displacement curve of a selected $t=0.150$ mm specimen with a reduced shear modulus. (see text for details)

The load-displacement curves obtained from the cohesive simulations of the three QI tests are displayed in Fig. 7.17. Since the undamaged loadings are more linear in the QI than in the CP specimens, they are better predicted by the linear cohesive models. Here also, the load peak prediction is excellent. In average on the three ply thicknesses, it is overestimated by 6.5%.

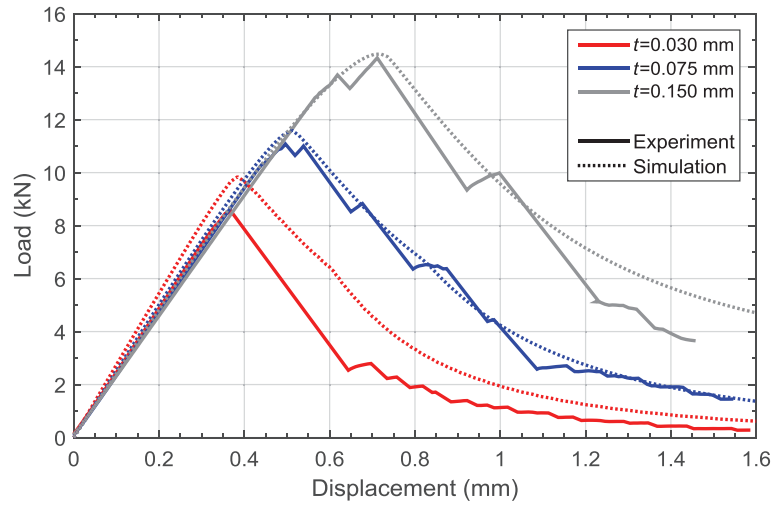


Fig. 7.17: Experimental and simulated load-displacement curves for QI specimens.(see text for details)

Overall, these simulation results show that even a simple cohesive model such as the one proposed in this work can accurately predict the translaminar crack growth of a wide range of ply thicknesses for both the CP and QI layups. In this model, fiber pull-out tractions are considered uniform until reaching a certain COD. Thanks to the simplicity of the proposed model, all parameters can be identified from direct experimental measurements. Moreover, thanks to the observed scaling relation, the results can easily be interpolated to different ply thicknesses. In addition, Li et al. [111] and Laffan et al. [97] have shown that blocking $t=0.125$ mm 0° plies in the stacking sequence increases almost linearly the laminate fracture toughness with respect to the thickness of the block of plies (from 0.125 to 0.6 mm). Therefore, the scaling trend observed in the present study can reasonably be extrapolated to ply thicknesses slightly larger than the ones tested experimentally.

7.4 Summary

The translaminar fracture toughness is measured on CP and QI CT specimens. A Matlab code is developed to compute the contour J-integral based on displacement fields obtained by DIC. This data reduction method has as main advantage to be completely independent of the crack length which is hard to define and measure accurately. A strong ply thickness effect is observed. Firstly, on the load displacement curves, the first load drop occurs at 33% (CP) and 41% (QI) lower load levels in the $t=0.030$ mm than $t=0.150$ mm specimens. Secondly, at crack initiation, the ERR is 70%

(CP) and 72% (QI) lower in the $t=0.030$ mm than $t=0.150$ mm specimens. Finally, at steady-state propagation, the resistance to fracture is 80% (CP) and 74% (QI) lower in the thin-ply as compared to the values in the thick-ply specimens. Overall the ERR values for the QI specimens are approximately 25% lower than for the corresponding CP specimens. The ERR at initiation and subsequent crack growth in the CP specimens scales linearly with the ply thicknesses on the range of observation of this work. In contrast to the inter- and intra-laminar fracture, the translaminar fracture toughness is already strongly decreased at crack initiation and the percentage of decrease is larger.

The fiber pull-out is the dominant toughening mechanism in the translaminar fracture of CP and QI laminates. In average, the height of the pull-out correlates with the ply thickness. The results demonstrate that the effect of ply thickness is attributed to the change of pull-out height. The lower ERR measured in the QI specimens compared to the CP ones is partially attributed to the ERR of the $\pm 45^\circ$ plies which is 2 times lower than for the 0° plies due to the triangular shape propagation profile. The remaining difference is explained by the interaction between the plies of different orientations, which reduces the relative difference between the crack profiles in each ply orientation and thus limits the length of the pull-out fibers.

Since the process zone is relatively small in the CT specimens, a simple modeling approach is proposed in this work. The initiation ERR is represented by a triangular traction-separation relation, where the maximal traction corresponds to the strength of the unnotched laminates. The pull-out mechanism is represented by a constant traction level until the separation value corresponds to the COD measured at the crack starter when steady-state propagation is reached. These COD values estimated from side views of the specimens correlate well with the height of the largest pull-out fibers observed on the fracture surfaces. The results of the cohesive simulations are in very good agreement with the experimental load-displacement curves.

Chapter 8

Improving the fracture toughness

Chapters 4 to 7 show that the inter-, intra- and trans-laminar fracture toughness are lower in thin-ply than in thick-ply laminates. Therefore, the use of thin-ply composites in critical applications such as aeronautics can be questioned. Indeed, the low toughness properties and quasi brittleness of failure are a challenge to ensure the safety of the structures and to schedule maintenance programs. Therefore, it is necessary to find a way to keep the advantages offered by the thin-ply size effect while improving the toughness properties. Through selected experiments, this chapter shows three techniques to improve the resistance to fracture.

8.1 Change of fiber/matrix combination

The inter- and intra-laminar fracture is strongly influenced by the fiber/matrix interface and by the toughness of the matrix. Similarly, the translaminar fracture is affected by the toughness of the fibers and by the fiber/matrix interface. Therefore, a change of fiber/matrix combination can substantially influence the toughness properties. As part of a CTI project, Amacher et al. have developed a highly toughened thin-ply prepreg system with toughness properties similar as the latest aerospace systems [112]. They used T800 carbon fibers that have an intermediate modulus (294 GPa), an intermediate ultimate tensile strength (5880 MPa), but a very high strain at failure (2.0%) [113]. In collaboration with their industrial partners, they developed and optimized a 180°C curing highly toughened epoxy system, referred to as Aero2. The T800 / Aero2 prepreg at $g=67 \text{ g/m}^2$ is optimal since it reaches 100% of the fiber ultimate strain (85% at onset of damage). Further reducing the ply thickness would be useless, since the full potential of the T800 fibers is reached (Fig. 8.1). The onset of damage of the QI laminate occurs at 900 MPa and the ultimate failure at 1100 MPa [112] (Fig. 8.1). In Fig. 8.1, the matrix Aero1 refers to the same epoxy resin as the Aero2, but with a not yet optimized formulation. These outstanding strength

8. Improving the fracture toughness

properties represent an increase of 21% on the onset value and 40% on the ultimate value when compared to the M40JB / TP80ep (with ply thickness $t=0.075$ mm).

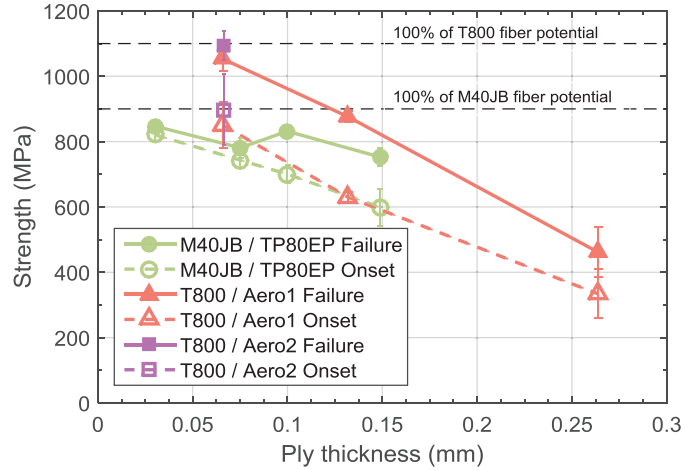


Fig. 8.1: Onset of damage and ultimate tensile strengths for different ply thicknesses and fiber / matrix combinations (adapted from [112]).

In terms of toughness, the properties are also improved, thanks to the highly toughened matrix (Aero2) and the tough fibers (T800). In mode I interlaminar fracture of $h=4$ mm thick DCB specimens, the ERR values are significantly higher in the T800 / Aero2 system than in M40JB / TP80EP. At crack initiation, the ERR is increased by 60% (Fig. 8.2). To account for toughening mechanisms such as fiber bridging, Amacher et al. have computed the average ERR value on 100 mm of crack propagation. In the M40JB / TP80EP $h=4$ mm specimens, the maximal crack increment is smaller than 100 mm (Fig. 4.4). To obtain a value for comparison with the T800 / Aero 2 specimens, the R-curves are extrapolated by using the considered steady-state ERRs. The propagation ERR is 120% higher in the T800 / Aero2 system when compared to the M40JB / TP80EP laminate with $t=0.075$ mm. Both the initiation and propagation ERR values are higher in the $t=0.067$ mm T800 / Aero2 specimens than in the $t=0.150$ mm M40JB / TP80EP specimens.

8.1 Change of fiber/matrix combination

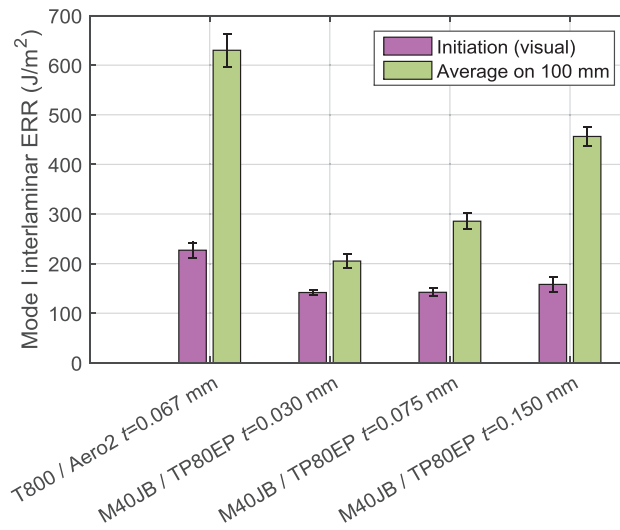


Fig. 8.2: Mode I ERR at crack initiation and in average on 100 mm of propagation in interlaminar fracture. (See text for details)

The increase in the interlaminar toughness is not limited to the mode I loading condition. Indeed, a significantly higher ERR is also measured in mode II. It is worth recalling here that in mode II the R-curves were found practically independent of ply thickness and constant along crack propagation. The average ERR on 40 mm of propagation in the $h=4$ mm 4ENF specimens is 57% higher in the new system. Interestingly, this value is close to the increase in the ERR at crack initiation in mode I. This observation shows that the increase in the matrix toughness and fiber / matrix cohesion triggers the crack initiation in mode I and mode II interlaminar fracture.

The translaminar fracture is also affected by the change of fiber / matrix combination, as shown in Fig. 8.3. The average R-curve for the T800 / Aero2 specimen made of $t=0.067$ mm plies is higher than the corresponding results for each of the ply thicknesses tested on the M40JB / TP80EP specimens. In particular, the ERR of the T800 / Aero2 system is increased by 125% at crack initiation ($\Delta a = 0.5$ mm) and 172% after 10 mm of crack propagation, when compared to the $t=0.075$ mm M40JB / TP80EP specimens. The increase in the fracture toughness is substantial. Indeed, the ply thickness considered for the T800 / Aero2 system is the one at which the full potential of the fiber is reached in terms of ultimate tensile strength. Since the translaminar fracture toughness is generally much affected by the ply thickness, even higher ERR values are expected if thicker plies are used. Unfortunately, this expectation could not be verified since specimens made of only $t=0.067$ mm plies were available. In M40JB / TP80EP, the full strength potential of the fibers is reached

with $t=0.030$ mm plies. At this strength based optimized ply thickness, the translaminar fracture ERR is 4 times (at initiation) to 5.3 (at 10 mm of propagation) lower in M40JB / TP80EP than in T800 / Aero2 specimens.

In absolute values, the fracture toughness of the T800 / Aero2 system is very good. As a comparison the fracture toughness reaches approximately 52 kJ/m^2 for aluminum alloys, 64 kJ/m^2 for titanium alloys and 107 kJ/m^2 for steel alloys [114]. The ERR at crack initiation of the T800 / Aero2 composite (64 kJ/m^2) is of comparable magnitude as for light metal alloys and the ERR propagation value compares with the toughness of heavy alloys.

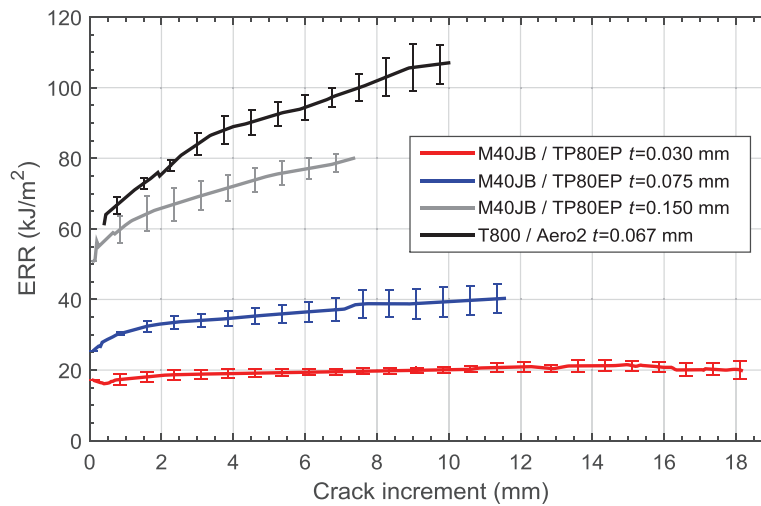


Fig. 8.3: Average R-curves of QI laminate for different ply thicknesses and fiber / matrix combinations.

8.2 Use of interlayer toughener

The compression after impact (CAI) value is an important evaluation criterion of composite laminates and is frequently used in the aeronautic industry [115]. The CAI tests consist in measuring the residual compressive strength of specimens that were impacted by a drop-weight beforehand. The out-of-plane impact causes a bending loading which might lead to the initiation and propagation of mode II interlaminar cracks. Therefore, the mode II interlaminar fracture ERR must be improved to increase the CAI values.

One way to increase the interlaminar toughness is to add toughened particles between the laminate layers. This technique, called interlayer toughening (IT), is used

by Amacher et al. who added 7 to 13 g/m² of reactive super fine particles of polyethersulfone (RSFP) between every 1, 3 or 7 laminate layers. They performed CAI tests according to the ASTM standards D7136 [116] and D7137 [117] with 4 mm thick specimens and 30.2 J of impact energy. As shown in Fig. 8.4, the T800 / Aero2 system has a CAI strength 33% higher than the M40JB / TP80EP. The use of IT further increases the CAI value by up to 43%. When IT is added between every single layer, the CAI strength reaches 285 MPa, which corresponds to a value comparable with the current generation of aerospace composites.

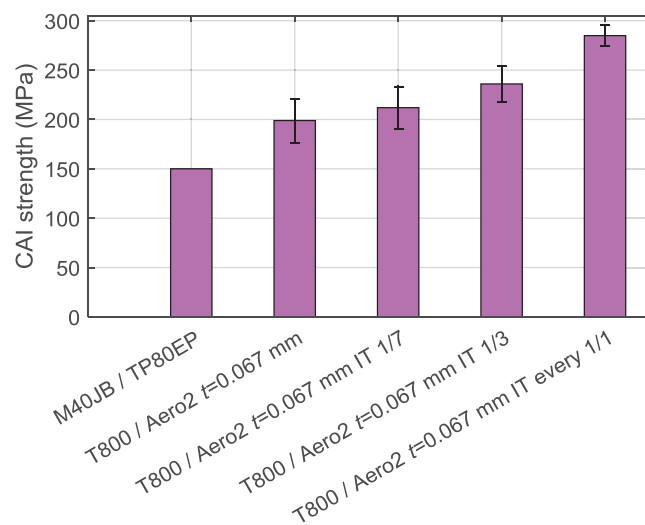


Fig. 8.4: CAI strength for different fiber / matrix combinations and IT. IT 1/n refers to IT every n layers. (adapted from [112])

The mode II interlaminar fracture of specimens with IT is assessed by testing 4ENF specimens. In these specimens, IT is added between every layer. Three different amounts of IT powder are tested: 4, 8 and 12 g/m². As already mentioned in section 8.1, the mode II ERR is increased by 57% when changing the fiber / matrix combination from M40JB / TP80EP to T800 / Aero2. Adding 4 or 8 g/m² does not contribute to increase the interlaminar fracture ERR. It even leads to slightly lower values (4.8 and 7.6%, respectively). However, the addition of 12 g/m² of RSFP increase the ERR by 68%. The causes of such a different behavior of the 12 g/m² IT compared to the 4 or 8 g/m² is not clearly established. However, the observation of the fracture surface of the 4 and 8 g/m² IT specimens reveal the absence of large polyethersulfone aggregates. In contrast, such aggregates were observed on the fracture surface of the 12 g/m² IT specimens. Such a contrast can explain the threshold effect observed on the mode II interlaminar fracture toughness and could be a sign of a crack migration

away from the toughened interface for the lower concentrations. More detailed microscopy observations would be necessary to confirm this hypothesis.

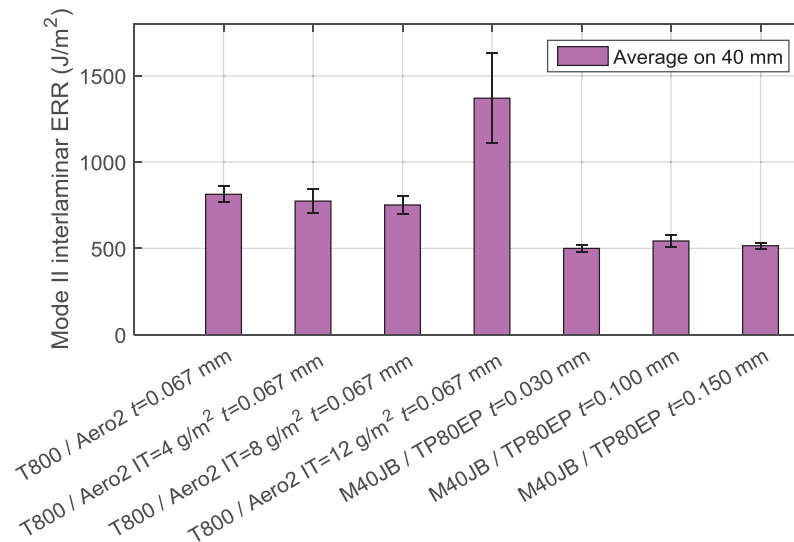


Fig. 8.5: Mode II average ERR on 40 mm of propagation in interlaminar fracture of different fiber / matrix combinations and amount of IT.

The IT strategy shows a substantial increase in the CAI strength. This improvement is attributed to the higher resistance to mode II interlaminar crack when IT is added. However, the IT has also drawbacks. Indeed, the IT strategy adds an operation in the production process, which incurs additional costs. Moreover, the deposition of the IT powder between the laminate layers considerably decreases the tack of the prepreg. The tack of the prepreg is the property that creates a sufficient bond between two successive plies so that the prepreg can be laid up. Therefore, IT can render the production process very difficult, if not impossible. As a consequence, IT strategy is reserved for very specific applications.

8.3 Use of fiber hybridization

As shown in section 8.1, a change of fiber / matrix combination can substantially increase the translaminar fracture toughness of the composite. The use of fiber hybridization can further increase the translaminar ERR. There are different ways to realize fiber hybridization:

- A tow-level hybridization where different types of fibers are intermingled in one single ply;

- A ply-level hybridization where plies made of different fibers are stacked alternatively.

In this work, the aim is to promote larger fiber pull-out, since it is shown by Bullegas et al. [94] that high pull-out significantly increases the translaminar fracture toughness. Such an objective can be reached by stimulating the fragmentation of low strain fibers in a ply-level hybrid composite based on high strain fibers. The design of such a hybrid composite is not simple since the following specifications should be fulfilled [112, 110]:

- The low strain fibers must fragment before the failure of the high strain fibers;
- The stress transferred by the failure of the low strain to the rest of the specimen should not lead to its catastrophic failure;
- The fragmentation length should be comprised in a range that promotes large fiber pull-out. On one hand, a small fragmentation length leads to a limited effect on the dissipated energy. On the other hand large fragmentation length might not affect at all the dissipated energy because of the excessive distance to the crack plane. Therefore, a trade-off must be found and values between 0.1 and 1 mm are targeted.

The fragmentation length is computed based on the shear-lag model proposed by Jalalvand et al. [110]. Small fragmentation lengths require very thin-ply, which limits the amount of possibilities in the selection process of the hybrid system. Amacher et al. [112] found that a hybridization of $t=0.067$ mm T800 plies with $t=0.020$ mm HR40 plies fulfill the requirements. The expected fragmentation length ranges from 0.5 to 1 mm. The HR40 carbon fiber is produced by Mitsubishi chemical. Its mechanical properties are close to the ones of the Toray M40JB fibers, with a high modulus (375 GPa), a relatively limited strength (4410) and a low strain at failure (1.2%) [118]. Two different configurations are considered, with the HR40 fibers parallel or orthogonal to the adjacent T800 ply. As schematized in Fig. 8.6 these pairs of plies are then stacked following a classical QI sequence:

- T800 / HR40 0°/0° hybrid (Fig. 8.6 (a)):
 $[0^\circ_{\text{T800}} / 0^\circ_{\text{HR40}} / +45^\circ_{\text{T800}} / +45^\circ_{\text{HR40}} / 90^\circ_{\text{T800}} / 90^\circ_{\text{HR40}} / -45^\circ_{\text{T800}} / -45^\circ_{\text{HR40}} /]$
- T800 / HR40 0°/90° hybrid (Fig. 8.6 (b)):
 $[0^\circ_{\text{T800}} / 90^\circ_{\text{HR40}} / +45^\circ_{\text{T800}} / -45^\circ_{\text{HR40}} / 90^\circ_{\text{T800}} / 0^\circ_{\text{HR40}} / -45^\circ_{\text{T800}} / +45^\circ_{\text{HR40}} /]$

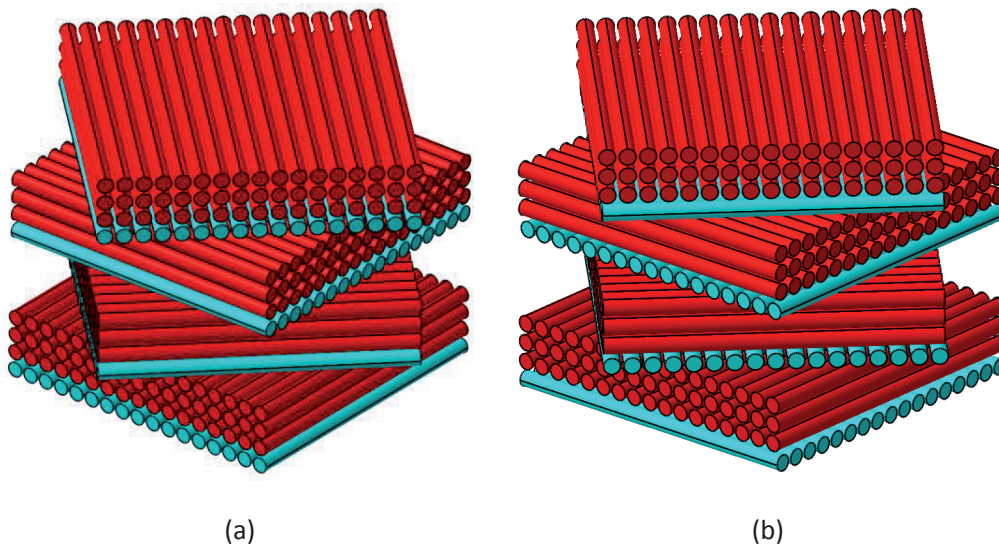


Fig. 8.6: Schematic view of the T800 / HR40 (a) $0^\circ/0^\circ$ and (b) $0^\circ/90^\circ$ hybrid (adapted from [112]).

The stress-strain curves are strongly affected by the fiber hybridization. Indeed, after the linear-elastic response, the hybrid laminates exhibit a pseudo-ductile behavior, rather than a quasi-brittle failure. In particular, the $0^\circ/0^\circ$ hybrid laminate has almost 0.5% of pseudo plastic strain before failure. However, the stress at onset of damage and ultimate tensile strength are reduced, when compared to the pure T800 laminate. The damage onset of the $0^\circ/0^\circ$ hybrid laminate occurs at the ultimate strain of the HR40 fibers. It occurs at a slightly lower stress level for the $0^\circ/90^\circ$ configuration. The onset of damage in the hybrid laminates are 21% ($0^\circ/0^\circ$) and 20% ($0^\circ/90^\circ$) lower than the corresponding value of the T800 $t=0.067$ laminate. The complete failure of the hybrid specimens occurs when the ultimate strain of the T800 fibers is reached. Interestingly, the tensile modulus of the hybrid laminates just before failure corresponds to tensile modulus computed by assuming that the HR40 plies are not active any more (stiffness set to zero). The ultimate strengths of the $0^\circ/0^\circ$ and $0^\circ/90^\circ$ hybrid laminates are 25% and 34% lower than the corresponding value of the T800 laminate.

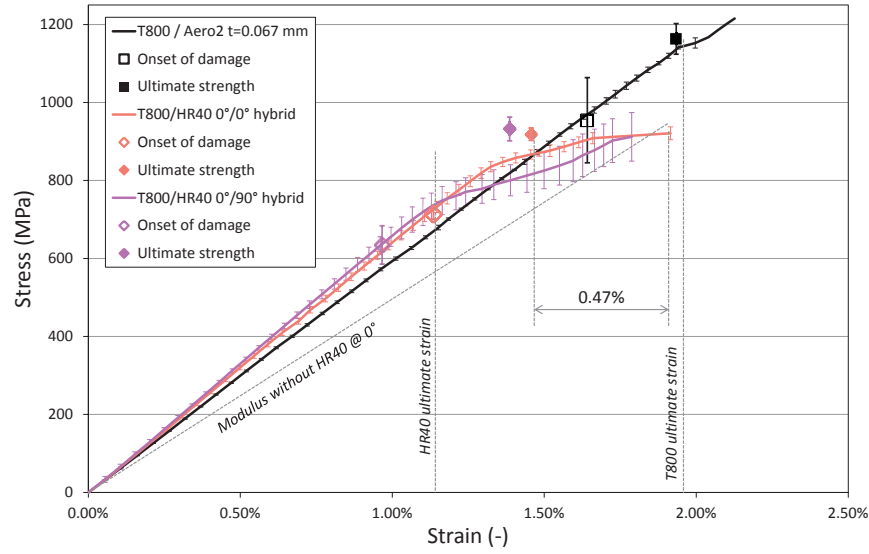


Fig. 8.7: Averaged stress-strain curves for the T800 / Aero2 and T800 / HR40 QI hybrid laminates in unnotched tension. The dots for ultimate strength of the hybrid represent the elastic part of the strain (adapted from [112]).

The effect of fiber hybridization on the translaminar fracture is not as large as expected. Indeed, the R-curves of the hybrid specimens are higher than for the pure T800 laminate, but not much (Fig. 8.8). At crack initiation, the increase in the translaminar toughness is of 8.3% for the 0°/0° and 15.5% for the 0°/90° configuration. At 8 mm of crack increment, the increase in the ERR is of 5.2% (0°/0°) and 19.8% (0°/90°). Since the stress-strain curves show that the fiber hybridization works as expected in the design process, these relatively small increases in the toughness are somehow disappointing.

A possible explanation of such a behavior is that another parameter influences detrimentally the fracture toughness. This parameter most probably is the ply thickness. Indeed, in the fiber hybridization strategy, very thin plies of HR40 are used. However, as shown in section 7.1.2, small ply thicknesses strongly reduce the translaminar fracture toughness. The HR40 fibers being similar to the M40JB fibers, the toughness of the $t=0.020$ mm HR40 fibers can be assumed to be approximately similar to the $t=0.030$ mm M40JB plies ($J_{HR40,t=0.020} \simeq J_{M40JB,t=0.030}$). As a consequence, in the absence of interaction mechanisms specific to fiber hybridization, the fracture toughness should be equal to the value computed by a simple rule of mixture:

8. Improving the fracture toughness

$$J_{T800/HR40} = \frac{t_{T800}}{t_{T800} + t_{HR40}} J_{T800} + \frac{t_{HR40}}{t_{T800} + t_{HR40}} J_{HR40} \quad (8.1)$$

where $t_{T800} = 0.067$ mm and $t_{HR40} = 0.020$ mm denotes the ply thickness of the T800 and HR40, respectively.

The R-curve computed with eq. (8.1) is displayed in dashed line in Fig. 8.8. Compared to this R-curve, the $0^\circ/0^\circ$ and $0^\circ/90^\circ$ hybrid configurations are 30.9% and 39.5% higher at crack initiation and 29.1% and 47.0% higher at 8 mm of crack increment. This significant increase shows that the fiber hybridization technique indeed triggers additional dissipative damage mechanisms, but its effect is partially counterbalanced by the detrimental ply thickness effect. Indeed, by using very thin high modulus plies in complement to intermediate thickness high strength ones, 23% of the specimen thickness is replaced by plies having an intrinsically low translaminar toughness. Thus further optimization of the fiber hybridization concept appears necessary.

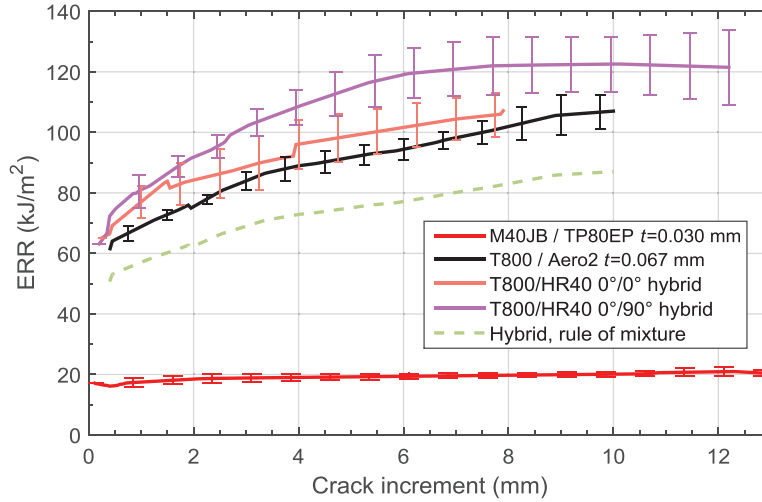


Fig. 8.8: Average R-curves of QI laminate for the T800 / Aero2 and hybrid laminates. The dashed line represent the rule of mixture between the T800 / Aero2 ($t=0.067$ mm) and M40JB / TP80EP ($t=0.030$ mm).

The fiber hybridization strategy gives a very interesting pseudo-plastic behavior observed on the stress-strain curves. However, the stress at onset of damage and ultimate strength are reduced compared to the pure T800 laminate. In terms of resistance to fracture, the increase is relatively small. Indeed, the effect of fiber hybridization is partially counterbalanced by the ply thickness effect. Since the effect of ply thickness is shown to be important in section 7.1.2, an increase in the thickness

of the T800 plies would have increased the fracture toughness as much as the fiber hybridization. Unfortunately, only one ply thickness of T800 / Aero2 was available for translaminar fracture testing and this hypothesis could not be verified.

8.4 Summary

This chapter presents three techniques to improve the resistance to fracture of thin-ply composites. The interlayer toughening strategy specifically addresses the resistance to interlaminar fracture. The 4ENF tests shows that from a certain amount of IT, the mode II interlaminar fracture is significantly increased. As a consequence, the extent of interlaminar fracture under impact loading is reduced in the laminates with IT and the residual compressive strength (CAI) is improved. The downside of this strategy is the more difficult production process and resulting higher costs. Nevertheless, the mode II testing of IT composites remains a challenge because of potential crack migrations away from the toughened interfaces that could introduce some bias when compared to more complex loading cases such as impact response of a quasi-isotropic laminate.

The fiber hybridization strategy addresses the resistance to translaminar fracture. The CT tests on the QI specimens show a small increase in the translaminar fracture with the $0^\circ/90^\circ$ T800/HR40 hybrid composite and almost no improvement with the $0^\circ/0^\circ$ hybrid configuration. This relatively low increase in the ERR is explained by the insertion of very thin layers of HR40 that have a very limited resistance to fracture, due to the detrimental ply thickness effect. In terms of stress-strain relations, the hybrid laminates have an interesting pseudo-plastic deformation of about 0.5% before failure. However, the onset of damage and ultimate strength occur at lower strain levels. Similarly as the ply thickness effect, the fiber hybridization effect illustrates the trade-off between strength and toughness properties.

Finally, the change of fiber / matrix combination shows substantial changes in strength and toughness properties. The T800 / Aero2 system fails at a higher ultimate strength than the M40JB and reaches the full potential of the fibers at a larger ply thickness. The interlaminar mode I and II as well as the translaminar mode I fracture are significantly increased when changing from M40JB / TP80EP system to the T800 / Aero2 composite.

Fig. 8.9 summarizes the strength versus translaminar fracture toughness properties for the different systems studied in this work. Clearly, the increase in the ply thickness and fiber hybridization augments the ERR values at the expense of

8. Improving the fracture toughness

significant decrease in the strength properties. The negative slopes of the curves representing the change of ply thickness and fiber hybridization illustrate the trade-off often faced in the process of material selection. In contrast, the curve representing the change of fiber / matrix combinations has a positive slope, indicating that both the strength and toughness properties are improved at the same time. As such an improvement is achieved, one can say that the T800 / Aero2 system belongs to a completely different class of carbon / epoxy composites, compared to the M40JB / TP80EP system.

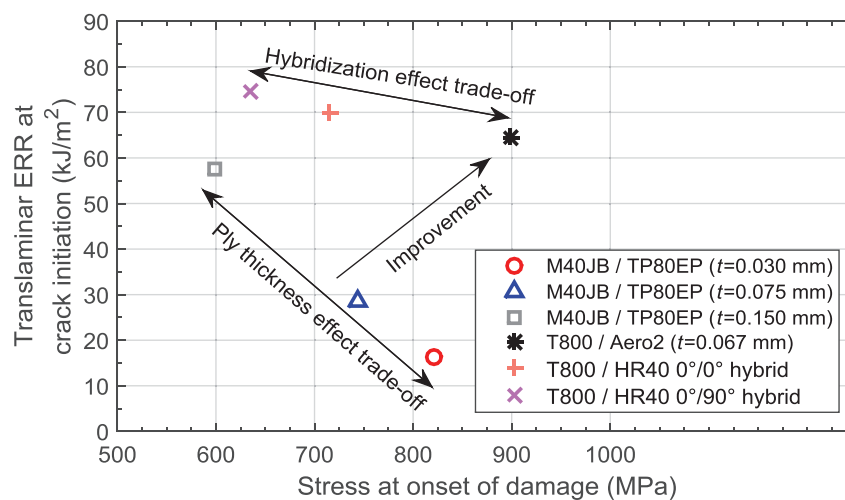


Fig. 8.9: Strength (onset of damage) vs translaminar fracture toughness (at crack initiation) for the different systems studied in this work.

Chapter 9

Conclusions and perspectives

9.1 Summary and conclusions

The conducted study investigates the effects of ply thickness on the fracture properties of a thin-ply carbon / epoxy system. It provides a complete view of the three basic modes of failure (inter-, intra-, and trans-laminar fracture), instead of being limited to only one preferential crack orientation. The ply thickness effects are assessed by testing the M40JB / TP80EP system made of standard-ply ($t=0.150$ mm) down to very thin-ply ($t=0.030$ mm). As a summary of this work, the scientific questions raised in the introduction can be answered.

How does the ply thickness affect the fracture toughness and R-curve behavior of thin-ply unidirectional composites for the inter- and intra-laminar fracture?

The mode I interlaminar fracture at crack initiation is found practically independent of ply and specimen thickness ($G_{I,i}=140\pm11$ J/m²). However, at subsequent crack growth, the R-curve is considerably affected by the ply thickness (Fig. 9.1). This effect is reflected by two main features: (i) steady-state propagation is reached at much smaller crack increment in thinner-ply specimens and (ii) the ERR plateau level is decreased by approximately 50% when changing from thick-ply to thin-ply laminate. Overall, the steady-state ERR is 1.4 to 3.4 times higher than the initiation ERR.

In mode II interlaminar fracture, no significant ply thickness effect is measured. After the first 5 mm of crack increment, the ERR remains constant along propagation. The largest ERR is measured on the intermediate-ply laminate and is in average less than 9% larger than in thin-ply. The thick-ply laminate exhibits a resistance to fracture of similar magnitude as the thin-ply. The absence of important toughening

mechanism acting in the wake of the crack as in mode I, explains the absence of significant ply thickness effect in mode II.

The intralaminar fracture in mode I loading condition is affected in a similar manner as the interlaminar fracture, but with a different magnitude. The initiation ERR is practically independent of ply thickness, even if the measured ERR are slightly higher in the crack initiation of thin-ply, compared to the other ply thicknesses. In contrast, the evolution of fracture resistance along crack advance is strongly affected by the ply thickness. In thin-ply, the ERR is higher on small crack increments (<20 mm) but reaches steady-state propagation at a 23% lower value than in thick-ply specimens. Overall, the intralaminar steady-state ERR is at least 5 times higher than the initiation ERR.

While the characterization of ply thickness effect on the inter- and intra-laminar has not been reported elsewhere in the literature, the specimen thickness is known to affect the R-curve behavior associated with inter- and intra-laminar cracks. In this work, specimens of different thicknesses for each of the ply thicknesses are tested to assess the impact of both effects on one the other. Both effects work concurrently and do not appear to have a reciprocal influence. Globally, on the range of observations, the change of ply thickness has a stronger impact on the steady-state inter- and intra-laminar ERR than the variation of specimen thickness.

How much is the fracture toughness reduced for translaminar cracks in CP or QI laminates made of very thin-ply?

The translaminar cracks propagation is studied by testing CT CP and QI specimens. A data reduction method independent of the crack length is implemented in this work to obtain reliable translaminar toughness measurements. This method consists in a numerical computation of a contour J-integral based on DIC measurement of the displacement fields.

The translaminar fracture of CP and QI laminates is strongly influenced by the ply thickness (Fig. 9.1). At crack initiation, the laminate toughness is reduced by 70% when changing from $t=0.150$ mm to $t=0.030$ mm plies in CP laminate. The reduction is of 72% in the QI specimens. The ERR at steady-state is also strongly reduced on this range of ply thicknesses: 80% in CP and 74% in QI specimens. By testing four different ply thickness, both the initiation and propagation ERR are shown to scale linearly with the ply thickness. Globally the laminate fracture toughness is 25% lower in the QI specimens compared to the corresponding CP specimens.

While the fracture toughness is decreased by approximately 75% between the $t=0.150$ and $t=0.030$ mm laminates, the ultimate strength is increased by only 35% on the same range. The reduction of toughness is thus proportionally more important than the increase in the strength on the range of observation. Therefore, the toughness properties should also be accounted for when selecting the ply thickness of a laminate for a real application.

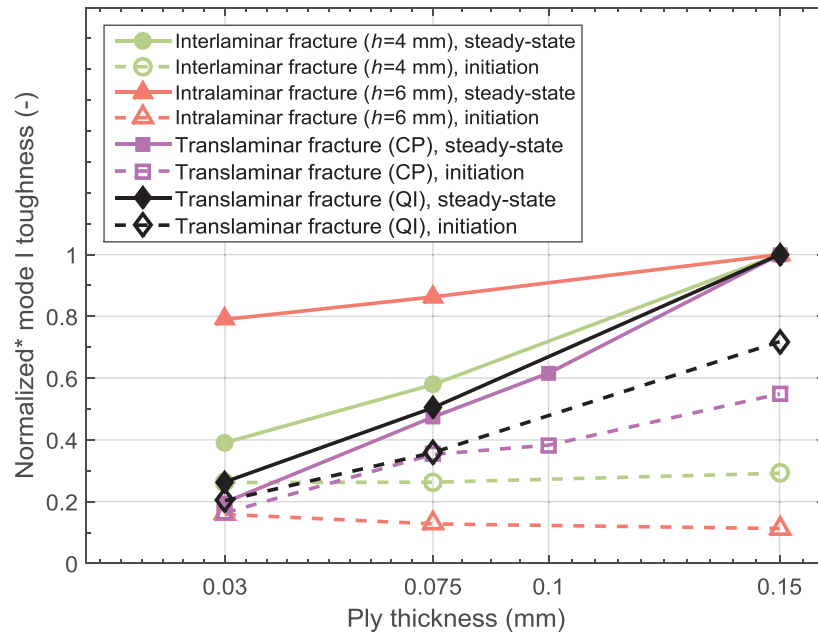


Fig. 9.1: Normalized inter-, intra- and trans-laminar fracture toughness as a function of ply thickness. (* Values normalized by the steady-state ERR at $t=0.150$ mm of the corresponding fracture orientation)

Which mechanisms can explain the observed size effects and what are the dominant parameters governing this behavior?

In inter- and intra-laminar fracture, the ply thickness effect is governed by differences in fiber bridging. This mechanism active in the wake of the crack increases the resistance to fracture. The intensity of fiber bridging is related to the ply thickness through differences of microstructure. The microstructure is much more homogenized in the thin-ply than in the thick-ply UD laminates where fiber- and matrix-rich regions are observed. The inhomogeneity of the microstructure leads to locally high stresses, the development of a large amount of micro-cracks and eventually to a wavy crack front. Such a tortuosity promotes the creation of large

bundles of bridging fibers. In contrast, in the well homogenized thin-ply laminate, the crack front remains flat, which annihilates the development of bridging bundles. The effect of ply thickness is thus reflected in the microstructure heterogeneity as well as in the number and size of fiber bridging bundles.

The ply thickness effect measured in the translaminar fracture is attributed to the fiber pull-out mechanism. Depending on the ply thickness, the 0° fibers break in average at different distance from the initial horizontal crack plane. These fibers are debonded from the surrounding matrix and progressively pulled-out, dissipating energy due to shearing and friction. The average height of the pull-out fibers remains practically constant along the direction of crack propagation. This observation explains the quasi constant increasing slope of the R-curves. The dissipation of energy ends when the fibers are completely pulled-out. Therefore, since the pull-out fibers are much shorter in the thin-ply than in the thick-ply specimens, the amount of dissipated energy is much lower. The decrease in the resistance to fracture is thus directly linked to the height of the pull-out fibers, which is the result of a complex stochastic fragmentation and debonding process.

How does interlaminar fracture differ from intralaminar fracture and what are the causes of such differences?

Inter- and intra-laminar fracture modes are relatively similar since in both cases the crack propagates in the direction parallel to the fibers. However, while in interlaminar fracture the crack is parallel to the plies, it is orthogonal in the intralaminar fracture. At crack initiation the ERR is of comparable magnitude in both modes of fracture. However, in the first 20 mm of crack propagation the ERR increases much more in the intra- than inter-laminar fracture. At steady-state the interlaminar ERR lies in the bound of 212 ($t=0.030$ mm) to 540 ($t=0.150$ mm) J/m². The corresponding values for the intralaminar fracture reach 824 to 1192 J/m².

This significant difference is attributed to the different bridging behavior in particular in the first 20 mm of crack propagation. The explanation proposed in this work relies on the fiber waviness and misalignments. During the production process, the potential fiber misalignments are much larger in the in-plane of the lamina than in the out-of-plane direction. Therefore, while the interlaminar cracks propagate between relatively well aligned fibers, the intralaminar crack planes are likely to intersect with many more fiber paths. Therefore, the probability to generate bridging fibers is larger in intralaminar fracture. Moreover, due to the relative misalignment

angle, these fibers have a strong geometric anchorage and carry large closing forces. In contrast, the relatively well aligned bridging fibers in interlaminar fracture can easily debond and propagate rather than carrying large forces, which explains the large size of the bridging zone. Therefore, the closing force per bridging fibers is higher in intra- than in inter-laminar fracture, leading to higher resistance to fracture.

How can the ply thickness effects be accounted for in the modeling and prediction of fracture in thin-ply composites?

The inter-, intra- and trans-laminar fracture can be simulated by cohesive elements models. To obtain accurate prediction the traction-separation relations must be identified and scaled based on reliable set of experimental data for the different ply thicknesses.

In inter- and intra-laminar fracture, the process zone is relatively long, so that linear or bilinear stiffness degradation fails to predict accurately the crack propagation. In this work, an effective method is proposed for the identification of the traction-separation relations based on the experimental R-curves. This method is validated through comparison with an existing inverse method based on strain measurements. Since the new method is time and cost-effective, it can easily be applied to different series of tests in order to get an accurate traction-separation profile as a function of scaling parameters such as the specimen or ply thickness. In case the number of experimental tests is limited, the extreme cases should be tested and the identification parameters can be interpolated as proposed in section 6.1.

In translaminar fracture, the process zone is relatively short, so that a simplified cohesive model can be used. The initiation ERR is represented by a linear degradation of the initial traction corresponding to the laminate strength. The pull-out mechanism is modeled as a constant traction level until an opening value corresponding to the COD at the crack starter when steady-state propagation is reached. Since the initiation and propagation ERRs and the maximal opening appear to scale linearly with the ply thickness, an empirical scaling relation can be established by testing the two extreme cases. Moreover, for coarse estimates, the rule of mixture could be used to extrapolate the translaminar fracture toughness of the 0° plies to the fracture toughness of multidirectional laminates, as shown in section 7.1.2.

Identifying the traction-relations associated with each ply thickness by the aforementioned technique is the best way to obtain an accurate model. Indeed, the load-displacement responses of the inter-, intra- and translaminar fracture are very

well predicted by the numerical models implemented in this work. However, when a limited amount of experimental data exists, the proposed scaling strategies can be employed to account for the ply thickness effects and obtain good estimations of the fracture responses.

What are the possible solutions to overcome the limitations highlighted in this work while keeping the thin-ply advantages?

The decrease in the fracture toughness with decreasing ply thickness is one of the main limitations of thin-ply composites. Indeed in critical applications such as aeronautics, a sufficiently large resistance to fracture is required to ensure the safety of the structures and schedule maintenance programs. Therefore, a trade-off between the increased strength properties and decreased toughness properties must be found when selecting the ply thickness of the laminate. However, advanced solutions exist to increase the fracture toughness while not losing too much of the benefits of the thin-ply composites.

The interlayer toughening strategy and fiber hybridization technique developed by R. Amacher in his project specifically address the inter- and trans-laminar fracture, respectively. Both methods indeed increase the fracture toughness, but are accompanied with some additional complexity in the production process. Moreover, the fiber hybridization technique decreases significantly the onset of damage and ultimate strength properties, which limits the thin-ply beneficial effect. Therefore a trade-off must be found between the strength, fracture toughness and production cost, among others.

Another way to increase the toughness properties consists in changing the fiber / matrix combination. As an example, the T800 / Aero2 system developed by Amacher et al. [112] and their industrial partners significantly increases the mode I and II interlaminar fracture and the translaminar fracture compared to the M40JB / TP80EP system. Moreover, the strength properties are also improved with this new carbon / epoxy system. Since both the strength and toughness properties are improved for this new generation of thin-ply composite, a real progress is accomplished.

9.2 Perspectives

Based on the significant ply thickness effects observed on the fracture toughness of thin-ply composites, the following research perspectives are proposed for further

analysis. Firstly, as shown in chapter 8, the fracture properties can significantly change with other fiber / matrix combinations. Therefore, this study could be repeated for other systems, in order to verify whether the scaling trends can be generalized to all the thin-ply composites or not. If not, the key parameters activating or deactivating the ply thickness effects should be highlighted.

More specifically, for the inter- and intra-laminar fracture, the extent of ply thickness effect should be verified for multidirectional laminates. Indeed, fiber bridging is known to be affected by the ply orientations. However, the combined effect of ply orientation and ply thickness has not been investigated yet. Moreover, the study can be extended to different mode-mixity, to represent a large range of realistic loading conditions. Finally, further investigations are required to confirm the proposed explanation about the different behaviors observed in inter- and intra-laminar fracture.

Regarding the translaminar fracture, important efforts should be made to develop a standardized testing methodology. Indeed, this fracture mode is more complex than the inter- and intra-laminar modes and requires a better understanding of the underlying failure mechanisms. The lack of uniform testing and data reduction procedure limits the understanding and comparison between the different studies. Among others, the difference of translaminar fracture toughness between the CP and QI laminates should be further investigated, and generalized to other multidirectional laminates.

References

- [1] J. Hale, "Boeing 787, from the ground up," *Aero magazine*, vol. QTR_04, pp. 17-23, 2006.
- [2] M. Holmes, "Global carbon fibre market remains on upward trend," *Reinforced Plastics*, vol. 58, pp. 38-45, 2014.
- [3] R. Amacher, J. Cugnoni, J. Botsis, L. Sorensen, W. Smith and C. Dransfeld, "Thin ply composites: Experimental characterization and modeling of size-effects," *Composites Science and Technology*, vol. 101, pp. 121-132, September 2014.
- [4] S. Sihn, R. Y. Kim, K. Kawabe and S. W. Tsai, "Experimental studies of thin-ply laminated composites," *Composites Science and Technology*, vol. 67, pp. 996-1008, 2007.
- [5] ASTM, "Standard terminology for composite materials," *D3878-16*, 2016.
- [6] M. De Moura, R. Campilho, A. Amaro and P. Reis, "Interlaminar and intralaminar fracture characterization of composites under mode I loading," *Composite Structures*, vol. 92, pp. 144-149, 2010.
- [7] NorthTPT, "<http://www.thinplytechnology.com/product-34-thin-plyprepreg>," [Online].
- [8] G. Guillaumet, "Improved delamination resistance of thin-ply based laminates: an experimental and numerical study," University of Girona, PhD thesis 2016.
- [9] R. Krueger, "Apparatus and method for spreading fibrous tows into linear arrays of generally uniform density and products made thereby". United States Patent 6,311,377, 6 November 2001.
- [10] H. Uno, "Innovative technology for carbon and aramid," *JEC Magazine*, 17,

2005.

- [11] K. Kawabe, T. Matsuo and Z. Maekwa, "New technology for opening various reinforcing fiber tows," *Society of Materials Science*, vol. 47, no. 7, pp. 727-734, 1998.
- [12] T. Yokozeki, Y. Aoki and T. Ogasawara, "Experimental characterization of strength and damage resistance properties of thin-ply carbon fiber/toughened epoxy laminates," *Composite Structures*, vol. 82, pp. 382-389, 2008.
- [13] T. Yokozeki, A. Kuorda, A. Yoshimura, T. Ogasawara and T. Aoki, "Damage characterization in thin-ply composite laminates under out-of-plane transverse loadings," *Composite Structures*, vol. 93, pp. 49-57, 2010.
- [14] M. R. Wisnom, B. Khan and S. R. Hallett, "Size effects in unnotched tensile strength of unidirectional and quasi-isotropic carbon/epoxy composites," *Composite Structures*, vol. 84, pp. 21-28, 2008.
- [15] B. Green, M. Wisnom and S. Hallett, "An experimental investigation into the tensile strength scaling of notched composites," *Composites: Part A*, vol. 38, pp. 867-78, 2007.
- [16] M. R. Wisnom and S. R. Hallett, "Scaling effects in notched composites," *Journal of Composite Materials*, vol. 44, pp. 195-210, 2010.
- [17] A. Arteiro, G. Catalanotti, J. Xavier and P. Camanho, "Notched response of non-crimp fabric thin-ply laminates," *Composites Science and Technology*, vol. 79, pp. 97-114, 2013.
- [18] P. Camanho, C. Dávila, S. Pinho, L. Iannucci and P. Robinson, "Prediction of in situ strengths and matrix cracking in composites under transverse tension and in-plane shear," *Composites: Part A*, vol. 37, pp. 165-176, 2006.
- [19] G. Guillaumet, A. Turon, J. Costa, J. Renart, P. Linde and J. Mayugo, "Damage occurrence at edges of non-crimp-fabric thin-ply laminates under off-axis uniaxial loading," *Composites Science and Technology*, vol. 98, pp. 44-50, 2014.
- [20] C. Sun and Z.-H. Jin, *Fracture Mechanics*, Boston: USA: Academic Press, 2012.
- [21] G. Irwin, "Analysis of stresses and strains near the end of a crack traversing a plate," *Journal of Applied Mechanics*, vol. 24, pp. 361-364, 1957.

References

- [22] A. Griffith, "The phenomena of rupture and flow in solids," *Philosophical Transactions of the Royal Society of London A*, vol. 221, pp. 163-198, 1920.
- [23] G. Irwin and J. Kies, "Critical energy rate analysis of fracture," *Welding Journal*, vol. 33, pp. 193-198, 1954.
- [24] I. Raju and T. O'Brien, "Fracture mechanics concepts, stress fields, strain energy release rates, delamination initiation and growth criteria," in *Delamination Behaviour of Composites*, 2008.
- [25] A. Zehnder, "Fracture Mechanics," in *Lecture Notes in Applied and Computational Mechanics*, Springer, 2012.
- [26] P. Davies, B. Blackman and A. Brunner, "Standard test methods for delamination resistance of composite materials: current status," *Applied Composite Materials*, vol. 5, pp. 345-364, 1998.
- [27] T. Tay, "Characterization and analysis of delamination fracture in composites: An overview of developments from 1990 to 2001," *Applied Mechanics Reviews*, vol. 56, no. 1, pp. 1-32, 2003.
- [28] S. Sridharan, *Delamination behaviour of composites*, Cambridge, 2008.
- [29] E. Farmand Ashtiani, *Studies on large scale bridging in delamination of unidirectional and cross-ply laminates*, École polytechnique fédérale de Lausanne, PhD thesis 2016.
- [30] B. Bigourdan, N. Baral, P. Davies and C. Baley, "Delamination behaviour of very high modulus carbon/epoxy marine composites," *Composites Science and Technology*, vol. 68, no. 3-4, pp. 995-1007, 2008.
- [31] T. Sebaey, N. Blanco, J. Costa and C. Lopes, "Characterization of crack propagation in mode I delamination of multidirectional CFRP laminates," *Composites Science and Technology*, vol. 72, pp. 1251-1256, 2012.
- [32] E. Farmand-Ashtiani, D. Alanis, J. Cugnoni and J. Botsis, "Delamination in cross-ply laminates: Identification of traction-separation relations and cohesive zone modeling," *Composites Science and Technology*, vol. 119, pp. 85-92, 2015.
- [33] J. Andersons and M. König, "Dependence of fracture toughness of composite laminates on interface ply orientations and delamination growth direction," *Composites Science and Technology*, vol. 64, pp. 2139-2152, 2004.

References

- [34] F. Ozdil and L. Carlsson, "Beam analysis of angle-ply laminate DCB specimens," *Composites Science and Technology*, vol. 59, pp. 305-315, 1999.
- [35] A. Russel and K. Street, "Moisture and temperature effects on the mixed-mode delamination fracture of unidirectional graphite/epoxy," *Delamination and Debonding of Materials, ASTM STP 876*, pp. 349-370, 1985.
- [36] E. Farmand-Ashtiani, J. Cugnoni and J. Botsis, "Specimen thickness dependence of large scale fiber bridging in mode I interlaminar fracture of carbon epoxy composite," *International Journal of Solids and Structures*, vol. 55, pp. 58-65, 2015.
- [37] B. D. Manshadi, A. P. Vassilopoulos and J. Botsis, "A combined experimental/numerical study of the scaling effects on mode I delamination of GFRP," *Composites Science and Technology*, vol. 83, pp. 32-39, 2012.
- [38] ASTM, "Standard test method for mode I interlaminar fracture toughness of unidirectional fiber-reinforced polymer matrix composites," *D5528-01*, 2007.
- [39] P. Davies, W. Cantwell and H. Kausch, "Measurement of Initiation Values of Glc in IM6/PEEK Composites," *Composites Science and Technology*, vol. 35, no. 3, pp. 301-313, 1989.
- [40] P. Davies, C. Moulin and H. Kausch, "Measurement of Glc and GIIc in Carbon/Epoxy Composites," *Composites Science and Technology*, vol. 39, pp. 193-205, 1990.
- [41] S. Hashemi, A. Kinloch and J. Williams, "Corrections Needed in Double Cantilever Beam Tests for Assessing the Interlaminar Failure of Fiber Composites," *Journal of Materials Science Letters*, vol. 8, pp. 125-129, 1989.
- [42] J. Rice, "A path independent integral and the approximate analysis of strain concentrations by notches and cracks.," *Journal of Applied Mechanics*, vol. 35, pp. 379-386, 1968.
- [43] J. Anthony and P. Paris, "Instantaneous evaluation of J and C," *International Journal of Fracture*, vol. 38, no. 1, pp. 19-21, 1988.
- [44] J. Gunderson, J. Brueck and A. Paris, "Alternative test method for interlaminar fracture toughness of composites," *International Journal of Fracture*, vol. 143, pp. 273-276, 2007.

References

- [45] C. Sarrado, A. Turon, J. Costa and J. Renart, "On the validity of linear elastic fracture mechanics methods to measure the fracture toughness of adhesive joints," *International Journal of Solids and Structures*, vol. 81, pp. 110-116, 2016.
- [46] ASTM, "Standard test method for determination of the mode II interlaminar fracture toughness of unidirectional fiber-reinforced polymer matrix composites," *D7905/D7905M-14*, 2014.
- [47] P. Davies, G. Sims, B. Blackman, A. Brunner, K. Kageyama, M. Hojo, K. Tanaka, G. Murri, C. Rousseau, B. Gieseke and R. Martin, "Comparison of test configurations for the determination of GIIC: Results from an international round robin," *Plastics, Rubber and Composites*, vol. 28, no. 9, pp. 432-437, 1999.
- [48] J. Barrett and R. Foschi, "Mode II stress-intensity factors for cracked wood beams," *Engineering Fracture Mechanics*, vol. 9, no. 2, pp. 371-378, 1977.
- [49] R. Pipes, L. Carlsson and J. Gillespie, "On the analysis and design of the end notched flexure (ENF) specimen for mode II testing," *Journal of Composite Materials*, vol. 20, no. 6, pp. 594-604, 1986.
- [50] K. Kageyama, M. Kikuchi and N. Yanagisawa, "Stabilized end notched flexure test: characterization of mode II interlaminar crack growth," *ASTM STP 1110-EB*, pp. 210-225, 1991.
- [51] H. Wang and T. Vu-Khanh, "Use of end-loaded-split (ELS) test to study stable fracture behaviour of composites under mode II loading," *Composite Structures*, vol. 36, pp. 71-79, 1996.
- [52] C. Schuecker and B. Davidson, "Evaluation of the accuracy of the four-point bend end-notched flexure test for mode II delamination toughness determination," *Composites Science and Technology*, vol. 60, no. 11, pp. 2137-2146, 2000.
- [53] C. Schuecker and B. Davidson, "Effect of friction on the perceived mode II delamination toughness from three- and four-point bend end-notched flexure tests," *ASTM STP 1383*, pp. 334-344, 2001.
- [54] S. Stutz, "Experimental and numerical studies of mode I and mode II delamination of polymer composites with embedded optical sensors," École

References

- polytechnique fédérale de Lausanne, PhD thesis 2011.
- [55] N. Sato, M. Hojo and M. Nishikawa, "Novel test method for accurate characterization of intralaminar fracture toughness in CFRP laminates," *Composites: Part B*, vol. 65, pp. 89-98, 2014.
- [56] M. Czabaj and J. Ratcliffe, "Comparison of intralaminar and interlaminar mode I fracture toughness of a unidirectional IM7/8552 carbon/epoxy composite," *Composites Science and Technology*, vol. 89, pp. 15-23, 2013.
- [57] B. Sørensen and T. Jacobsen, "Large-scale bridging in composites: R-curves and bridging laws," *Composites: Part A*, vol. 29, no. 11, pp. 1443-1451, 1998.
- [58] M. Iwamoto, Q. Ni, T. Fujiwara and K. Kurashiki, "Intralaminar fracture mechanism in unidirectional CFRP composites. I. Intralaminar toughness and AE characteristics," *Engineering Fracture Mechanics*, vol. 64, no. 6, pp. 721-745, 1999.
- [59] G. Pappas and J. Botsis, "Intralaminar fracture of unidirectional carbon/epoxy composite: experimental results and numerical analysis," *International Journal of Solids and Structures*, Vols. 85-86, pp. 114-124, 2016.
- [60] G. Pappas, L. Canal and J. Botsis, "Characterization of intralaminar mode I fracture of AS4/PPS composite using inverse identification and micromechanics," *Composites: Part A*, vol. 91, pp. 117-126, 2016.
- [61] L. Canal, G. Pappas and J. Botsis, "Large scale fiber bridging in mode I intralaminar fracture. An embedded cell approach," *Composites Science and Technology*, vol. 126, pp. 52-59, 2016.
- [62] T. Jacobsen and B. Sørensen, "Mode I intra-laminar crack growth in composites - modelling of R-curves from measured bridging laws," *Composites: Part A*, vol. 32, pp. 1-11, 2001.
- [63] R. Gutkin, M. J. Laffan, S. T. Pinho, P. Robinson and P. T. Curtis, "Modelling the R-curve effect and its specimen-dependence," *International Journal of Solids and Structures*, vol. 48, pp. 1767-1777, 2011.
- [64] R. Truss, P. Hine and R. Duckett, "Interlaminar and intralaminar fracture toughness of uniaxial continuous and discontinuous carbon fibre/epoxy composites," *Composites: Part A*, vol. 28, no. 7, pp. 627-636, 1997.

References

- [65] S. Jose, R. Kumar, M. Jana and G. Rao, "Intralaminar fracture toughness of a cross-ply laminate and its constituent sub-laminates," *Composites Science and Technology*, vol. 61, no. 8, pp. 1115-1122, 2001.
- [66] F. Macedo, A. Pereira and A. de Morais, "Mixed bending-tension (MBT) test for mode I interlaminar and intralaminar fracture," *Composites Science and Technology*, vol. 48, no. 11-12, pp. 1049-1055, 2012.
- [67] G. Pappas, Studies on traction-separation relations in fracture of layered composites; experiments and modeling, École polytechnique fédérale de Lausanne, PhD thesis 2017.
- [68] W. Johnson and P. Mangalgiri, "Investigation of fiber bridging in double cantilever beam specimens," *Journal of Composites Technology and Research*, vol. 9, no. 1, pp. 10-13, 1987.
- [69] G. Frossard, J. Cugnoni, T. Gmür and J. Botsis, "Mode I interlaminar fracture of carbon epoxy laminates: effects of ply thickness," *Composites: Part A*, vol. 91, pp. 1-8, 2016.
- [70] G. Frossard, J. Cugnoni, T. Gmür and J. Botsis, "Mode I fracture of thin-ply carbon-epoxy laminates: effects of ply thickness," in *20th international conference on composite materials (ICCM/20)*, Copenhagen, 2015.
- [71] M. Shokrieh, M. Salamat-Talab and M. Heidari-Rarani, "Effect of interface fiber angle on the R-curve behavior of E-glass/epoxy DCB specimens," *Theoretical and Applied Fracture Mechanics*, vol. 86, pp. 153-160, 2016.
- [72] B. Sørensen and T. Jacobsen, "Determination of cohesive laws by the J integral approach," *Engineering Fracture Mechanics*, vol. 70, pp. 1841-1858, 2003.
- [73] V. Tamuzs, S. Tarasovs and U. Vilks, "Progressive delamination and fiber bridging modeling in double cantilever beam composite specimens," *Engineering Fracture Mechanics*, vol. 68, pp. 513-525, 2001.
- [74] L. Sorensen, J. Botsis, T. Gmür and L. Humbert, "Bridging tractions in mode I delamination: Measurements and simulations," *Composites Science and Technology*, vol. 68, no. 12, pp. 2350-2358, 2008.
- [75] S. Stutz, J. Cugnoni and J. Botsis, "Studies of mode I delamination in monotonic and fatigue loading using FBG wavelength multiplexing and numerical

- analysis," *Composites Science and Technology*, vol. 71, pp. 443-449, 2011.
- [76] R. Kottner, R. Hynek and T. Kroupa, "Identification of parameters of cohesive elements for modeling of adhesively bonded joints of epoxy composites," *Applied and Computational Mechanics*, vol. 7, pp. 137-144, 2013.
- [77] C. G. Davila, C. A. Rose and P. P. Camanho, "A procedure for superposing linear cohesive laws to represent multiple damage mechanisms in the fracture of composites," *International Journal of Fracture*, vol. 158, pp. 211-223, 2009.
- [78] M. Heidari-Rarani, M. M. Shokrieh and P. P. Camanho, "Finite element modeling of mode I delamination growth in laminated DCB specimens with R-curve effects," *Composites: Part B*, vol. 45, pp. 897-903, 2013.
- [79] S. Stutz, J. Cugnoni and J. Botsis, "Crack - fiber sensor interaction and characterization of the bridging tractions in mode I delamination," *Engineering Fracture Mechanics*, vol. 78, pp. 890-900, 2011.
- [80] G. Frossard, J. Cugnoni, T. Gmür and J. Botsis, "An efficient method for fiber bridging traction identification based on the R-curve: Formulation and experimental validation," *Composite Structures*, vol. 175, pp. 135-144, 2017.
- [81] ASTM, "Standard test method for translaminar fracture toughness of laminated and pultruded polymer matrix composite materials," *E1922-04*, 2010.
- [82] ASTM, "Standard test method for linear-elastic plane-strain fracture toughness K_{Ic} of metallic materials," *E399-12*, 2012.
- [83] S. Pinho, P. Robinson and L. Iannucci, "Fracture toughness of the tensile and compressive fibre failure modes in laminated composites," *Composites Science and Technology*, vol. 66, pp. 2069-2079, 2006.
- [84] M. J. Laffan, S. T. Pinho, P. Robinson and L. Iannucci, "Measurement of the in situ ply fracture toughness associated with mode I fibre tensile failure in FRP. Part I: Data reduction," *Composites Science and Technology*, vol. 70, pp. 606-613, 2010.
- [85] M. J. Laffan, S. T. Pinho, P. Robinson and A. J. McMillan, "Translaminar fracture toughness testing of composites: A review," *Polymer Testing* 31, pp. 481-489, 2012.

References

- [86] J. Underwood and M. Kortschot, "Notch-tip damage and translaminar fracture toughness measurements from carbon/epoxy laminates," *US army armament research, development and engineering center, Technical report ARCCB-TR-94010*, 1994.
- [87] J. Masters, "Translaminar fracture toughness of a composite wing skin made of stitched warp-knit fabric," *NASA Contractor Report 201728*, 1997.
- [88] G. Catalanotti, P. P. Camanho, J. Xavier, C. G. Davila and A. T. Marques, "Measurement of resistance curves in the longitudinal failure of composites using digital image correlation," *Composites Science and Technology*, vol. 70, pp. 1986-1993, 2010.
- [89] F. Hou and S. Hong, "Characterization of R-curve behavior of translaminar crack growth in cross-ply composite laminates using digital image correlation," *Engineering Fracture Mechanics*, vol. 117, pp. 51-70, 2014.
- [90] C. Sun and K. Prewo, "The fracture toughness of boron aluminum composites," *Journal of Composite Materials*, vol. 11, pp. 164-175, 1977.
- [91] M. Laffan, S. Pinho, P. Robinson and A. McMillan, "Translaminar fracture toughness: The critical notch tip radius of 0° plies in CFRP," *Composites Science and Technology*, vol. 72, pp. 97-102, 2011.
- [92] M. Laffan, S. Pinho and P. Robinson, "Mixed-mode translaminar fracture of CFRP: Failure analysis and fractography," *Composite Structures*, vol. 95, pp. 135-141, 2013.
- [93] L. Gigliotti and S. Pinho, "Translaminar fracture toughness of NCF composites with multiaxial blankets," *Materials and Design*, vol. 94, pp. 410-416, 2016.
- [94] G. Bullegas, S. Pinho and S. Pimenta, "Engineering the translaminar fracture behaviour of thin-ply composites," *Composites Science and Technology*, vol. 131, pp. 110-122, 2016.
- [95] R. Teixeira, S. Pinho and P. Robinson, "Thickness-dependence of the translaminar fracture toughness: Experimental study using thin-ply composites," *Composites: Part A*, vol. 90, pp. 33-44, 2016.
- [96] C. Furtado, A. Arteiro, M. Bessa, B. Wardle and P. Camanho, "Prediction of size effects in open-hole laminates using only the Young's modulus, the strength,

References

- and the R-curve of the 0° ply," *Composites: Part A*, vol. 101, pp. 306-317, 2017.
- [97] M. J. Laffan, S. T. Pinho, P. Robinson and L. Iannucci, "Measurement of the in situ ply fracture toughness associated with mode I fibre tensile failure in FRP. Part II: Size and lay-up effects," *Composites Science and Technology*, vol. 70, pp. 614-621, 2010.
- [98] S. Pimenta and S. Pinho, "An analytical model for the translaminar fracture toughness of fibre composites with stochastic quasi-fractal fracture surfaces," *Journal of the Mechanics and Physics of Solids*, vol. 66, pp. 78-102, 2014.
- [99] Toray, "M40J data sheet (technical data sheet No. CFA-014)".
- [100] A. De Morais and M. De Moura, "Evaluation of initiation criteria used in interlaminar fracture tests," *Engineering Fracture Mechanics*, vol. 73, pp. 2264-2276, 2006.
- [101] L. Sorensen, J. Botsis, T. Gmür and J. Cugnoni, "Delamination detection and characterisation of bridging tractions using long FBG optical sensors," *Composites: Part A*, vol. 38, pp. 2087-2096, 2007.
- [102] J. Botsis, "Fiber Bragg grating applied to in-situ characterization of composites," in *Wiley Encyclopedia of Composites*, New Jersey, John Wiley & Sons, 2012, pp. 1-15.
- [103] Z. Suo, G. Bao and B. Fan, "Delamination R-curve phenomena due to damage," *Journal of the Mechanics and Physics of Solids*, vol. 40, no. 1, pp. 1-16, 1992.
- [104] L. Canal, C. Gonzalez, J. Segurado and J. Llorca, "Intraply fracture of fiber-reinforced composites: Microscopic mechanisms and modeling," *Composites Science and Technology*, vol. 72, pp. 1223-1232, 2012.
- [105] L. Canal, M. Alfano and J. Botsis, "A multi-scale based cohesive zone model for the analysis of thickness scaling effect in fiber bridging," *Composites Science and Technology*, vol. 139, pp. 90-98, 2017.
- [106] S. Spearing and A. Evans, "The role of fiber bridging in the delamination resistance of fiber-reinforced composites," *Acta Metallurgica et Materialia*, vol. 40, no. 9, pp. 2191-2199, 1992.
- [107] B. Sørensen, E. Gamstedt, R. Østergaard and S. Goutianos, "Micromechanical model of cross-over fibre bridging – Prediction of mixed mode bridging laws,"

References

- Mechanics of Materials*, vol. 40, pp. 220-234, 2008.
- [108] R. F. Teixeira, S. T. Pinho and P. Robinson, "Translaminar ply fracture toughness of advanced composites," in *18th international conference on composite materials*, Jeju Island, South Korea, 2011.
- [109] P. P. Camanho and G. Catalanotti, "On the relation between the mode I fracture toughness of a composite laminate and that of a 0° ply : Analytical model and experimental validation," *Engineering Fracture Mechanics*, vol. 78, pp. 2535-2546, 2011.
- [110] M. Jalalvand, G. Czél and M. Wisnom, "Damage analysis of pseudo-ductile thin-ply UD hybrid composites - A new analytical method," *Composites: Part A*, vol. 69, pp. 83-93, 2015.
- [111] X. Li, S. Hallet, M. Wisnom, N. Zobeiry, R. Vaziri and A. Poursartip, "Experimental study of damage propagation in over-height compact tension tests," *Composites: Part A*, vol. 40, pp. 1891-1899, 2009.
- [112] R. Amacher, J. Cugnoni, J. Brunner, E. Kramer, C. Dransfeld, W. Smith, K. Scobbie, L. Sorensen and J. Botsis, "Toward aerospace grade thin-ply composites," in *European conference on composite materials ECCM17*, Munich, Germany, 2016.
- [113] Toray, "T800S data sheet (technical data sheet No. CFA-019)".
- [114] K. Ravichandran, "Fracture resistance of structural alloys," in *ASM Handbook, Volume 19: Fatigue and Fracture*, 1996, pp. 381-392.
- [115] Y. Aoki, H. Samejima, H. Suemasu and Y. Nagao, "Effect of thickness on impact damage and CAI behavior," in *17th International conference on composite materials, ICCM17*, Edinburgh (UK), 2009.
- [116] ASTM, "Standard test method for measuring the damage resistance of a fiber-reinforced polymer matrix composite to a drop-weight impact event," *D7136/D7136M-07*, 2007.
- [117] ASTM, "Standard test method for compressive residual strength properties of damaged polymer matrix composite plates," *D7137/D7137M-07*, 2007.
- [118] Mitsubishi chemical - Carbon fiber and composites, "<http://mccfc.com/pan-fiber/>," [Online].

Curriculum Vitae

Personal data:

Name : Guillaume Frossard
Address : Av. Pictet-de-Rochemont 23
CH-1207 Genève
Birth date : 18th September 1988
Nationality : Swiss
Languages : French, English, German
Phone : 0041 79 850 46 81
Email : guillaumefrossard@hotmail.com



Education:

2014-2018 **PhD** in solid mechanics, STI-IGM-LMAF
2011-2013 **Master of Science** in Mechanical Engineering, EPFL
Bombardier Transportation Award (Best average grade of the Master cycle in Mechanical engineering, 2013)
Erasmus exchange, one year at Heriot-Watt University, Edinburgh, UK
2008-2011 **Bachelor of Science** in Mechanical Engineering, EPFL
Ranking: 4/69
2002-2007 **High school diploma**, latin & sciences orientation, Lycée-Collège de l'Abbaye de St-Maurice

Professional experiences:

2014-2018 Doctoral assistant, EPFL – LMAF
Teaching assistant in the following courses:

- Mécanique des structures (Mechanics of structures)
- Mécanique des milieux continus (Continuum mechanics)
- TP de techniques de mesures, analyse modale (Practical workshops in modal analysis)
- Fracture mechanics

2013 Master project, Georg Fischer Automotive SA, Schaffhausen

List of publications:

Frossard G, Cugnoni J, Gmür T, Botsis J. Ply thickness effect of the translaminar fracture in thin-ply composites. (in preparation)

Frossard G, Cugnoni J, Gmür T, Botsis J. Ply thickness dependence of the intralaminar fracture in thin-ply composites. (submitted to Composites: Part A, 8th July 2017).

Frossard G, Cugnoni J, Gmür T, Botsis J. An efficient method for fiber bridging traction identification based on the R-curve: Formulation and experimental validation. *Composite Structures* 2017; 175: 135-144.

Frossard G, Cugnoni J, Gmür T, Botsis J. Mode I interlaminar fracture of carbon epoxy laminates: effects of ply thickness. *Composites Part A* 2016; 91: 1–8.

List of conference participations:

Frossard G, Amacher R, Cugnoni J, Gmür T, Costa J, Garcia-Rodriguez SM, Botsis J. Translaminar fracture of thin-ply composites: hybridization as toughening strategy. *CompTest* 8, 2017, Leuven.

Frossard G, Cugnoni J, Gmür T, Botsis J. Fiber bridging identification based on the R-curves of thin-ply layered composites. *ICEM* 17, 2016, Rhodes.

Frossard G, Cugnoni J, Gmür T, Botsis J. Mode I fracture of thin-ply carbon-epoxy laminates: effects of ply thickness. In proceeding *ICCM* 20, 2015, Copenhagen.

Frossard G, Cugnoni J, Gmür T, Botsis J. Mode I fracture of thin-ply carbon-epoxy laminates: effects of ply and specimen thickness. *CompTest* 7, 2015, Madrid.

Frossard G, Cugnoni J, Gmür T, Botsis J. Influence of the thin ply size on mode I and mode II energy release rate of unidirectional carbon epoxy laminates. *ICEM* 16, 2014, Cambridge.

Selected projects:

- | | |
|------------------|---|
| PhD thesis | EPFL, Lausanne. Fracture of thin-ply carbon-epoxy laminates: effects of ply thickness. |
| Master project | Georg Fischer, Schaffhausen. Prediction of residual stresses and deformation in high pressure die casted components and validation by experimental measurements. |
| Bachelor project | Heriot-Watt University, Edinburgh. Design and use of an experimental posture detection platform to study the equilibrium of patients suffering from central nervous system pathologies. |

